Omar Manzardo

Band 418

Micro-Sized Fourier Spectrometers

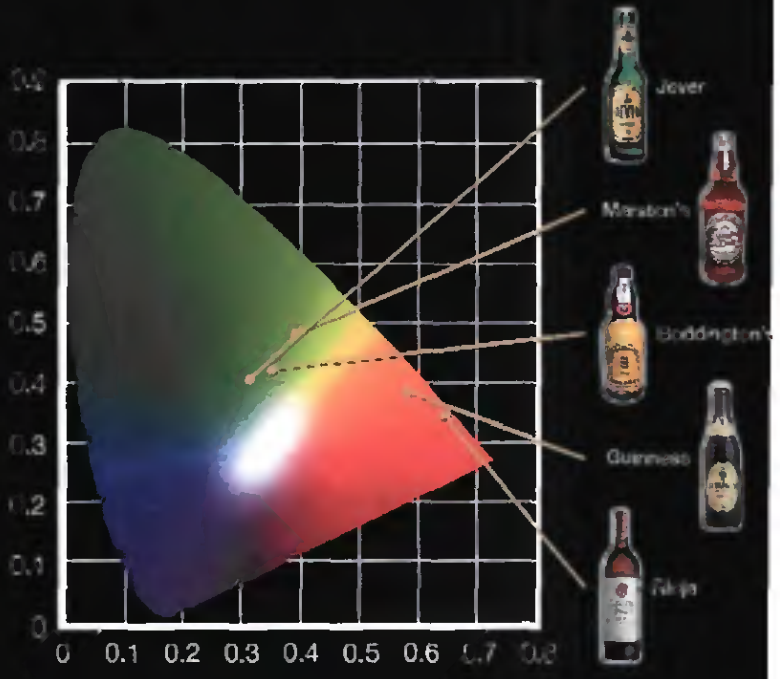

Université de Neuchâtel
Institut de Microtechnique

Micro-sized Fourier Spectrometers

Thèse

Présentée à la faculté des sciences
pour obtenir le grade de docteur ès sciences
par

Omar Manzardo

Neuchâtel, janvier 2002

UFO Dissertation Band 418

Die Deutsche Bibliothek – CIP-Einheitsaufnahme
Ein Titeldatensatz für diese Publikation ist bei
Der Deutschen Bibliothek erhältlich.

Dissertation der Universität Neuchâtel
Datum der mündlichen Prüfung: 17.01.2002
Referenten: Prof. Dr. R. Dändliker
Prof. Dr. H.-P. Herzig
Prof. Dr. N. de Rooij
Dr. H. Teichmann
Prof. Dr. G. Guelachvili

UFO Atelier für Gestaltung & Verlag GbR · D-78476 Allensbach
Internet: www.ufo-verlag.de

ISBN 3-935511-19-1

IMPRIMATUR POUR LA THESE

Micro-sized Fourier Spectrometers

de M. Omar Manzardo

UNIVERSITE DE NEUCHATEL

FACULTE DES SCIENCES

La Faculté des sciences de l'Université de Neuchâtel sur le rapport des membres du jury,

MM. R. Dändliker (directeur de thèse),
N. de Rooij, H.-P. Herzig, H. Teichmann (Zürich)
et G. Guelachvili (Orsay F)

autorise l'impression de la présente thèse.

Neuchâtel, le 25 septembre 2002

Le doyen:

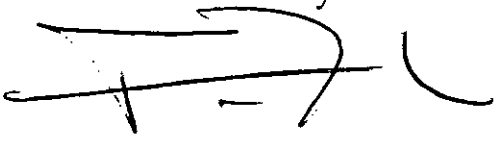

F. Zwahlen

Abstract

Fourier transform spectroscopy is a well-known and widely used technique. It is a powerful tool to measure the spectra of weak extended sources, since it offers distinct throughput and multiplex advantages, providing higher signal-to-noise ratio performance compared with other methods. Many commercial Fourier spectrometers are available. Their main applications are in fields that require high resolution. Therefore, commonly used Fourier spectrometers necessitate a scanning mirror mechanism with very high precision, resulting in large size and high cost.

Nowadays, lower resolution miniature spectrometers become attractive because of new applications, expanding opportunities in a remarkable variety of disciplines and industries. Miniaturization could make instruments and sensors smaller, cheaper and faster. Target applications are various and they include color measurements, industrial process control, quality control of food, environmental monitoring or medical diagnosties. Other aspects, like the size and the fabrication cost, play an important role for this type of miniature spectrometers, enabling the realization of small size, portable sensor solutions.

In this thesis, we report on two specific miniaturized spectrometers. Both devices are based on the Michelson interferometer. The first one is a spatially modulated (stationary) Fourier spectrometer and the second one is a time-scanning interferometer. This work includes an overview of the subject of Fourier transform spectroscopy (FTS), as well as more specific facets regarding Fourier spectrometers, essentially when considering micro-sized devices.

The stationary Fourier transform spectrometer operates in the visible wavelength range. No moving parts, no imaging system and compactness are the characteristics of this spectrometer. It is functional for applications requiring moderate spectral resolution (10 nm) but a good stray light suppression in the blue region (better than 20 dB). The measured resolution of the spectrometer is 3 nm at a wavelength of 633 nm. The dimensions are 3 mm $\times$ 3.3 mm $\times$ 25 mm.

The time-scanning Fourier transform spectrometer is based on micro-optical electro-mechanical systems (MOEMS) technology. An electrostatic comb drive actuator moves the scanning mirror. The maximum optical path differenec is equal to 77 μm. The measured resolution of the spectrometer is 6 nm at a wavelength of 633 nm. The dimensions are 5 mm $\times$ 5 mm $\times$ 0.5 mm.

Acknowledgements

This thesis was mostly carried out within the framework of the project MICROSPEC, an element of the EUREKA programme for promoting European research and development. It is in this context that I was able to join the group of applied optics of Professor René Dändliker and Professor Hans Peter Herzig, both of whom became my thesis advisers. I would like to thank them warmly for welcoming me within their team. Peter Kipfer, also involved in the above mentioned project, was instrumental in helping me take my first steps within the field of optics in/outside the institute. As a souvenir, I dedicate the measurements shown in Fig. 4.30, with many thanks. Among the project partners, I wish to thank Helmut Teichmann and all the staff of the CSEM Zürich, as well as Peter Ehbets at GretagMacbeth. The development of the original MEMS-based interferometer was the result of a fruitful collaboration with the SAMLAB of our institute, and it still is today. I would also like to express my sincere gratitude to Nico de Rooij, Cornel Marxer, Benedikt Guldimann, Wilfried Noell, Sylviane Pochon, Pierre-André Clerc, Giani Mondin, Sylvain Jeanneret, for teaching me the necessary know-how, which helped me to work efficiently and safely in the field of micro-electro-mechanical systems, as well as allowing me to make use of the clean room facilities. Many thanks also to Guy Guelachvili, for accepting to be a member of my thesis jury. Finally, I am very grateful to my parents for supporting me throughout my academic career. Last but not least, I wish to thank all friends and colleagues who crossed my karma and interacted with my shakras during the time this PhD was carried out: Virginie, Caspar, David, Gabriel, Felix, Emiliano, Piero, Irène, Lionel, Luciana, Stephanie, Dania, Claude, Toralf, Emilien, Josepha, Karim, Lucien and Yvette Horner, Andreas, Etienne, nona Maria, Carsten, Christophe, Guido, Lory, John, Christian, Tommaso, Antonello, Sylvie, Martin, Christel, Joelle, Olivier, Luigi, ... I'll pay a beer to anyone I forgot.

Publications

Part of the work described in this thesis has already been published in peer-reviewed journals and has been presented at various international conferences.

Publications in peer-reviewed journals

R. Dändliker, H. P. Herzig, O. Manzardo, T. Scharf, G. Boer. Micro-Optics for Spectroscopy. ICO V Triennial publication, *International Trends in Optics*, Edited by A. H. Guenther, (2002).

W. Noell, P. A. Clerc, L. Dellmann, B. Guldimann, H. P. Herzig, O. Manzardo, C. Marxer, K. Weible, R. Dändliker, and N. De Rooij. Applications of SOI-based optical MEMS. *J. Selec. Top. Quant. Electr.*, **8**, 148 (2002).

O. Manzardo, H. P. Herzig, C. R. Marxer, and N. F. De Rooij. Miniaturized time-scanning Fourier transform spectrometer based on silicon technology. *Opt. Lett.* **24**, 1705 (1999).

Contributions presented at international conferences

W. Noell, W. Sun, N. De Rooij, H. P. Herzig, O. Manzardo, and R. Dändliker. Optical MEMS based on Silicon-on-Insulator (SOI) for Monolithic Microoptics. *15th Annual Meeting of the IEEE Lasers and Electro-Optics Society*, November 10–14, 2002, Glasgow, Scottland.

O. Manzardo, Y. Petremand, H. P. Herzig, W. Noell, and N. De Rooij. Micro-fabricated spectral analysers. *19th Congress of the International Commission for Optics: Optics for the Quality of Life*, August 25–30, 2002, Firenze, Italy.

O. Manzardo, Y. Petremand, H. P. Herzig, W. Noell, and N. De Rooij. Micro-fabricated wavelengths monitoring. *IEEE's conference on Optical MEMS and Their Applications*, August 20–23, 2002, Lugano, Switzerland, IEEE Catalog 02EX610, pp. 23–24.

W. Noell, P.-A. Clerc, B. Guldimann, G. Schürmann, U. Staufer, N. De Rooij, H. P. Herzig, O. Manzardo, R. Dändliker, and C. Marxer. Optical microelectromechanical systems (OMEMS) based on silicon-on-insulator (SOI) technology. OSA *Trends in Optics*

and Photonics (TOPS) Vol. 75, Diffractive Optics and Micro-Optics, OSA Technical Digest, Postconference Edition (Optical Society of America, Washington DC), June 3–6, 2002, Tucson, AZ, USA, pp. 114–116.

O. Manzardo, Y. Petremand, H. P. Herzig, W. Noell, and N. De Rooij. Micro-sized Fourier spectrometer. OSA *Trends in Optics and Photonics (TOPS) Vol. 75, Diffractive Optics and Micro-Optics*, OSA Technical Digest, Postconference Edition (Optical Society of America, Washington DC), June 3–6, 2002, Tucson, AZ, USA, pp. 119–121.

O. Manzardo, H. P. Herzig, B. Guldimann, C. R. Marxer, and N. F. De Rooij. New design for an integrated Fourier transform spectrometer. *SPIE's symposium on Micromachining and Microfabrication*, September 18–20, 2000, Santa Clara, Proc. of SPIE Vol. 4178, pp. 310–319.

O. Manzardo, B. Guldimann, C. R. Marxer, N. F. De Rooij, and H. P. Herzig. Optics and actuators for miniaturized spectrometers. *IEEE's conference on Optical MEMS*, August 21–24, 2000, Kauai Hawaii, IEEE Catalog 00EX399, pp. 23–24.

R. Dändliker, H. P. Herzig, O. Manzardo, and S. Traut. Micro-optics for spectroscopy. *Internation canference on optical sciences and applications for sustainable development*, April 10–14, 2000, Dakar, Senegal.

O. Manzardo, H. P. Herzig, C. R. Marxer, and N. F. De Rooij. Miniaturized time-scanning Fourier transform spectrometer based on silicon technology. *SPIE's 1999 Symposium and Education Program on Micromachining and Microfabrication*, September 20–22, 1999, Santa Clara CA, USA.

H. P. Herzig, O. Manzardo. Miniaturized Fourier Transform Spectrometers. *3rd International Conference on Micro Opto Electro Mechanical Systems - MOEMS '99*, August 30 – September 1, 1999, Mainz, Germany.

O. Manzardo, C. R. Marxer, and H. P. Herzig. Miniaturized time-scanning Fourier transform spectrometer using an electrostatic actuator. *18th Congress of the International Commission for Optics: Optics for the Next Millennium*, August 2–6, 1999, San Francisco CA, USA.

O. Manzardo, P. Kipfer, H.P. Herzig. Dispersive compact Fourier transform spectrometer for the visible. *OSA Fourier Transform Spectroscopy: New Methods and Applications*, June 22–24, 1999, Santa Barbara CA, USA.

C. Marxer, O. Manzardo, and N. F. De Rooij. An electrostatic actuator with large dynamic range and linear displacement-voltage behaviour for a miniature spectrometer. *Transducers' 99*, June 7–10, 1999, Sendai, Japan.

O. Manzardo, C. Marxer, H. P. Herzig. Miniaturized time-scanning Fourier transform

spectrometer using an electrostatic actuator. *DGaO Jahrestagung 1999*, May 25–29, 1999, Berlin, Germany.

O. Manzardo, P. Kipfer, H. P. Herzig, H. Teichmann, M. T. Gale, P. Ebbets. Compact Fourier Transform Spectrometer for Applications Requiring Moderate Resolution. *EOS topical meetings digests series: Vol. 16 (Optical Spectral Analysis Microsystems)*, April 6–8, 1998, Engelberg, Switzerland.

O. Manzardo, P. Kipfer, and H. P. Herzig. Compact Fourier spectrometer for the visible region. *DGaO Jahrestagung 1997*, May 21–24, 1997, Kloster Banz, Germany.

Contents

Chapter 1

Introduction

Fourier transform spectroscopy (FTS) is a powerful tool which is now widely used. It is a well-known technique to measure the spectra of weak extended sources, since it offers distinct throughput and multiplex advantages, providing higher signal-to-noise ratio performance compared with other methods like grating or Fabry-Perot.

Many commercial Fourier spectrometers are available and their main applications are in fields that require high resolution. Therefore, commonly used Fourier spectrometers necessitate a scanning mirror mechanism with very high precision, resulting in large size and high cost.

Nowadays, lower resolution miniature spectrometers find their 'raison d'être' because of new applications, expanding opportunities in a remarkable variety of disciplines and industries. Target applications are various and they include color measurements, industrial process control, environmental monitoring or medical diagnostics. Other aspects, like the size and the fabrication cost, play an important role for this type of miniature spectrometers.

The trend towards miniaturization started in the early 1990s, with spectrometers which are sufficiently portable to bring the sensor to the sample. With the title 'Spectrometers move out of the lab', the magazine *Laser Focus World* devoted its cover article of the February 2001 issue to miniature spectrometers:

> 'Thought the first spectroscope was developed nearly 200 years ago, only in the last decade or so has spectroscopic instrumentation escaped the confines of the laboratory. Thanks to a fortuitous combination of circumstances – the mass production of optical fibers, the development of less costly and more efficient detectors and optics, and the emergence of personal computers – the practical applications of spectroscopy has expanded beyond the lab and into the field, into the factory, and even into the human body. In fact, applications once thought impossible, or at best, impractical, are now nearly commonplace, using real-time, *in situ* spectroscopy.'

The vast majority of commercially available portable colour sensors are grating-based spectrometers. The reason is the relatively easy fabrication and assembly of the critical elements. Our aim in this thesis is to demonstrate that miniaturized Fourier spectrometers have an enormous potential for the same task, especially when their realization utilizes particularly versatile technologies of micro-systems fabrication.

Outline of this thesis

Most of the work reported in this thesis was undertaken in the framework of the project *Microspec*, which was part of the EUREKA programme for promoting European research and development. Three Swiss and two British industrial and non-industrial partners collaborated to develop prototypes of miniaturized cheap spectrometers operating in the visible wavelength range. The work is the result of the collaboration between IMT (Institute of Microtechnology), CSEM Zürich (formerly Paul Scherrer Institute), GretagMacbeth, BRI (Brewing Research International) and Msquared. The markets are in the food and drink industries (beer colour), the graphics and imaging industries (surface colour measurements), the process control in chemistry and the environment monitoring of colour (surface and ground waters).

The present work is an investigation of the potentials and limitations of miniature Fourier spectrometers. In other words, we shall give a theoretical and experimental evaluation of Fourier spectrometers when their dimensions become comparable to existing portable spectroscopic sensing systems. The evaluation has been undertaken by simulating interference patterns and by discussing specific aspects of miniature Fourier spectrometers (chapter 3). Experimental assessments have been carried out by means of a modular stationary Michelson interferometer (section 4.1). Additionally, this thesis presents two specific compact spectrometers. Both devices are based on the well-known Michelson interferometer. The first one is a spatially modulated Fourier spectrometer (sections 4.2 and 4.3) and the second one is a time-scanning interferometer (sections 5.2 and 5.3).

The stationary Fourier spectrometer described in chapter 4 is built with a non conventional shape of the beamsplitter and it operates in the visible wavelength range. No moving parts, no imaging system and compactness are the characteristics of this spectrometer. It is functional for applications requiring moderate spectral resolution (10 nm) but a good stray light suppression in the blue region (better than 20 dB). The principal advantage of stationary Fourier spectrometers is the absence of a mobile mirror, since the interferogram is spread in space rather than in time. For the detection, a photodiode array (PDA) is necessary to record the interferogram instantaneously. The resolution is limited by the relatively small amount of sampling points (or pixel of the PDA), contrary to a scanning configuration where the major limiting factor is the maximum achievable path difference. Therefore, the ambition of spatially modulated and static-type Fourier spectrometers is to be stable, compact and robust enough to operate as portable sensors; their aspect is mostly monolithic and their tolerance against vibrations has to be strong. Due to the fact that a silicon PDA is used, their wavelength range is normally restricted from the ultraviolet to the near-infrared. Detector arrays for other wavelengths are non-standard.

Despite the clear advantages of a stationary configuration, the time-scanning solution described in chapter 5 offers some benefits as well. The use of a single photodiode, instead of an array (PDA), eliminates the nuisance coming from the background intensity distribution. The resolution is not limited by the number of pixels of the PDA, but only by the maximum achievable scan distance of the mirror. In addition, the influence of the angular extension of the source is strongly reduced, since the mirrors are not tilted with respect to each other. The development of this original micro-electro-mechanical system

(MEMS) based interferometer is the result of a collaboration with the Sensors, Actuators and Microsystem Laboratory (SAMLAB) of our institute. This device is currently under investigation in view of an industrial prototype.

The size of the time-scanning Michelson interferometer, which is in the order of the millimeter, and the specific fabrication technology are fundamental assets. Together with the advantages offered by a scanning configuration, they provide net profit to this particular solution. The experimental characterization of the motion of the mirror is presented and we demonstrate that the device is suitable for Fourier spectroscopy in the visible and near-infrared region with a resolution better than 10 nm.

Finally, in chapter 5, we give a description of silicon micromachining, more particularly silicon-on-insulator (SOI) technology, which is the technique used to realize the time-scanning Michelson interferometer. This technology is nowadays widely used to build movable devices using silicon integrated-circuit batch-fabrication processes, so-called MEMS (micro-electro-mechanical systems). MOEMS (micro-optical- electro-mechanical systems) is the combination of microoptics and micromechanics. This combination is a challenging new field and it is exploited in order to create a wider class of integrated microoptical systems. As the two constituent technologies in MOEMS are compatible with integrated-circuit technology, they allow batch processing. Thus, MOEMS can be produced in large quantity at low cost, which makes them highly attractive for commercial applications.

Chapter 2

Elements of Fourier transform spectroscopy

The aim of this chapter is to give an overview of the subject of Fourier transform spectroscopy (FTS). Indeed, a lot has been written since the huge development of this technique, in the seventies. The relevant themes (those that made FTS famous) will be mentioned in this introduction, but rather than extending their description, we will focus on elements closer to this specific work. First of all, the notion of interferogram will be presented from its formation to the connection with the spectrum, introducing the concepts of coherence and random processes. In a second part, we shall discuss the recovery of the spectrum from the interferogram. Specific aspects resulting from the particularity of our devices will be treated: asymmetric interferograms and phase errors. Finally, we shall introduce the notion of resolution and develop the typical aspects dealing with the instrument and their influence on the spectrum.

The discussion presented in this chapter is mainly issued from a number of books introducing and treating particular aspects of FTS [1, 2, 3, 4, 5, 6, 7, 8, 9].

Known advantages of Fourier transform spectroscopy.

The general advantages of Fourier transform spectrometers over dispersive instruments arise from two major concepts known as the throughput (or étendue) advantage as first described by Jacquinot [10] and the multiplex advantage pointed out by Fellgett [11]. Basically, both ideas deal with the total amount of usable recorded signal, or the ability to collect large amounts of energy at high resolution.

Compared with a grating-type spectrometers, the advantage of Jacquinot states that in the case of the interferometer an extended source at the input or entrance aperture does not reduce significantly the resolution. Assuming the same area of the aperture, the same gathering ability of the diverging light source and the same resolving power, then about 200 times more power can be put through the interferometer than through an ideal grating spectrometer [4, p. 22].

Compared with grating-type spectrometer, the advantage of Fellgett tells that, all along the interferogram, the interferometer receives information about the entire spectral range. Assuming the same recording time and the same resolving power, then the signal-

to-noise ratio (SNR) in the spectrum obtained with an interferometer raises with the amount of spectral elements, whereas it stays constant with a grating spectrometer. The multiplex principle can be expressed as [4, p. 24]

$$\frac{(\mathrm{SNR})_\mathrm{I}}{(\mathrm{SNR})_\mathrm{G}} = \sqrt{M}, \tag{2.1}$$

where $(\mathrm{SNR})_\mathrm{I}$, $(\mathrm{SNR})_\mathrm{G}$ are the signal-to-noise ratios of the interferometer and of the grating, respectively and M is the number of spectral elements. It should be added that this consideration is only true if the considered noise is additive, i.e. if the noise is independent of the signal level.

2.1 Interferogram and spectrum

In Fourier transform spectroscopy, the spectrum of a source is obtained from the measurement of the complex degree of coherence between two interfering waves as the path difference is varied in a two-beam interferometer (Fig. 2.1). The radiation of the source is divided into two beams passing via d_1 and d_2 respectively. After the two beams have merged, they reach the detector with a phase delay determined by the path difference $\delta = d_2 - d_1$. The intensity at a point in the interference signal is recorded as a function of the delay in the interferometer.

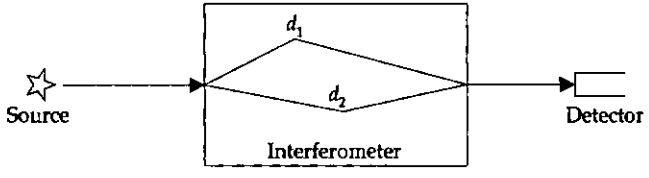

Figure 2.1: Schematic arrangement for a two-beam interferometer.

At the output of the interferometer, the recorded optical power P as a function of the path difference is proportional to the interferogram $F(\delta)$ and, as will be shown in the following discussion, the interferogram is the Fourier transform of the spectrum of the incident light. Therefore, since the Fourier transform is a reciprocal operation, one has only to take the Fourier transform of the interferogram to recover the spectrum. An interesting method, the *visibility technique*, has been developed by Michelson in order to recover the spectrum from the envelop of the interferogram. For more details see reference [3]. However, the measurement of the visibility only leads to the recovery of a spectrum which is symmetric with respect to its central frequency.

Suppose a two-beam interferometer which is perfectly symmetric, i.e. the optical and geometrical path differences are equal, and assume that the interferometer receives a monochromatic radiation of wavenumber σ_0 with a spectral component of power B_0, the

power P at the output of the interferometer will vary as

$$P(\delta) = B_0 \cos^2[\pi\sigma_0\delta], \tag{2.2}$$

where

$$\sigma = 1/\lambda. \tag{2.3}$$

Using a trigonometric relation, Eq. (2.2) can be rewritten as

$$P(\delta) = \frac{1}{2}B_0 + \frac{1}{2}B_0 \cos[2\pi\sigma_0\delta]. \tag{2.4}$$

The signal $P(\delta)$ corresponds to the time-averaged value of a radiant flux density integrated over the detector area at a specific path difference δ.

We define the interferogram

$$F(\delta) = B_0 \cos[2\pi\sigma_0\delta] \tag{2.5}$$

as the variable part of the output signal P.

If the interferometer is illuminated by several monochromatic lines, each radiation creates a similar cosinusoidal modulation and the resulting interferogram is the sum of all modulations:

$$F(\delta) = \sum_{\sigma_m} B_m \cos[2\pi\sigma_m\delta]. \tag{2.6}$$

Logically, in case of a continuous spectrum spreading from σ_1 to σ_2, the interferogram becomes

$$F(\delta) = \int_{\sigma_1}^{\sigma_2} B(\sigma)\cos[2\pi\sigma\delta]\mathrm{d}\sigma, \tag{2.7}$$

where $B(\sigma) = \mathrm{d}P(\sigma)/d\sigma$ is the power spectral density. $B(\sigma)\mathrm{d}\sigma$ is the power contained in the interval σ to $\sigma + \mathrm{d}\sigma$. The total power in the spectrum, or the total quantity of radiation in the signal, corresponds to the mean value

$$\lim_{\Delta\to\infty} \frac{1}{2\Delta}\int_{-\Delta}^{\Delta} P(\delta)\mathrm{d}\delta = \int_0^{\infty} B(\sigma)\mathrm{d}\sigma \doteq P_0, \tag{2.8}$$

of the output signal $P(\delta)$.

The most widely used two-beam interferometer in FTS is the *Michelson interferometer*; some basic setups are shown in Fig. 2.3. The path difference is created either by the motion or the tilt of one mirror with respect to the other.

2.1.1 Interference function

We describe now the previous considerations by introducing the concept of *coherence*, as well as the fundamental relation that governs FTS, known as the Wiener-Kintchine theorem.

Coherence is differentiated into temporal and spatial coherence. When considering *temporal coherence*, we are concerned with the ability of a light beam to interfere with a time-delayed version of itself. We refer to such a division as *amplitude splitting*. If we are

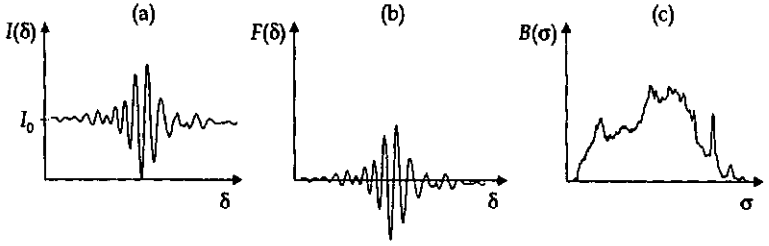

Figure 2.2: Relation between (a) the detected signal of a two-beam interferometer, (b) the interferogram and (c) the power spectrum.

concerned with the ability of a light beam to interfere with a spatially shifted version of itself, we are considering *spatial coherence*. We refer to this type of division as *wavefront splitting*. In this section we discuss temporal coherence.

For clarity reasons, it is more appropriate to switch to a time notation of the useful parameters: the light frequency ν and the retardation τ.

Quasi-monochromatic analytical light source

Assume that the light source is a quasi-monochromatic radiation produced by an optical disturbance at a single point, and let

$$u(t) = \alpha(t)\exp[i2\pi\nu_0 t] \tag{2.9}$$

be the analytical signal representation of the emitted light, where $\alpha(t) = a(t)\exp[i\phi(t)]$ is the *complex amplitude* or, *time-varying phasor amplitude* [12, p. 104] representing the real amplitude (or envelope) $a(t)$ and the phase $\phi(t)$.

In a two-beam interferometer, $u(t)$ is split in two parts $u_1(t) = s_1 u(t)$ and $u_2(t) = s_2 u(t+\tau)$ as shown in Fig. 2.4. s_1 and s_2 are real numbers determined by the losses in the two branches (including losses due to the transmission of the optical components and, for a Michelson interferometer, the fact that half of the incoming radiation can get out through the entrance).

After the recombination of the two beams, the instantaneous intensity $I(t,\tau)$, or radiant flux density, at the output of the interferometer becomes

$$I(t,\tau) = |u_1 + u_2|^2 = |u_1|^2 + |u_2|^2 + 2\mathrm{Re}\{u_1 u_2^*\}, \tag{2.10}$$

that is

$$I(t,\tau) = s_1^2|u(t)|^2 + s_2^2|u(t+\tau)|^2 + 2s_1 s_2 \mathrm{Re}\{u(t)u^*(t+\tau)\}. \tag{2.11}$$

Real source

If the optical disturbance introduced previously is emitting light in a certain statistical manner, it is then necessary to introduce the concept of *random process*. In fact, the

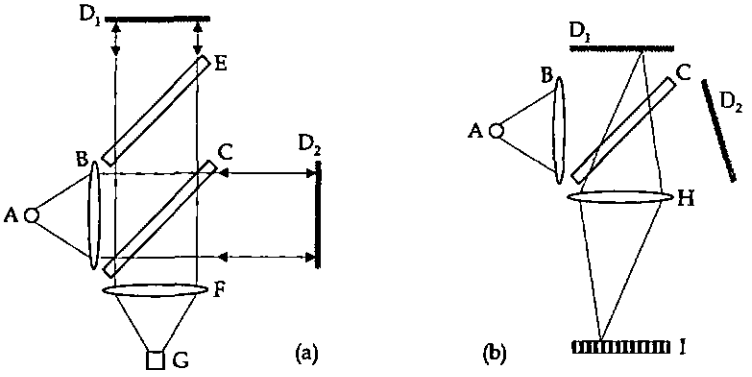

Figure 2.3: Two different configurations of a Michelson interferometer used for Fourier spectroscopy. A: Source; B: Collimator; C: Beamsplitter; D_1: Fixed mirror. (a) In the *scanning* configuration, the phase delay is generated by the movable mirror (D_2). If a perfectly symmetric interferogram is desired, the use of a compensator (E) is necessary. F: Condensator; G: single pixel detector. (b) In the *stationary* configuration, the phase delay is generated by the tilt of the second mirror (D_2) and therefore the interferogram is spread in space. With this configuration, a photo-detector array (I) is needed. The lens (H) is used to image the interference plane onto the detector in order to minimize the effect of the source size.

wave amplitude emitted by any real source has properties that change with time in an unpredictable way to some degree; in other words, a light source is not a single disturbance but a random function of time. Therefore, it becomes important to study the role played by the statistical properties of light, since they determine the outcome of most optical experiments. In many practical cases, an incomplete description in terms of second-order averages is sufficient. Elements of statistical optics, including a description of random processes, are given in appendix A.

We have discussed the behaviour of a single analytical function $u(t)$ representing an optical disturbance. Consider now an ensemble U of random functions with each sample function being typical of the entire ensemble. U is said to be a random process and u one sample function. The randomness is contained in the complex amplitude, or phasor $\alpha(t)$ (Fig. 2.5) and is given by a certain probability distribution depending on the statistical properties of the ensemble.

Considering a real source, the instantaneous intensity I given by Eq. (2.11) will become an averaged intensity $I_D = < I >_T$ over the integration time T of the detector (e.g. $T \approx 1/20$ s, for the human eye [13, p. 467]):

$$I_D(\tau) = s_1^2 < |u(t)|^2 >_T + s_2^2 < |u(t+\tau)|^2 >_T + 2 s_1 s_2 \mathrm{Re}\{\underbrace{< u(t) u^*(t+\tau) >_T}_{\Gamma(\tau)}\}. \qquad (2.12)$$

Note that the detector has a certain finite area over which the signal is integrated. The

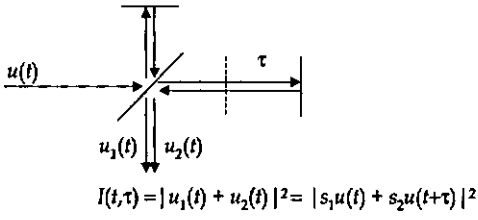

Figure 2.4: Principles of Fourier transform spectroscopy using a two-beam interferometer. τ is the difference of the time of flight between the two branches of the interferometer ($\tau = \delta/c$, where δ is the path difference).

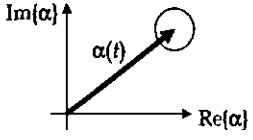

Figure 2.5: Random phasor with a contour of constant probability having a certain standard deviation.

complex function $\Gamma(\tau)$ is called the *temporal coherence function* and is the *time autocorrelation function* of the analytical signal $u(t)$ (see Eq. (A.16)). For a delay $\tau = 0$, Γ is real and the quantity

$$\Gamma(0) = I_0 = <|u(t)|^2>_T \tag{2.13}$$

is equal to the total spectral power of the incoming radiation. We can then rewrite the detected intensity as

$$I_D(\tau) = (s_1^2 + s_2^2)I_0 + 2s_1 s_2 \mathrm{Re}\{\Gamma(\tau)\}. \tag{2.14}$$

For $\tau = 0$ the temporal coherence is maximum and the detected intensity is $I_D(0) = (s_1 + s_2)^2 I_0$. When $\tau \to \pm\infty$, one is in an incoherent regime and $\mathrm{Re}\{\Gamma(\pm\infty)\} = 0$, which means that no interference is detected as a function of τ, i.e. $I_D(\pm\infty) = (s_1^2 + s_2^2)I_0$.

Note that if U is a stationary random process, Γ (and consequently I_D) are independent of time, in other words, the statistical properties are invariant with respect to time translation. As a matter of fact, Γ is only a function of the time difference τ.

It is convenient to define the *complex degree of coherence*

$$\gamma(\tau) = \frac{\Gamma(\tau)}{\Gamma(0)}, \tag{2.15}$$

which is the normalized version of the coherence function. The degree of coherence quantifies the temporal coherence of the incoming radiation. Its modulus $|\gamma(\tau)|$ is the *visibility curve*, or *envelope* of the interferogram, and it has values between 0 and 1, with $|\gamma(0)| = 1$.

Equation (2.14) is then expressed as

$$I_D = (s_1^2 + s_2^2) I_0 \left[1 + \frac{2 s_1 s_2}{(s_1^2 + s_2^2)} \mathrm{Re}\{\gamma(\tau)\} \right]. \tag{2.16}$$

In order to reach an analytical expression for the interferogram, we express the time autocorrelation function by introducing the representation for a quasi-monochromatic radiation from Eq. (2.9):

$$\Gamma(\tau) = \frac{1}{T} \int_0^T \alpha(t) \exp[i 2\pi\nu_0 t] \alpha^*(t+\tau) \exp[-i 2\pi\nu_0 (t+\tau)] = <\alpha(t)\alpha^*(t+\tau)>_T \exp[-i 2\pi\nu_0 \tau]. \tag{2.17}$$

By representing $\Gamma(\tau)$ in a complex manner (Fig. 2.6), it follows that

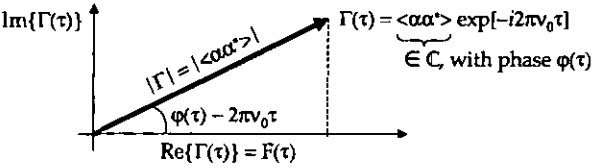

Figure 2.6: Complex representation of the temporal coherence function $\Gamma(\tau)$ for a quasi-monochromatic radiation. The time autocorrelation function $< \alpha(t)\alpha^*(t+\tau) >_T$ of the complex amplitude $\alpha(t)$ of the analytical signal representation is a complex function having a phase $\phi(\tau)$. The interferogram $F(\tau)$ is the real part of the function of coherence.

$$F(\tau) = |\Gamma(\tau)| \cos[\phi(\tau) - 2\pi\nu_0\tau]. \tag{2.18}$$

If the frequency band under investigation is narrow, then the envelope $|\Gamma|$ varies much slower than the modulation $\cos[2\pi\nu_0\tau]$.

Contrast

The *contrast* in the vicinity of the path difference τ is defined as the visibility curve $|\gamma(t,\tau)|$, taking into account the losses in the interferometer in each branch of the interferometer:

$$C_\tau = \frac{I_{\max}(\tau) - I_{\min}(\tau)}{I_{\max}(\tau) + I_{\min}(\tau)} = \frac{2 s_1 s_2}{(s_1^2 + s_2^2)} |\gamma(\tau)|. \tag{2.19}$$

2.1.2 Power spectrum and Wiener-Kintchine theorem

In order to continue the discussion, we introduce the notion of spectral density, since we wish to find the spectral distribution that characterizes the entire random process. In particular, we bring up the notions of energy and power spectral densities.

Again, let $u(t)$ (Eq. (2.9)) be our sample function of a *stationary* (section A.2.1) *linearly filtered* (section A.3.2) random process $U(t)$, then:

- if $u(t)$ is Fourier transformable (Eq. (A.17)) with $\hat{u}(\nu)$ being the Fourier transform of $u(t)$, then the *energy spectral density* of $u(t)$, in terms of the *ensemble average* $<.>_E$ (section A.2.1), is

$$E(\nu) = <|\hat{u}(\nu)|^2>_E; \tag{2.20}$$

- if $u(t)$ has a finite average power (Eq. (A.21)), then the truncated function $u_T(t) = \text{rect}(2T, t)u(t)$ is Fourier transformable, with $\hat{u}_T(\nu)$ being the Fourier transform of $u_T(t)$, and then the *power spectral density* of $u(t)$ is

$$B(\nu) = \lim_{T\to\infty} \frac{<|\hat{u}_T(\nu)|^2>_E}{2T}. \tag{2.21}$$

The power spectral density $B(\nu)$ has the following properties [12, p. 70] (the same properties can be derived for the energy spectral density $E(\nu)$):

1. $B(\nu) \geq 0$; the power spectral density is positive and real-valued.

2. $B(-\nu) = B(\nu)$; the power spectral density is an even function and $U(t)$ is a real-valued random process.

3. $\int_{-\infty}^{\infty} B(\nu)\mathrm{d}\nu = <u^2>_t$,

where $<.>_t$ is the *time average* (section A.2.1). The third is obtained by using Parceval's theorem and says that the energy is conserved:

$$\begin{aligned}
\int_{-\infty}^{\infty} B(\nu)\mathrm{d}\nu &= \int_{-\infty}^{\infty} \left[\lim_{T\to\infty} \frac{<|\hat{u}_T(\nu)|^2>_E}{2T}\right] \mathrm{d}\nu \\
&= \lim_{T\to\infty} \frac{1}{2T} < \underbrace{\int_{-\infty}^{\infty} |\hat{u}_T(\nu)|^2 \mathrm{d}\nu}_{\int_{-\infty}^{\infty} u_T^2(t)\mathrm{d}t,\ \text{Parceval}} >_E \\
&= \lim_{T\to\infty} \frac{1}{2T} \int_{-T}^{T} <u_T^2(t)>_E \,\mathrm{d}t \\
&= <u^2>_t .
\end{aligned}$$

It is shown in section A.4 that, for a stationary random process, there exists a relationship between the time autocorrelation function and the power spectral density of the source. This relationship is known as the *Wiener-Kintchine theorem*:

$$B(\nu) = \int_{-\infty}^{\infty} \Gamma(\tau) \exp[i2\pi\nu\tau]\mathrm{d}\tau. \tag{2.22}$$

The reader can find the demonstration of this theorem in section A.4.1. This theorem says that the temporal coherence function and the power spectral density are linked by a Fourier transform.

2.1.3 Temporal coherence of a random process

Because of the reciprocity of the Fourier transform, and since the random process $U(t)$ is assumed to be stationary (note that $U(t)$ does not need to be ergodic, see section A.2.1), it follows from Eq. (2.22) that the temporal coherence function $\Gamma(\tau)$ is given by

$$\Gamma(\tau) \doteq < u(t+\tau)u^*(t) > = \int_{-\infty}^{\infty} B(\nu) \exp[-i2\pi\nu\tau] \mathrm{d}\nu, \tag{2.23}$$

and, consequently, the complex degree of coherence $\gamma(\tau)$ becomes

$$\gamma(\tau) = \frac{\int_{-\infty}^{\infty} B(\nu) \exp[i2\pi\nu\tau] \mathrm{d}\nu}{\int_{-\infty}^{\infty} B(\nu) \mathrm{d}\nu}, \tag{2.24}$$

where $\int_{-\infty}^{\infty} B(\nu)\mathrm{d}\nu = \Gamma(0)$ is the total power in the spectrum of the source.

Time of coherence

The *time of coherence* τ_c of the incoming radiation can be defined as [12, p. 167]

$$\tau_c = \int_{-\infty}^{\infty} |\gamma(\tau)|^2 \mathrm{d}\tau. \tag{2.25}$$

The time of coherence tells whether the radiation has a high or a low temporal coherence. A quasi-monochromatic light wave has a long time of coherence. This can be seen with an interferometric measurement, because of the large number of oscillations under the envelope. On the contrary, if the modulation vanishes rapidly with τ, the time of coherence is small.

For instance, if the spectrum has a rectangular shape, as shown in Fig. 2.7, the time of coherence is [12, p. 168]

$$\tau_c = \Delta\nu^{-1}, \tag{2.26}$$

where $\Delta\nu$ is the spectral width. In the same way, the time of coherence of a laser line

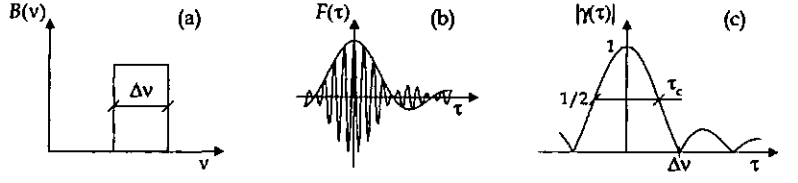

Figure 2.7: Relation between (a) the width $\Delta\nu$ of a rectangular spectrum $B(\nu)$, the envelope of the interferogram, shown in (b) and (c) and the time of coherence τ_c defined here as the width at half maximum of the envelope.

having a Gaussian spectral distribution is

$$\tau_c = 0.664\Delta\nu^{-1}, \tag{2.27}$$

where $\Delta\nu$ is the spectral width.

Sometimes it is preferable to use the length of coherence

$$l_c = \tau_c / c, \tag{2.28}$$

because we often measure the interferogram as a function of path difference, where c is the speed of light in the vacuum corresponding to τ_c.

2.2 Recovery of the power spectrum

In the previous section we presented the Wiener-Kintchine theorem which relates the autocorrelation function of a signal with its spectrum; we remind that $\Gamma(\tau)$ is a complex function and $B(\nu)$ a real-valued function. In addition, we have seen that at the output of a two-beam interferometer, the detected modulation is the real part of the time autocorrelation function, named the interferogram.

In this section, we shall show how to retrieve the physical spectrum from the interferogram.

2.2.1 Physical and mathematical spectrum

The spectrum retrieved from the interferogram via Wiener-Kintchine is defined for frequencies from $-\infty$ to ∞. On the other hand, we know that the spectrum of a given light source is physical, and therefore defined for positive frequencies only.

Assuming a symmetric interferometer, the result of the complex Fourier transform of Γ and the result of the cosine transform of $\mathrm{Re}\{\Gamma\}$ (we name it $\Gamma^{(r)}$) are equal. Equation (2.22) can then be written as

$$\begin{aligned} B(\nu) &= \int_{-\infty}^{\infty} \Gamma^{(r)}(\tau) \cos[2\pi\nu\tau] \mathrm{d}\tau \\ &= 2\int_{0}^{\infty} \Gamma^{(r)}(\tau) \cos[2\pi\nu\tau] \mathrm{d}\tau, \quad -\infty < \nu < \infty, \end{aligned} \tag{2.29}$$

with $B(\nu)$ being symmetric. It can be considered as the even part of the physical spectrum, which can be defined as the sum of an even an odd part, as shown in Fig. 2.8.

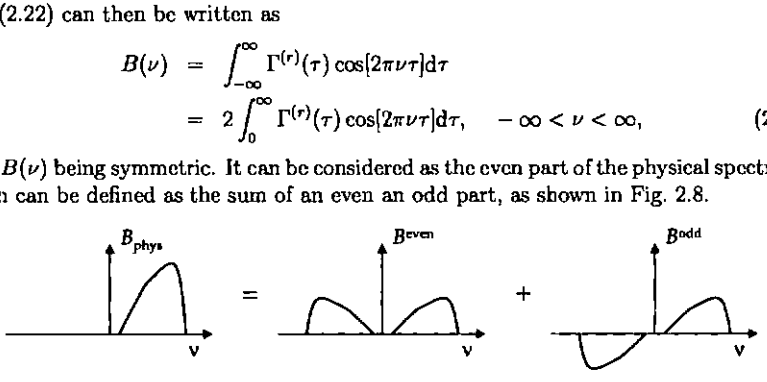

Figure 2.8: Convenient representation of the physical spectrum by the sum of an even and an odd function.

With these assumptions, we find that

$$B_{\mathrm{phys}}(\nu) = 4\int_{0}^{\infty} \Gamma^{(r)}(\tau) \cos[2\pi\nu\tau] \mathrm{d}\tau, \quad \nu > 0, \tag{2.30}$$

which means that with a symmetric interferometer, the physical spectrum defined for positive frequencies is retrieved by means of the cosine Fourier transform of the real part of the autocorrelation function, taking into account only a positive time delay τ. The factor in front of the integral is of little importance, since we are more interested in studying the 'shape' of a spectrum than its quantity.

Wavelength domain

In terms of the path difference $\delta = \tau c$, Eq. (2.30) becomes

$$B(\sigma) = 4 \int_0^\infty F(\delta) \cos[2\pi\sigma\delta] \mathrm{d}\delta, \tag{2.31}$$

where $\sigma = \nu/c = 1/\lambda$ are the wavenumber and λ the wavelength. For practical reasons, we may represent the power spectral density also in the wavelength domain. Since the power contained in an infinitely small portion of the spectral density must be equal for any representation of the Fourier frequency, it follows that

$$|B_\lambda(\lambda)\mathrm{d}\lambda| = |B_\sigma(\sigma)\mathrm{d}\sigma| = |B_\nu(\nu)\mathrm{d}\nu|, \tag{2.32}$$

where

$$\mathrm{d}\sigma = -\frac{1}{\lambda^2}\mathrm{d}\lambda. \tag{2.33}$$

B_λ and B_σ are two distinct power spectral densities.

2.2.2 Complex Fourier transform

So far it has been assumed that the interferogram $F(\tau)$ is a symmetric function. This is the reason why one needs only to carry out a cosine Fourier transform for positive values of τ. In other words, the interferogram needs only to be recorded on the positive side of the zero path difference.

Nevertheless, for several reasons that will be listed below and that are intrinsic to the interferometer, the measured interferogram may not necessarily be symmetric. In those particular cases, we may perform the complex Fourier transform on the complete interferogram, that is the two-sided interferogram. As a matter of fact, the result will be complex, which does not mean that the spectrum is complex. The result of the complex Fourier transform will qualify and quantify the asymmetry of the interferometer. The complex transform of an asymmetric interferogram gives the power spectral density, as well as the phase shift proper to each frequency, which has been introduced by the interferometer. With an asymmetric interferogram, we have

$$\hat{F}(\nu) = \int_{-\infty}^{\infty} F(\tau) \exp[i2\pi\nu\tau] \mathrm{d}\tau, \tag{2.34}$$

where $\hat{F}(\nu)$ is the complex Fourier transform of $F(\tau)$. The power spectrum $B(\nu)$ is then given by

$$B(\nu) = |\hat{F}(\nu)| = \sqrt{\hat{F}_{\cos}^2 + \hat{F}_{\sin}^2} \tag{2.35}$$

and the phase delay (for each frequency) introduced by the interferometer is

$$\Phi(\nu) = \tan^{-1} \frac{\mathrm{Im}\{\hat{F}(\nu)\}}{\mathrm{Re}\{\hat{F}(\nu)\}}. \tag{2.36}$$

If the interferogram is symmetric, all cosinusoidal modulations corresponding to a particular frequency, add constructively at $\tau = 0$, and therefore a cosine Fourier transform is sufficient; thus $B = \hat{F}$ and $\Phi = 0$.

The two-sided transform gives the positions of bands correctly, as well as the absolute power levels [7, p. 187]. Despite this fact, the Fourier spectroscopist usually tries to avoid any type of distortion in order to record one-sided interferograms. The reason is that one might be limited by the number of sampling points to be processed when performing high resolution spectroscopy. Additionally, the recording time is half. For situations with low SNR ratios, the cosine transform is preferred to the complex transform, since, in the latter case, all components of the noise are positive (due to the modulus of the transform), whereas in the cosine transform, the noise averages to zero [1, 14].

2.2.3 Asymmetric interferograms

As mentioned above, the function of coherence Γ is an even function. The reason why the measured interferogram is asymmetric is only due to the interferometer. In this section we discuss different types of asymmetries, causing phase shift or phase errors, as well as the manner to retrieve the power spectrum under these conditions.

An interferometer is said asymmetric either when

- the two branches have different transmission properties,
- no sampling point hits the zero path difference,
- *the span used to record the interferogram, is not centered.*

In addition, the phase delay arising from the path difference, can be nonlinear. In such a situation, we refer to a distorted interferogram. The distinction between asymmetry and distortion is relevant, since in the first case, a complex Fourier transform gives the power spectrum, but in the second case, the phase has to be corrected.

Asymmetry and phase correction are subjects that have been treated by many authors. Particularly in high precision FTS (besides the high attention that must be paid to the mechanical, optical and electronics design of the spectrometer) the algorithms used to process the recorded interferogram play a critical role. This includes phase correction and phase discrepancies, correction of asymmetric interferograms, chirping, phase correction of emission lines, correction of instrument line-shape distortions, interpolation of the zero path difference, drive nonlinearities. The subject is vast and the reader can refer to the following incomplete list of publications [1, 15, 16, 17, 18, 19, 20, 21, 22, 23].

On the contrary, our specific applications require moderate resolution, and therefore we focus on the aspects listed at the beginning of this section. They will be discussed in a general way and then presented in a practical way in the following chapters. Due to the fact that our devices are not optimized to carry out one-sided interferograms, we always

record two-sided interferograms. Indeed, the center of our interest is focused on easily mounted, non-sensitive and non-perfectly adjusted interferometers.

For the treatment of asymmetry due to the dispersion or to the sampling position of the zero path difference, the complex Fourier transform gives the correct spectrum. It is an advantage, because it eliminates any dependence of the computed spectrum on the location of the origin. If one would perform one-sided interferograms, then the origin had to be known very accurately. Reference [24] gives a complete description of distortions in the spectrum due to an offset in the origin of the interferogram.

Offset at the center of the span

The span is the window, in terms of path difference, used to record the interferogram. The problem of using a shifted span in which the centre of the span and the zero of the geometrical path difference do not coincide, is treated in reference [7, p. 181–182]. The result shows that if the offset is small compared to the span, then the terms, introduced by the offset, vanish when the modulus of the complex Fourier transform is taken. On the other hand, variations will appear in the spectrum, which increase with the offset.

Note that the offset in the zero path difference and the offset in the span are two different problems.

Dispersion

By using a dispersive interferometer, it may be possible to determine the thickness d of a plate placed in one branch of the interferometer. In this case the interferogram is

$$I(\delta) = \int_{-\infty}^{\infty} B(\sigma)\cos[2\pi\delta\sigma - \Phi(\sigma)]\mathrm{d}\sigma, \tag{2.37}$$

where

$$\Phi(\sigma) = 2\pi 2dn(\sigma)\sigma \tag{2.38}$$

is the phase shift introduced by the plate having a dispersive index of refraction of $n(\sigma)$.

In conventional FTS, asymmetry due to a dispersive effect in one branch of the interferometer is usually avoided by mean of a compensation plate of the same thickness and material than the beam splitter, as shown in Fig. 2.3(a).

Distortion

Path difference nonlinearities cannot simply be compensated by using a complex Fourier transform. In fact, in such a case δ is no more a linear ramp. In practice, the difference between each sampling point, in terms of path difference, is not constant. Then, the spectrum can be retrieved by

$$B(\sigma) = \int_{-\infty}^{\infty} F(\delta)\exp[i2\pi\sigma(\delta - \Delta(\delta))]\mathrm{d}\delta, \tag{2.39}$$

where $\Delta(\delta)$ is the path discrepancy as a function of the path difference. The function $\Delta(\delta)$ can be obtained by an interferometric measurement.

Of course, the ideal procedure is to remove the cause of phase error in the interferometer itself. This is the reason why generally, in high precision FTS, the scanning of the mirror is operated by means of self-controlled drive systems (e.g. piezo-electric devices in combination with an interferometric control, which is coupled with feed-back electronics).

2.2.4 Sampling

An additional important feature in recovering the power spectrum comes from the fact that the signal is sampled in order to be recorded. In this section, we will show that sampling the interferogram does not alter the spectrum, but attention has to be paid to the sampling interval with respect to the band width of interest. In addition, we will show the influence of the finite number of samples on the spectrum.

The sampling theorem

We refer to the work of Shannon [25]. He showed that for a finite spectrum, the entire information contained in its continuous interferogram can exactly be contained in a sampled interferogram. In practical cases, the measured spectrum is never infinite, since it is always limited either by the emission itself, by the transmission of the materials, or the spectral sensitivity of the detector.

Consider the sampled interferogram

$$F_b(\delta) = F(\delta)W(b,\delta), \tag{2.40}$$

where $W(b,x)$ is the comb function [26]

$$W(b,x) = b\sum_{k=-\infty}^{\infty} \varrho(x-kb). \tag{2.41}$$

having Dirac peaks ϱ at the positions kb (k is an integer), also called the shah function. With this representation, the sampled interferogram can be written as

$$F_b(\delta) = b\sum_{k=-\infty}^{\infty} F(\delta)\varrho(\delta-kb). \tag{2.42}$$

By the convolution theorem, and knowing that the Fourier transform of $W(b,x)$ is $bW(1/b,m)$ [26] (m are the Fourier frequencies), the Fourier transform of the sampled function becomes

$$\hat{F}_b = bW(1/b,\sigma) \circ B(\sigma) \equiv B_{1/b}(\sigma), \tag{2.43}$$

where $\circ$ stands for the convolution operation. This relation shows that the power spectrum is repeated at intervals $1/b$. Now, if the true spectrum is band-limited so that $B(\sigma) \equiv 0$ for $\sigma > \sigma_{\max}$, it can be represented as

$$B(\sigma)\mathrm{rect}(\sigma_{\max}/2, \sigma - \sigma_{\max}/2) = bB_{1/b}(\sigma), \quad 0 \le \sigma < \sigma_{\max}. \tag{2.44}$$

where $\sigma_{\max}$ is the cutoff frequency. This means that the analogue band-limited spectrum $B(\sigma)$ can be obtained unambiguously from a sampled function $F_b(\delta)$, as illustrated in Fig. 2.9. Note that for $\sigma_{\max} < 1/2b$ (no aliasing effect), the analogue interferogram $F(\delta)$ itself can unambiguously be reconstructed by means of its sampled version $F_b(\delta)$.

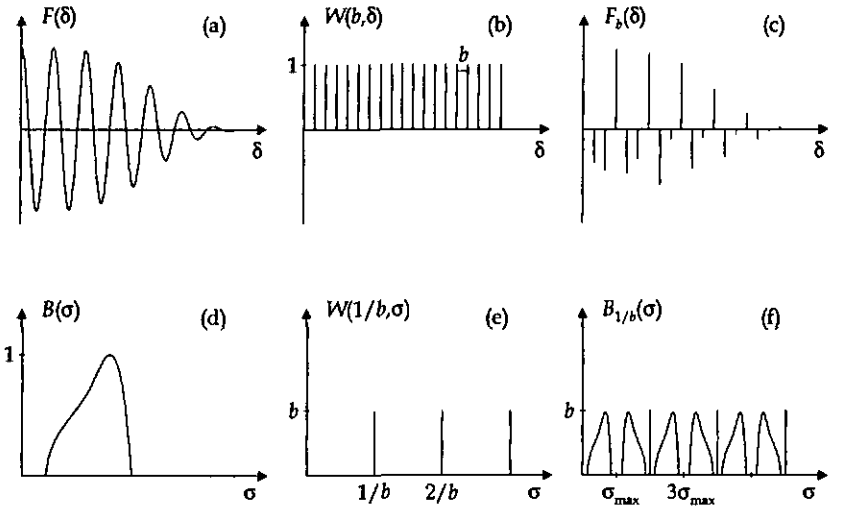

Figure 2.9: (a) Continuous interferogram; (b) Comb function (or shah function $W(b,x)$); (c) Sampled interferogram; (d), (e) and (f) Fourier transform of (a), (b), respectively of (c).

Necessary number of sampling points

The evaluation of a given spectral extension $\Delta\sigma$ at a given resolution relies on two parameters: the optical path maximum δ_{max} and the sampling interval b. Of course, they are related to the number of sampling points N by $\delta_{max} = Nb$. It follows from Eq. (2.44) that

$$b = 1/2\sigma_{max} = \lambda_{min}/2. \tag{2.45}$$

This result is evident, since one always needs at least two sampling points to sample the smallest modulation (λ_{min}). For larger intervals the interferogram is not sampled enough (undersampling); therefore the power spectrum cannot be recovered and aliasing effects occur.

For the choice of the number of sampling points N, the minimum desired frequency σ_{min} is relevant. Indeed, the path difference needs to be long enough to resolve σ_{min} as well. The number of samples will be

$$N = 2\Delta\sigma\delta_{max}, \tag{2.46}$$

where $\Delta\sigma = \sigma_{max} - \sigma_{min}$.

In order to illustrate this discussion, we give two numerical examples:

- Consider an application in colorimetry, with a specification of 10 nm resolution in the visible wavelength range ($\lambda_{min} = 380$ nm to $\lambda_{max} = 730$ nm, i.e. $\sigma_{min} = 1.37\ \mu m^{-1}$

to $\sigma_{max} = 2.63\ \mu m^{-1}$). Then, the necessary optical path becomes (Eq. (2.58)) $\delta_{max} = 27\ \mu m$ and the sampling interval becomes $b = 190$ nm. Therefore the required number of samples is (Eq. (2.46)) $N = 142$.

- Now, consider an application in telecommunication with the following requirements: 1 nm resolution and a spectral window extending from $\lambda_{min} = 1.40\ \mu m$ to $\lambda_{max} = 1.65\ \mu m$. Then we get $b = 700$ nm, $\delta_{max} = 1.36$ mm, and $N \approx 2000$.

Note that the effect of apodization is not taken into account in these examples. As will be shown in the next section, apodization decreases the resolution. As a consequence, δ_{max} has to be increased, as well as N, in order to achieve the same requirements. As an example, Table 2.1 shows that with a triangular apodization the width of a single frequency is enlarged by a factor of about 1.5; δ_{max} and N are increased by the same factor.

Fourier series

We have seen that a finite spectrum $B(\sigma)$ and its corresponding interferogram $F(\delta)$ can be reconstructed uniquely from each other using a convenient sampling. In addition, both functions are well-behaved periodic functions and therefore may be represented by linear series of complex periodic functions:

$$F(\delta) = \sum_{m=1}^{\infty} B(\sigma_m) \exp[-i2\pi\delta\sigma_m] \tag{2.47}$$

and

$$B(\sigma) = \sum_{n=1}^{\infty} F(\delta_n) \exp[i2\pi\delta_n\sigma], \tag{2.48}$$

where σ_m are the discrete frequencies and δ_n the discrete sample positions. Equation (2.47) is used to fabricate interferograms numerically (see next chapter) and Eq. (2.48) to retrieve the spectrum from a recorded sampled interferogram.

Of course in practice, the number of samples N is finite and we consider *finite Fourier series*. In that case, the effect is similar to the truncation of the interferogram discussed in section 2.3.1.

2.3 Instrumental function

The instrumental function, also called apparatus function, instrument profile or instrument line-shape, is defined as the power spectral density which we would obtain for a rigorously monochromatic radiation. The instrumental function includes any type of influence of the instrument over the spectrum. In this section, we will discuss the following effects and their spectral responses:

- Truncation: the interferogram is recorded over a finite span limited by the optical path maximum δ_{max}.

- Apodization: decreases the effect of truncation and of low S/N ratio at the borders of the interferogram.

- Field of view: the influence of the size of a circular source (or entrance aperture), in terms of angle of acceptance.

In a very general manner, following the concept of Fourier optics (linear systems), the instrument profile can be represented by a function $h(\sigma)$, called the spectral *impulse response*. Then, the spectrum can be written as

$$B'(\sigma) = h(\sigma) \circ B(\sigma), \tag{2.49}$$

where $B(\sigma)$ is the spectrum issued from the true interferogram $F(\delta)$. From the convolution theorem, the multiplication of two functions is the convolution of their respective Fourier transforms. Therefore, the transfered interferogram $F'(\delta)$ becomes

$$F'(\delta) = H(\delta)F(\delta), \tag{2.50}$$

where $H(\delta)$ is the *transfer function* of the instrument.

Resolution

Strictly speaking, *resolution* represents the smallest spectral interval that can be discerned.

It is convenient to describe the quality of the resolution in terms of *resolving power*

$$R = \frac{\sigma}{\delta\sigma}, \tag{2.51}$$

which is a measure of the ability to separate neighbouring lines, where $\delta\sigma$ is the resolution in terms of width of the instrument function $h(\sigma)$. For a given spectral range $\Delta\sigma = \sigma_{\max} - \sigma_{\min}$, the resolving power

$$M = \frac{\Delta\sigma}{\delta\sigma}. \tag{2.52}$$

represents the number of accessible spectral elements.

2.3.1 Truncation

If the interferogram is measured over a finite path difference range $-\delta_{\max}$ to $\delta_{\max}$, the interferogram is represented by

$$F_t(\delta) = \mathrm{rect}(\delta_{\max}, \delta)F(\delta), \tag{2.53}$$

where $\mathrm{rect}(\delta_{\max}, \delta)$ is defined to be equal to 1 for $-\delta_{\max} \leq \delta \leq \delta_{\max}$ and zero otherwise. Following Eq. (2.49), the reconstructed spectrum becomes

$$B_t(\sigma) = \mathrm{sinc}(1/2\delta_{\max}, \sigma) \circ B(\sigma), \tag{2.54}$$

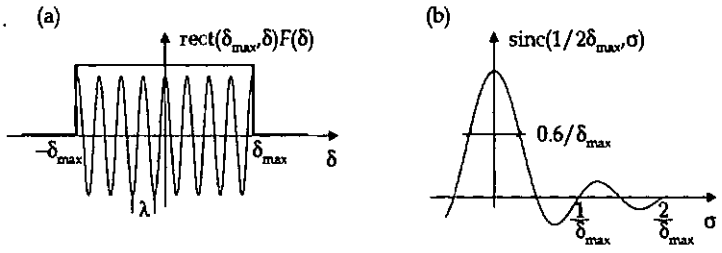

Figure 2.10: (a) Truncation of the interferogram with a rectangular function. (b) The instrumental line-shape, which is the Fourier transform of $\mathrm{rect}(\delta_{\max}, \delta)$, is a sinc function with a first zero at $1/2\delta_{\max}$.

where $\mathrm{sinc}(a, x) = \sin(\pi x/a)/(\pi x/a)$ is a function of x with a first zero at the position $x = a$. The sinc function, shown in Fig. 2.10(b), is the instrumental function associated with the truncation.

If one considers a sampled interferogram $F(\delta_n)$ truncated at the sampling position $n = N$, then the spectrum $B(\sigma)$ in Eq. (2.54) is given by the expression in Eq. (2.48). Since one knows that at the wavenumber $\sigma_m = m/2\delta_{\max}$, the $\mathrm{sinc}(1/2\delta_{\max}, \sigma_m)$ is equal to 1 for $m = 0$ and equal to 0 for $m \neq 0$, it turns out that

$$B_t(\sigma_m) = \sum_{n=1}^{N} F(\delta_n) \exp[i2\pi\delta_n\sigma_m] = B(\sigma_m). \tag{2.55}$$

The choice of the criterion that will determine the resolution is discussed now. The theoretical resolution can be defined as [1, p. 55]

$$\delta\sigma = 0.5/\delta_{\max}, \tag{2.56}$$

which corresponds to the separation of two lines whose interference has a beat frequency being zero at $\delta_{\max}$. In this case, the resolving power (Eq. (2.51)) will be

$$R = 2\sigma\delta_{\max} = 2K_\sigma, \tag{2.57}$$

where K_σ is the number of recorded modulation period for a given wavenumber σ and a given path difference maximum $\delta_{\max}$. For a grating spectrometer, the resolving power is the number of grating periods that are illuminated. By analogy, in Fourier spectroscopy the resolving power is related to the number of modulation period that one can measure.

When considering a power spectrum as a function of the wavelength λ, the theoretical resolution (Eq. (2.56)) is

$$\delta\lambda = 0.5\lambda^2/\delta_{\max}, \tag{2.58}$$

which shows that the resolution decreases with the square of the wavelength. In section 3.3.2 we shall see that, with a convenient processing, it is possible to get a constant resolution as a function of the wavelength.

On the other hand we can consider, as introduced in the beginning of this section, that a certain width is associated to a given apparatus function. In our case, the full half width at maximum (FWHM) of the function $\mathrm{sinc}(0.5/\delta_{\max}, \sigma)$ is $0.603/\delta_{\max}$.

In future, when discussing the resolution, we shall keep the notion of theoretical resolution, as well as the value of the FWHM of a calculated or measured line.

2.3.2 Apodization

As seen, the main effect of truncation is the presence of secondary maxima, called *sidelobes*, in the power spectrum of a monochromatic radiation. It is the primary purpose of apodization to reduce these sidelobes [27, 28, 29]. Of course, the smaller the modulation at the position of the truncation, the lower the effect of truncation; indeed, for smooth broadband spectra, the effect of truncation vanishes and the use of apodization will have a different purpose, that is to diminish the effect caused by poor signal-to-noise ratio at the borders of the interferogram.

Any well-chosen function can be used as apodizing function $A(\delta)$ to multiply the interferogram. The modified spectrum is the given by the convolution of the original spectrum with the Fourier transform $\hat{A}(\sigma)$ of the apodization function $A(\delta)$. Therefore, it is the shape of $\hat{A}(\sigma)$, which determines the instrument function and, of course, the resolution. The choice of the apodization depends on how much resolution one can concede for the desired effect; thus a trade-off has to be found.

As a simple example, let us consider a triangular apodization as shown in Fig. 2.11. After apodization, the interferogram is $\mathrm{triang}(\delta_{\max}, \delta)F(\delta)$, where $\mathrm{triang}(\delta_{\max}, \delta) = 1 -$

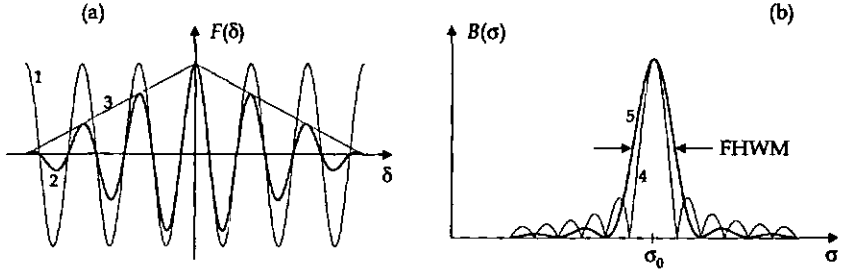

Figure 2.11: (a) Interferogram of (1) a truncated monochromatic radiation of wavenumber σ_0 and (2) the same radiation after a (3) triangular apodization. (b) Power spectra of the cases (1) and (2), named (4) and (5) respectively. The width FWHM is $0.603/\delta_{\max}$ for (4) and $0.886/\delta_{\max}$ for (5) (see Table 2.1).

$|\delta|/\delta_{\max}$ is a triangular function with a first zero at $\delta_{\max}$. Because a triangle is the convolution of two rectangles, the resulting spectrum becomes

$$B_a(\sigma) = B(\sigma) \circ \mathrm{sinc}^2(1/\delta_{\max}, \sigma). \tag{2.59}$$

In this case, the instrumental function is a sinc^2 function. Here the width of the line-shape is $0.886/\delta_{\max}$.

Table 2.1 shows the deterioration of resolution, in terms of percentage increase of the full half width at maximum (FWHM) of a monochromatic source, for some common apodization filters. The increase of the FWHM is compared with an unapodized spectrum recorded with a given path difference maximum $\delta_{\max}$. The height of the first sidelobe is given in percent of the principal maximum. We notice that the stronger the

Table 2.1:

Apodizing filter		FWHM	First sidelobe height
Unapodized	$\mathrm{rect}(\delta_{\max}, \delta)$	$0.603/\delta_{\max}$	22%
Triangle	$1 - \lvert\delta\rvert/\delta_{\max}$	$0.886/\delta_{\max}$	4.7%
Cosine	$\cos[\pi\delta/2\delta_{\max}]$	$0.820/\delta_{\max}$	7.1%
Happ-Genzel [30]	$0.54 + 0.46\cos[\pi\delta/\delta_{\max}]$	$0.908/\delta_{\max}$	0.6%
Blackman-Harris [30]	$0.42 + 0.50\cos[\pi\delta/\delta_{\max}]$		
	$+0.08\cos[2\pi\delta/\delta_{\max}]$	$1.150/\delta_{\max}$	0%
Gauss	$\exp[-\pi\delta^2/\delta^2_{\max}]$	$0.963/\delta_{\max}$	0%
Super Gauss	$\exp[-\pi\delta^4/\delta^4_{\max}]$	$0.823/\delta_{\max}$	10.8%

filter, the larger the width of the instrumental function and the better the suppression of the sidelobes. The best trade-off is offered by the triangular and the Happ-Genzel filters. Additionally, both filters have the advantage to become zero at the ends of the interferogram.

2.3.3 Field of view

A realistic interferometer works with an entrance slit or a source of finite size. In this section, we discuss the instrumental function of a Michelson interferometer for a circular aperture.

The important parameter in this discussion is the solid angle Ω subtended by the source at the collimator (see Fig. B.1). As seen from Fig. 2.12, for a displacement $\delta/2$ of

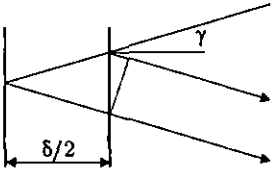

Figure 2.12: Change of path length in a two beam interferometer for a beam with oblique incidence γ.

the mirror, the optical path difference for an oblique beam of angle γ is

$$(\delta/\cos\gamma) - \delta\tan\gamma\sin\gamma = \delta\cos\gamma. \tag{2.60}$$

For $\gamma_{max} \ll \pi/2$, the interferogram for a given wavenumber σ_0 becomes

$$F(\delta) \propto \int_0^{\gamma_{max}} \cos[2\pi\sigma_0\delta\cos\gamma]\sin\gamma d\gamma, \tag{2.61}$$

and after the integration

$$F(\delta) \propto \mathrm{sinc}(1/\sigma_0(1-\cos\gamma_{max}), \delta)\cos[2\pi\delta\bar{\sigma}], \tag{2.62}$$

where

$$\bar{\sigma} = (1+\cos\gamma_{max})/2. \tag{2.63}$$

By replacing $\cos\gamma_{max} = 1 - \Omega/2\pi$, the mean wavenumber $\bar{\sigma}$ can be expressed as

$$\bar{\sigma} = \sigma_0(1-\Omega/4\pi). \tag{2.64}$$

This means that the resulting interference is a cosine modulation, shifted to a lower frequency $\bar{\sigma}$ with respect to the true frequency σ_0, and multiplied by a sinc function with a first zero at $2\pi/\sigma_0\Omega = [\sigma_0(1-\cos\gamma_{max})]^{-1}$. As shown in Fig. 2.13, the resulting spectrum

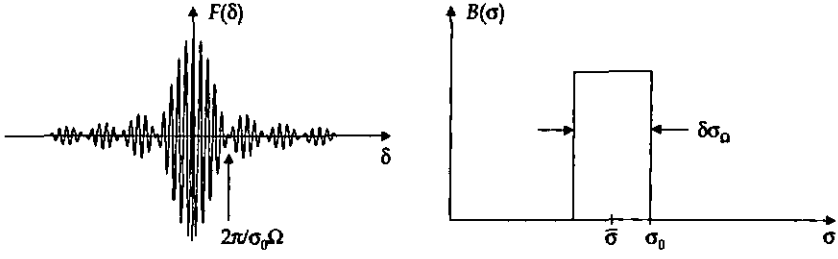

Figure 2.13: Left: Interferogram due to a circular source making a solid angle Ω with respect to the collimator. Right: Corresponding power spectrum.

is a rectangle centered at $\bar{\sigma}$ and with a width of

$$\delta\sigma_\Omega = \sigma_0\Omega/2\pi. \tag{2.65}$$

In conclusion, the instrument function is

$$B_f(\sigma) = \mathrm{rect}(\sigma\Omega/4\pi, \sigma+\bar{\sigma}). \tag{2.66}$$

2.4 Noise

The last aspect treated in this chapter is related to the effect of noise in Fourier transform spectroscopy. The interferogram signal is always accompanied by statistical errors and we want to know their effect on the spectrum. Several types of noise and their origins will be presented in this section.

Signal-to-noise ratio

The quantity that characterizes statistical fluctuations is the *standard deviation* (std), or the *variance* var = std^2 = $<(u-\bar{u})^2> = <u^2> - \bar{u}^2$, where u is a random variable and $\bar{u}$ is its mean value. The *root mean square* (RMS) value is equal to the standard deviation, if the mean value of the random variable is zero, i.e. RMS = $\sqrt{<u^2>}$.

The signal-to-noise ratio (SNR) of a random variable is defined as

$$\mathrm{SNR} = \bar{u}^2/\mathrm{var} = \bar{u}^2/\,<(u-\bar{u})^2>\,. \tag{2.67}$$

In the case of a detector generating an electric current proportional to the incoming photon flux, the SNR is the ratio between the mean power of the electrical signal and the mean power of the noise.

2.4.1 The types of noise

In spectroscopy, we usually distinguish between *additive noise* and *multiplicative noise*. The first one is the noise added to the signal; the latter varies with the signal power. In the introduction of this chapter we have mentioned the multiplex advantage of an interferometer over a dispersive spectrometer (Fellgett advantage). This advantage occurs only for additive noise.

In terms of electro-optical detection, the noise contribution will depend on the energy of the detected photons, in other words on the wavelength region under investigation. Table 2.2 shows the common subdivision of photons in the infrared regions and their corresponding energy. In the far infrared region, photon energies are smaller than k_BT at room temperature; on the contrary, in the near-infrared, photon energies are higher.

Table 2.2: Spectral ranges with the corresponding photon energies of near and middle infrared (NIR) and far infrared (FIR) (thermal energy k_BT = 26 meV at T= 300°K).

	NIR			FIR	
wavelength	700 nm	$\longrightarrow$	25 μm	$\longrightarrow$	1 mm
wavenumber	14300 cm^{-1}	$\longrightarrow$	400 cm^{-1}	$\longrightarrow$	10 cm^{-1}
frequency	$4.3 \cdot 10^{14}$ Hz	$\longrightarrow$	$1.2 \cdot 10^{13}$ Hz	$\longrightarrow$	$3 \cdot 10^{11}$ Hz
photon energy (hν)	1.78 eV	$\longrightarrow$	49.6 meV	$\longrightarrow$	1.24 meV

Additive noise

Thermal noise (or *Johnson noise*, *electronic noise*, *circuit noise*) arises from thermal fluctuations of the current in the detector and is independent of the signal level. As mentioned above, in the infrared region, photon energies are smaller than these thermal fluctuations and, therefore, detectors will mainly be limited by thermal noise.

In addition, we mention the *dark-current noise*, which is an additive noise as well. Photodetection devices also generate dark-current noise, which is present even in the

absence of light and results from random electron-hole pairs generated thermally or by tunneling [31, p. 674].

Multiplicative noise

Photon noise (or *quantum noise*, *shot noise*) is associated to the electromagnetic radiation itself and is a fundamental quantity. It refers to the fluctuations resulting from the random arrival of photons at the detector. The standard deviation of these fluctuations is proportional to the square root of the number of photons arriving. Therefore, the noise power is proportional to the square root of the signal power. Photon noise is a multiplicative noise. In the near-infrared and visible region, very sensitive detectors (e.g. photo-diodes) are available, which allow to approach photon-noise-limited detection. In this case, there is no multiplex advantage of the FTS over a dispersive instrument (note that the interferometer still enjoys the luminosity or étendue advantage).

Chapter 3

Considerations about miniature Fourier spectrometers

In the previous chapter, general aspects of Fourier transform spectroscopy have been considered. Now, we shall treat more specific facets regarding Fourier spectrometers, essentially when considering micro-sized devices. Two miniature Fourier spectrometers (a stationary and a seanning one) will be presented later. The topics discussed here are related to given particularities concerning configuration, or conception, associated with these instruments, as well as their potential performance.

3.1 Specifications

As will be mentioned in this section, one important application of miniature spectrometers is colorimetry. In the field of colour science, the specifications require a relatively low resolution in the visible wavelength range and a good intensity accuracy in the blue region. Despite the fact that the results of measurements are given by steps of 10 nm (in textile, paint or ink industry, the measured spectra are in general smooth), the wavelength accuracy is high, better than 0.5 nm. These requirements fit in general with the performance achievable by miniature spectrometers.

Investigating the potential and evaluating the performance of micro-sized Fourier spectrometers requires to select specific key parameters. Here, the straylight suppression ability, the colour recognition and the contrast are considered as quality indicators.

In our case the straylight suppression ability of the spectrometer, especially in the blue region, has been chosen as the most relevant indicator. The reason for that is associated with colour science. Firstly, the eye is particularly sensitive to spectral changes in the blue, which means that small variations in this wavelength region give a relatively large change in colour coordinates. Secondly, the commonly used type of spectrometer for this application is the grating spectrometer, which is particular sensitive to straylight. In reality, Fourier transform spectrometers (of any type) are not sensitive to physical straylight, believed as scattered parasitic light. The unique effect caused by physical straylight is a reduction of the contrast by a certain factor, but in principle the visibility curve is not altered. In our study, straylight is meant as a comparison parameter, and one should be

aware that what is called 'straylight' comes from the mathematical transformation of an undesired noisy contribution distributed in the spectrum. This is the fundamental reason why a mathematical treatment of the interferogram can reduce the spectral weight in a given suppressed region (see sections 3.2.2, 3.3.2, 4.1.2 and 4.1.1).

It is convenient to define the suppression spectrum $S(\lambda)$, which is a different representation of the transmission spectrum $T(\lambda)$. The suppression spectrum is expressed in dB and is calculated as

$$S(\lambda) = -10\log_{10}[T(\lambda)]. \tag{3.1}$$

The reference value SU used to quantify the straylight suppression ability is defined as

$$SU = \frac{1}{\lambda_2 - \lambda_1}\int_{\lambda_1}^{\lambda_2} S(\lambda)\mathrm{d}\lambda, \tag{3.2}$$

which is the mean value of $S(\lambda)$ between $\lambda_1 = 400$ nm and $\lambda_2 = 470$ nm, when a blue-blocking filter (GG495) is measured (see Appendix C). In section 4.1.1, measurements of SU, carried out with a spatially modulated interferometer, are used to practically evaluate the performance of the spectrometer.

An additional key feature used to evaluate the performance, is the colour separation ΔE introduced in section 3.1.1. ΔE is the ability of the spectrometer to measure the real colour of a sample.

Finally, the contrast C of the central fringe for a symmetrical (or non-dispersive) configuration can be considered as a good indicator for the reliability of the interferogram. The limit value for the contrast has been determined empirically from interferograms fulfilling the specifications concerning SU and ΔE. In other words, the contrast is here a quality factor that indicates whether the interferogram will give a spectrum which achieves the desired performance.

Micro-sized spectrometers should satisfy the following specifications:

- $\Delta\lambda = 10$ nm,
- wavelength range 380 nm $< \lambda <$ 730 nm,
- λ accuracy < 0.5 nm,
- $SU > 20$ dB,
- $\Delta E < 1$,
- $C > 50\%$.

3.1.1 Colorimetry

Colorimetry is the measurement of colours. One fundamental aspect related with micro-sized spectrometers (of any type or concept) is colour science, since they find most of their applications in this field.

In 1931, the 'Commission Internationale de l'Eclairage' (CIE) developed a standard method of determining colours, called CIE 1931, which is based on perceptual and physiological measurements. It represents an internationally agreed method of colour identification based on a linear combination of trichromatic stimuli [32]. Colours are represented in a so-called CIE diagram (or chromaticity diagram, see Fig. 3.1), which is based on the

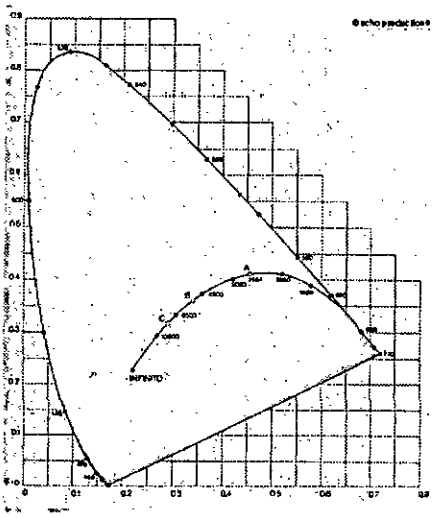

Figure 3.1: CIE 1931 Standard Colour Table, used to specify colours.

ability of the human eye to match colours. It is a mathematical construction that has the advantage that the position of each colour in relation to the primary colours can be calculated.

The values plotted in the CIE 1931 diagram are obtain from the measurement of the tristimuli values X, Y and Z obtained as follows:

$$\begin{aligned} X &= K\sum T(\lambda)r(\lambda) \\ Y &= K\sum T(\lambda)g(\lambda) \\ Z &= K\sum T(\lambda)b(\lambda) \\ \text{with } K &= 100/\sum g(\lambda), \end{aligned} \tag{3.3}$$

where $r(\lambda)$, $g(\lambda)$ and $b(\lambda)$ are the so called tristimuli functions determined by the CIE and $T(\lambda)$ is the transmission spectrum. In order to study colours using two dimensional maps, three new variables x, y and z (colour-masses) were derived from the three measured values of X, Y and Z by dividing each of these numbers by their total sum: $x = X/(X+Y+Z)$, $y = Y/(X+Y+Z)$ and $z = Z/(X+Y+Z)$. With this conversion, the sums of the colour-masses add up to one ($x+y+z=1$). Only two of the new values thus remain

independent, and these can be shown on a two-dimensional chart. In the CIE diagram shown in Fig. 3.1, the horizontal axis represents the values for x, and the vertical axis the values for y.

Colour separation

Unfortunately, the CIE Standard Colour Table cannot be used to determine colour differences as simple gradations on a chart. This drawback has always been the subject of criticism. Indeed, for the application of colour in industry, it is not only the measurement of colour that is significant, but also the exact determination of colour differences. Then, in 1976, a new system emerged, recommended by the CIE and named CIE $L^*a^*b^*$, which is now widely used for non-self-luminous objects such as textiles, paints and plastics. The CIE $L^*a^*b^*$ system is derived from the CIE Standard Colour Table by transforming the original X, Y and Z coordinates into the three new reference values of L^*, a^* and b^* [33]:

$$\begin{aligned} L^* &= 116\left(\frac{Y}{Y_0}\right)^{1/3} - 16 \\ a^* &= 500\left[\left(\frac{X}{X_0}\right)^{1/3} - \left(\frac{Y}{Y_0}\right)^{1/3}\right] \\ b^* &= 200\left[\left(\frac{Y}{Y_0}\right)^{1/3} - \left(\frac{Z}{Z_0}\right)^{1/3}\right]. \end{aligned} \tag{3.4}$$

with $X_0 = 98.072$, $Y_0 = 100$ and $Z_0 = 118.225$. If one of the ratios $\frac{X}{X_0}$, $\frac{Y}{Y_0}$ and $\frac{Z}{Z_0}$ is smaller than 0.008856, then the respective ratio changes to:

$$\begin{aligned} \frac{X}{X_0} &= 7.787\left(\frac{X}{X_0}\right)^{1/3} + 16/116 \\ \frac{Y}{Y_0} &= 7.787\left(\frac{Y}{Y_0}\right)^{1/3} + 16/116 \\ \frac{Z}{Z_0} &= 7.787\left(\frac{Z}{Z_0}\right)^{1/3} + 16/116. \end{aligned} \tag{3.5}$$

The separation between two colours is defined as

$$\Delta E = \sqrt{\Delta L^{*2} + \Delta a^{*2} + \Delta b^{*2}}. \tag{3.6}$$

When ΔE is smaller than 1, then the ability of the human eye to distinguish two adjacent colours vanishes.

3.1.2 Number of pixels and dynamic range

We have mentioned the sampling of an interferogram. At the output of a CCD line the signal is as well digitized and, as a consequence, the level of a suppression region varies as a function of the degree of digitalization η, expressed in bits. The total number of available grey levels is equal to 2^η. We shall see here that it is not recommended to oversample the interferogram.

The noise-free interferogram

$$F_n = \sum_m \cos[2\pi mn/N], \tag{3.7}$$

has been digitized. It is composed by a given set of frequencies m ($m < N/2$), being integers (to avoid sidelobes). Of course, the finer the digitization, the lower the mean level of the suppressed frequencies ρ. It is shown that ρ is linear with η above a certain digitization level. Indeed, when compared with one grey level, which is equal to $1/2^\eta$, the ratio $\Xi(\eta) = \rho/(1/2^\eta)$ (see Fig. 3.2) saturates after having reached a certain degree of

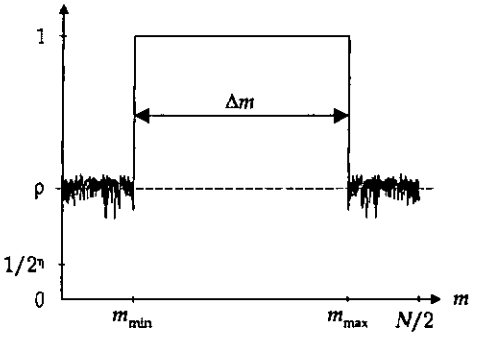

Figure 3.2: Square spectrum retrieved from the digitized interferogram from Eq. (3.7). ρ is the mean level of the suppressed frequencies and $1/2^\eta$ corresponds to one grey level. The spectrum is composed of integer frequencies m extending from $m_{\min}$ to $m_{\max}$.

digitization η.

The ratio Ξ (after saturation) is plotted in Fig. 3.3 as a function of the number N of sampling points. As can be seen, Ξ is proportional to the square root of N. This means that, for a given digitization, the higher the sampling rate, the higher the mean level of suppressed frequencies. As a consequence, oversampling the interferogram is not recommended.

The ratio Ξ in Fig. 3.3 depends on the bandwidth of the spectrum. Table 3.1 shows

Table 3.1: Square root law followed by the ratio Ξ in function of the bandwidth Δm.

Δm	
$0.8N/2$	$0.232\sqrt{N}$
$0.6N/2$	$0.179\sqrt{N}$
$0.4N/2$	$0.122\sqrt{N}$
$0.2N/2$	$0.061\sqrt{N}$

the factors multiplying the square root of Ξ. It is shown that the larger the bandwidth, the greater the effect of an oversampling.

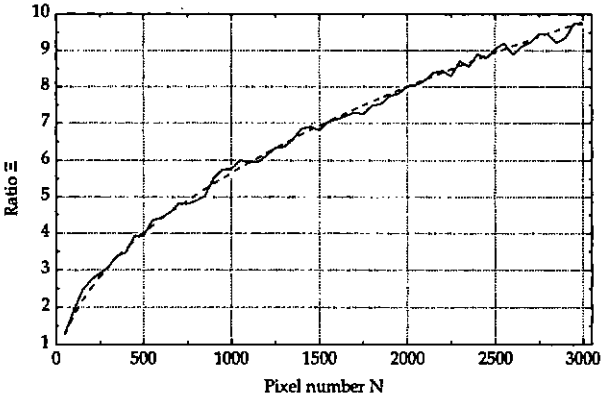

Figure 3.3: Ratio $\Xi = \rho/(1/2^n)$ as a function of the number of sampling points N (plain line). Here, the dashed line is $0.179\sqrt{N}$.

3.2 Performance of a stationary Fourier spectrometer

In the case of a stationary Fourier spectrometer, as presented in chapter 4, the device parameters that affect the specifications given in section 3.1 are:

- the number of sampling points N,
- the dynamic range η of the detector,
- the area of the pixel and its pitch,
- the background intensity distribution and nonuniformity,
- the tilts of the mirror α_x and α_y,
- the maximum optical path difference δ_{max},
- the cutoff wavelength λ_{min},
- the lateral extension h of the source,
- the focal length of the collimating lens,
- the distance z from the interference plane to the detector,
- the distortion,
- the dispersion,

- the noise.

In Fig. 3.4, these parameters are illustrated.

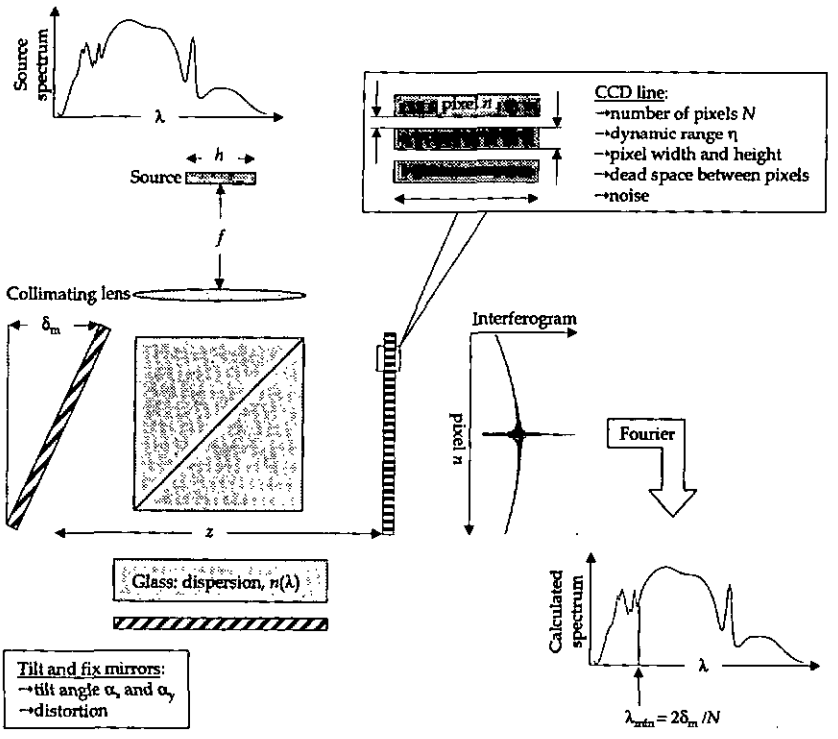

Figure 3.4: Illustration of the parameters affecting the performance of a stationary Fourier spectrometer.

It is the aim of this section to assess the device parameters necessary to achieve the specifications. This evaluation has been carried out by simulating specific interferograms, in which the device parameters are taken into account.

Additional features will be discussed in section 3.4 concerning the influence of the extension of the light source.

3.2.1 Resolution and dynamic range

We know that, according to Eq. (2.58), the theoretical resolution for a two-sided interferogram is equal to $\delta\lambda = 2\lambda^2/N\lambda_{\min}$. It follows that the amount of sampling points

necessary to achieve an experimental resolution $\Delta\lambda$, defined as the full half width maximum (FWHM) of a peak, must be superior to

$$N = 2\lambda^2/\lambda_{\min}\delta\lambda, \tag{3.8}$$

where $\lambda_{\min}$ is the cutoff wavelength. A theoretical resolution of 10 nm at $\lambda = 730$ nm, requires 280 sampling points for $\lambda_{\min} = 380$ nm (a similar numerical example is given in section 2.2.4).

In order to determine the amount of sampling points N and dynamic range η necessary to achieve a given experimental resolution $\Delta\lambda$, two-sided interferograms of monochromatic radiations have been simulated, with the following device parameters:

- the dynamic range is $\eta = 16$ bit,
- the pixel width is $s = 20$ μm,
- the pixel period is $b = 25$ μm,
- the background intensity is Lambertian,
- the tilts of the mirror are $\alpha_x = 3.5$ mrad and $\alpha_y = 0$,
- the cutoff wavelength is $\lambda_{\min} = 350$ nm,
- the lateral extension of the source is $h = 400$ μm,
- the focal of the collimating lens is $l = 80$ mm,
- the distance from the interference plane to the detector is $z = 4$ mm,
- the standard deviation of the noise is proportional to the signal and is equal to 5 bit.

The result of the simulated experimental resolution in terms of FWHM is shown in Fig. 3.5.

It can be seen that the simulated experimental resolution has a λ^2 dependence as expected theoretically (Eq. 3.8). In addition, it turns out that, with these selected device parameters, the experimental resolution will be decreased by a factor about 1.7 compared with the theoretical resolution. From table 2.1, one remembers that in case of truncation, the resolution is reduced by a factor 1.2.

Experimental measurements will be shown in section 4.3.1.

As expected, Fig. 3.5 reveals that for shorter wavelengths, the resolving power is higher. This will be exploited in section 3.3.2 to enhance the straylight suppression ability SU.

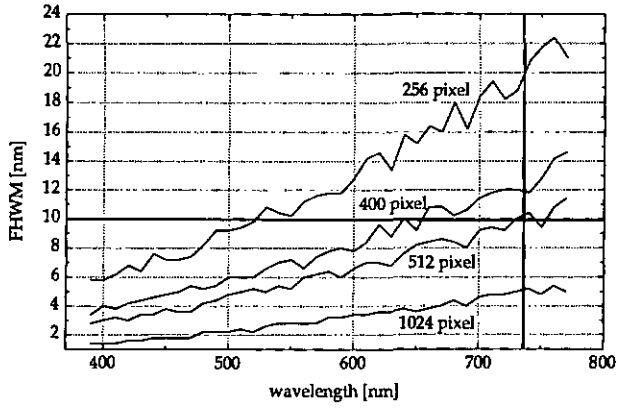

Figure 3.5: Simulated experimental resolution in term of full width at half maximum (FWHM) as a function of the wavelengtb, for different numbers of pixels. No apodization was used.

3.2.2 Equalization of the interferogram

A particularity of stationary Fourier spectrometers is the nonuniform distribution of the background intensity, caused by the fact that the interference is spread in space. We distinguish between the slowly varying distribution generated by the light source, which is never spatially uniform, and the local contributions caused by inhomogeneities of the optical components or the detector array.

In section 4.1.2, the influence of inhomogeneities will be discussed and experimental methods to remove them will be proposed. Here, we treat the subtraction of the smooth variations of the background intensity (we simply call it *background* in the following discussion) from the mathematical point of view.

The background nonuniformity has two consequences:

- It brings a high spectral weight to the very low frequencies; if the background is a constant offset, only a zero frequency component is added to the spectrum.
- It adds strong modulations overall the spectrum.

The stronger effect is caused by the fact that the first point of the interferogram is not at the same level as the last one. In addition to spectral undulations, this adds a baseline contribution. Figure 3.6 shows a schematic interferogram on a certain background. The corresponding spectrum shows typical wavy contributions and a raised baseline. In this classical case, removing the mean value of the interferogram does not help.

The frequency of the parasite ripples is equal to half the inverse of the pixel number, $1/2N$. Their amplitude is about equal to the difference ΔI between the beginning and the end of the interferogram (see Fig. 3.6). The baseline of the spectrum raises by about

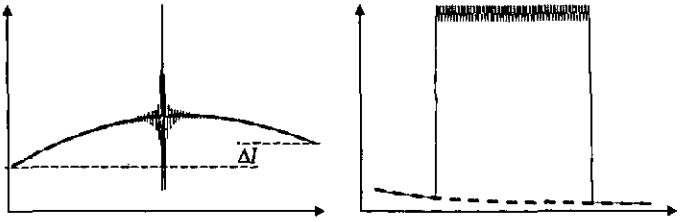

Figure 3.6: Left: Interferogram (plain line) and background (dashed line). Right: Resulting spectrum (plain line) and baseline (dashed line).

the same magnitude. It can be observed that a small difference ΔI of 2% compared with the mean value of the interferogram, gives a ripples amplitude of 1.5% and a baseline raising of 2% (17 dB) compared with the intensity of a white spectrum.

In reality, the light source is emitting with a Lambertian distribution, which gives rise to high nonuniformity of the background, particularly when the majority of the light emitted by the source is collected. Then, an apodizing effect appears, which deteriorates the resolution. As a result, the averaging, or equalization procedure has to include a local stretching of the interferogram.

Equalization procedure

In order to obtain the offset-free interferogram F_n without background, the signal I_n recorded at the sampling positions n is equalized and stretched as follows:

$$F_n = \frac{I_n}{J_n} - 1, \tag{3.9}$$

where

$$J_n = \frac{1}{L} \sum_{k \in L} I_k \tag{3.10}$$

is the mean value (over L points) of the detected signal. The longer the number of sampling L considered for averaging, the smoother the equalization. A typical value for a 512 pixel interferogram is $L = 50$.

As seen above, a small difference ΔI between the two ends of the interferogram causes a dramatic effect on the spectrum. In practice, a background removal as described in section 4.1.2 does not let a perfectly leveled interferogram. Therefore, we operate an equalization of the interferogram, as well as of the measured background.

Figure 4.9 shows an equalized interferogram with the measured background being removed.

3.2.3 Response of a photodiode array

An additional aspect, typical for compact Fourier spectrometers based on a stationary configuration, follows from the fact that a photodiode array (PDA) is used. In the case

of the spectrometer as described in chapter 4, the detector is a CCD line composed of N pixel having a width s of 20 μm and a height of 500 μm. Neigbbour pixels are separated by a 5 μm *dead zone*, so that the period b becomes of 25 μm.

The width s of the pixel area in the x-direction determines the calculated intensity response of the spectral components. This feature is illustrated in Fig. 3.7. In practice,

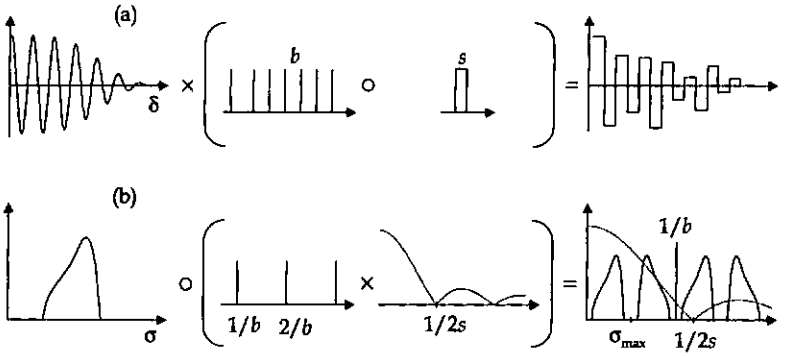

Figure 3.7: Representation of the effect induced by a detector with a period b and a pixel width s ($s \leq b$).

the recorded interferogram is the true interferogram multiplied by a Dirac comb, which is convoluted by a rectangular function of width s (Fig. 3.7(a)). In the Fourier space (Fig. 3.7(b)), this leads to a convolution of the spectrum with the multiplication of a Dirac comb and a sinc function having the first zero at $1/2s$: $\mathrm{sinc}(1/2s, \sigma)$. This sinc function changes the spectral response of the spectrometer.

If the width s is equal to the sampling interval b, then the spectral response is zero for the wavenumber σ_{max} corresponding to the cutoff frequency. This is an evident result, since, at σ_{max}, the contrast would be zero. In our particular case, the ratio between the active area and the sampling interval is 80%, which gives a zero response at $1.25 \times \sigma_{max}$. In this configuration, the power of the cutoff frequency is reduced by 24%.

Pixel height

Due to the particular shape of the pixels described above, a stationary interferometer is very sensitive to the tilt of the fringes shown in Fig. 3.8. This inclination is caused by the tilt α_y of the mirror perpendicular to the tilt α_x which is used to generate the interferogram (see Fig. 3.8).

For a spectrum corresponding to a standard red test plate used for colour calibration and a cutoff $\lambda_{min} = 350$ nm, it has been shown that an unwanted mirror tilt of $\alpha_y = 0.5$ mrad (i.e. a fringes inclination of 6°) leads to a decrease of the contrast from 86% to 51%, giving rise to a colour change of $\Delta E = 0.3$.

The effect due to the extension of the pixel is of course larger when the detected modulation has a short spatial variation. Then, since the resolution of spatially modulated

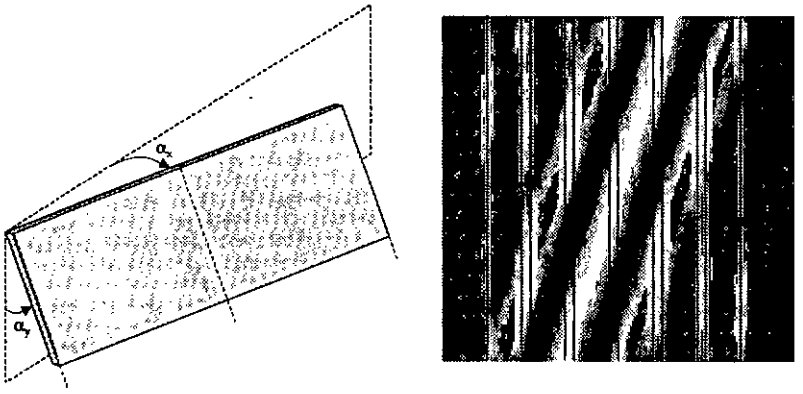

Figure 3.8: Inclined interference pattern. Some pixel are represented; the ratio between the pixel height and the pixel period is equal to 20.

interferometers is depending on the amount of pixel number, attention has to be paid to the position accuracy of the tilt mirror; the more vertical the fringes, the closer the minimum desired accessible wavelength to the cut off. In case of spectroscopy in the visible with a desired wavelength range from 380 nm to 730 nm, we suggest a cutoff at $\lambda_{min} = 350$ nm.

3.3 Noise analysis and reduction of noise

In section 2.4, the different types of noise encountered in Fourier spectroscopy have been presented. One additional contribution, the fixed pattern noise (or background intensity distribution), will be discussed in section 4.1.1 and section 4.1.2. In both cases, i.e. statistical noise or fixed pattern noise, apodization helps to reduce the effect caused by poor signal-to-noise ratio near the borders of broad band interferograms. The aim of this section is to study the signal-to-noise ratio (SNR) in the spectrum, particularly for broadband spectra. In addition, a method is proposed to reduce the effect of noise in broadband spectra by using variable apodization.

Overview

The detailed treatment of the relationship between the noise in the interferogram and the resulting signal-to-noise ratio in the calculated spectrum is a complex study. According to Chamberlain [7, p. 283], "it can take you into some of the more esoteric branches of the subject." Janine Connes [1] has given a complete treatment of the problematic of noise. Since then, noise levels in FTS have been considered by several studies, either by discussing random sampling errors for a monochromatic spectral line [34] and more general spectra [35, 22], or by estimating signal-to-noise ratios in the computed spectrum from

observation of the noise in the interferogram [36], or comparing the SNR obtained with Fourier spectrometer and dispersive scanning devices [37], or analyzing effect of sampling jitter induced by frequency fluctuations of the refereoce laser, as well as caused by detector and electronic noise [38]. Note that the study of systematic sampling errors [24] refers rather to the problem of phase distortion.

More recently, a derivation of the SNR from basic principles in optical interferometric cross correlators based on broadband light sources has been carried out [39]. Interferometric cross correlators are used to detect the amplitude and phase of optical signals in interferometric mieroscopy [40] or dispersive spectroscopy [41, 42]. This technique differs from FTS, in which the focus is on *autocorrelation*, in emphasizing phase-sensitive detection and *cross-correlation*.

Comparison between SNR of dispersive and Fourier spectrometers has been a driving force in the study of noise. This has lead to the well-known multiplex advantage pointed out by Fellgett, which is valid even in the presence of high background noise [43]. Since this bene6t does not apply for multiplicative noise, e.g. shot noise, the unanimous opinion is that FTS offers, in UV-Visible spectroscopy, no significant advantages in SNR over dispersive techniques, except for line emission spectra [44]. We mention that reference [45] describes a UV-Visible stationary FT spectrometer, which is not limited by shot noise and so the Fellgett advantage applies. The question of the applicability of the Fellgett advantage in a standard Michelson interferometer optimized for the UV-Visible region has been described by the authors of reference [46]. They reported that the noise in the spectrum was localized on the peaks rather than distributed equally throughout the spectrum and they found that the presence of large peaks had no effect on smaller signals. Nevertheless, the experimental verification of the applicability of the Fellgett advantage has not been as unequivocal. SNR characteristies of a hybrid dispersive interferometer has been discussed in reference [47] and the conclusion was that the presence of large peaks degraded the SNR of smaller peaks. In addition, it is shown that flicker noise ($1/f$-noise) remains localized where the spectral weight is, contrary to shot noise, which is uniformly distributed throughout the baseline of the spectrum [48].

Finally, note that for stationary Fourier spectrometers, using a linear photodiode array, the quantization noise can limit the SNR, particularly when the contrast is low [49, 50]. In addition, when the interferogram is spread in space rather than in time, the size of the source has an important influence on the visibility of the interference pattern. Reference [51] discusses the optimization of the SNR for a stationary Fourier spectrometer.

3.3.1 Treatment of the noise problem in the spectrum

The main aspect that limits such an analysis is the shape of the spectrum (or the interferogram). This is the reason why people give normally qualitative treatments. Generally, one separates the problem between monochromatic radiation, broadband spectra without sharp features and broadband spectra containing absorption lines. Here we focus on broadband spectra without sharp features, since they represent the spectra of interest when considering the main application of micro-sized spectrometers. Note that absorption spectra consisting of broadband spectra with sharp absorption lines, require a high dynamic range. Indeed, their corresponding interferograms consist mainly of low contrast

modulations extending as far as the length of coherence of the sharpest feature. This limitation can be suppressed by the technique of double beam differencing [52].

In this section, we try to find the influence of the shape of the interferogram (i.e. its envelop) and the SNR in the spectrum. We shall show that this influence can be quantified with a unique value, the coherence length, which is defined as the area under the envelope (Eq. (2.25)).

In this section, a Gaussian spectrum with variable width has been used, since it well represents the types of spectra considered in Fourier spectroscopy with micro-sized devices. In addition, it has the advantage that the relation between the envelop of the interferogram and the shape of the spectrum are known.

Statiatical noise analysis

The noise analysis has been carried out by generating digital white noise, which has been added to a sampled and digitized interferogram

$$I_n = 0.5 \exp[-\pi n^2/w_I^2] \cos[2\pi m_0 n/N] + 0.5, \tag{3.11}$$

consisting of a cosine modulation having a Gaussian envelop, where n are the sampling positions ($-N/2 < n < N/2 - 1$), w_I the FWHM of the Gaussian envelop and m_0 is a probe frequency, which will be used for the calculation of the SNR. The corresponding spectrum

$$\begin{aligned} B_m &\propto \sum_{n=-N/2}^{N/2-1} I_n \exp[2\pi m n/N] \\ &\propto \exp[-\pi(m - m_0)^2/w_B^2] \end{aligned} \tag{3.12}$$

has a Gaussian shape, where

$$w_B = \frac{N}{w_I}, \tag{3.13}$$

is the FWHM of the Gaussian spectrum.

The noise is characterized by the standard deviation. The intensity I_0 of the interferogram at zero path difference (ZPD) is 1. As will be shown below, the noise power I_{RMS}^2 in the interferogram is proportional to the spectral noise B_{RMS}^2, which is evident since the Fourier transform is a linear transformation. Then, the SNR at the ZPD will give an estimation of the SNR in the spectrum without computing the transform.

The work of Connes [1] indicates that the noise in the spectrum is at a minimum when the interferogram is recorded continuously through an RC filter, and a Fourier transform of the filtered interferogram is made. When the same interferogram is sampled and a digital Fourier transform is computed, the same result is achieved with a step-record method. If h is the step interval in the time domain, the variance of the spectral noise power is given [36], without apodization, by

$$B_{RMS}^2 = 2ThI_{RMS}^2, \tag{3.14}$$

where T is the total recording time. This is true when h is larger than the integration time τ given by the RC filter ($\tau = RC$).

Now, if the delay in the interferometer is measured in terms of optical path difference increments b, the variance for a one-sided unapodized interferogram of N points becomes [53]

$$B_{\mathrm{RMS}}^2 = 2Nb^2 I_{\mathrm{RMS}}^2. \tag{3.15}$$

An analogous result is given by reference [54] for two-sided interferograms.

Estimation of the SNR

A bandpass spectrum of total width $\Delta\sigma$ can be divided into M spectral elements. From Eq. (2.52), the number of spectral elements can be rewritten as $M = \Delta\sigma N/\sigma_{\max}$. Following reference [36], the intensity at ZPD can be estimated as

$$I_0 = B_{\max}\Delta\sigma/2\sigma_{\max}, \tag{3.16}$$

where $B_{\max}$ is the maximum intensity of the bandpass spectrum. Calculating the quantity $B_{\max}b/B_{\mathrm{RMS}}$ gives

$$\mathrm{SNR}_B = \mathrm{SNR}_I\sqrt{\frac{\sigma_{\max}}{\delta_{\max}\Delta\sigma^2}} = \mathrm{SNR}_I\frac{\sqrt{2}}{b\sqrt{N}\Delta\sigma}, \tag{3.17}$$

where $\delta_{\max} = bN$.

The first remark resulting from Eq. (3.15) is evident, since the Fourier transform is a linear operation: if all interferogram parameters (i.e. number of sampling points and cutoff frequency) are fixed, then the noise power in the spectrum is proportional to the noise power in the interferogram. In addition, if the RMS value of the interferogram is fixed, then the RMS value of the noise in the spectrum is proportional to the square root of the number of sampling points N and proportional to the cutoff wavelength $\lambda_{\min} = b/2$.

An additional parameter $\Delta\sigma$, characteristic of the spectrum, is taken into account in Eq. (3.17). Again, if the interferogram parameters are fixed, we observe that the SNR_B in the spectrum is proportional to the SNR_I in the interferogram. On the other hand, for a given spectrum, when the noise in the interferogram is fixed, the SNR_B is inverse proportional to the square root of the number of sampling points and inverse proportional to the cutoff wavelength.

As mentioned previously, in the study of the signal-to-noise ratio, the relevant notion is the shape of the spectrum. We consider now two cases:

1. oversampling of the interferogram, and
2. observing the interferogram at longer path lengths.

Oversampling

In a stationary configuration, oversampling the interferogram is equivalent to decreasing the tilt of the mirror. To treat this configuration, we use the fact that the width of the spectrum is $\Delta\sigma = M\delta\sigma = M/2\delta_{\max}$, and we assume that the number of detectable spectral elements M is fixed. In the extreme case of no tilt, all pixels detect ZPD only. In this case, the width of the spectrum would be 'infinite', since the path difference is zero,

but the detector pixels record the total energy contained in the spectrum. Equation (3.17) becomes $\mathrm{SNR}_B = \mathrm{SNR}_I 2\sqrt{2N/M}$.

Then, for constant number of samples N and number of spectral elements M, the SNR_B in the spectrum is constant. This has been observed by adding digitally generated white noise to several interferograms having a different cutoff wavelength λ_{min}. The experience has been undertaken with additive and multiplicative noise; the fact that SNR_B is constant has been observed in both cases.

In conclusion, when the number of sampling points is fixed by the device configuration, it is preferable to choose a cutoff wavelength as close as possible to the minimum observed wavelength.

Larger path differences

Observing the interferogram at larger optical path differences δ_{max} with constant optical difference increment b, is equivalent to adding additional sampling points. In this case, the longer the path the better the spectrum is resolved, but the width of the spectrum $\Delta\sigma$ remains the same. Equation (3.17) becomes $\mathrm{SNR}_B = \mathrm{SNR}_I\sqrt{2}/b\Delta\sigma\sqrt{N}$. Thus, we obtain that the SNR_B in the spectrum is inversely proportional to the square root of the number of sampling points. This means that a higher number of sampling points yields a lower SNR_B. This result is understandable, since a broad band spectrum gives rise to an interferogram having an important contribution near ZPD, decreasing very rapidly with increasing optical path difference. Thus, observing the interferogram at larger path differences, i.e. where no substantial information is available, will add more noise power than signal power.

Note that the SNR of monochromatic radiation has an opposite behaviour. A monochromatic line will generate an interferogram, which is a cosine modulation. When this modulation is Fourier transformed in the spectral domain, it will give a narrow line intensity distribution, which is directly proportional to the maximum optical path difference (or the number of sampling points N). On the other hand, the RMS value of the noise in the spectrum increases with the square root of N (Eq. (3.15)). Thus, the SNR in the spectrum will increase proportionally with N.

By studying this case with Gaussian spectral line shapes, we observe that the behaviour of the SNR_B as a function of N is not strictly dictated by Eq. (3.17). For a number of sampling points N (larger than N_0), the SNR_B behaves like expected, but for N below N_0 we observe that the SNR_B is decreasing. Figure 3.9 shows this behaviour, which has been pointed out, but not quantified, by Chamberlain [7, p. 285]. From Fig. 3.9, we notice that the maximum of the curve is at N_0, which corresponds about to the width of the Gaussian envelope in the pixel domain ($N_0 \approx w_1$), in this case 256 pixels. A closer observation shows that the maximum signal-to-noise ratio is achieved when the contrast in the interferogram is about 40%. The same experiment has been carried out with different coherence lengths and it turned out that the maximum SNR_B occurs always when the contrast is about 40%.

The position N_0, at which the maximum SNR_B occurs, depends only on the coherence length defined here as $l_c = bw_1$. N_0 is independent of the noise level I_{RMS} in the interferogram, as well as of the dynamic range (except if one uses less than 9 bit or 512 grey

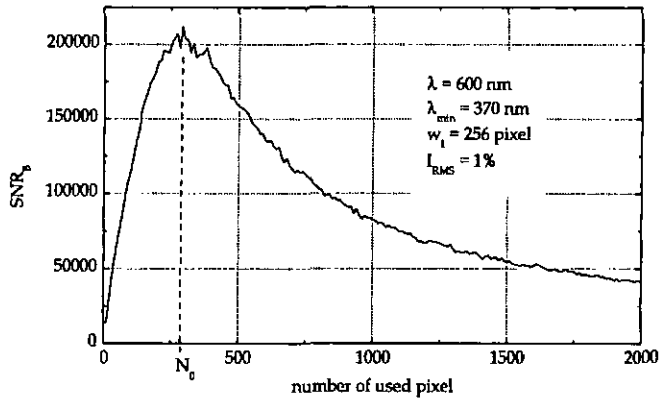

Figure 3.9: Signal-to-noise ratio in the power spectrum of a Gaussian line shape. The envelop of the interferogram has a width w_1 given in numbers of samples. The relation with the coherence length is $l_c = bw_1$.

level).

The linear relation between the coherence length and the maximum signal-to-noise ratio in the spectrum (at the position N_0) is shown in Fig. 3.10. This result is in accordance with Eq. (3.17), because the width of the band $\Delta\sigma$ can be estimated as the inverse of the coherence length.

Of course, the position N_0 would be the ideal position (in term of SNR_B) for truncating an interferogram for a given coherence length l_c. In reality, due to the poor resolution available after such a truncation, one has to choose a trade off between loss of SNR_B and desired resolution. A similar trade off between the amplitude of the sidelobes due to the truncation and the SNR_B for a Lorentzian spectral line shape was studied in reference [53]. The practical application in reference [53] was to find of the best signal-to-noise ratio for absorption spectra.

The previous results change if apodization is applied. In the quest of the best achievable SNR_B, apodization can be used to reduce the sidelobes [55] and enhance the SNR_B, taking into account that the resolution is deteriorated. In Eq. (3.14), apodization is taken into account by a factor Q, which is the mean value of the square of the weighting function (Q is equal to unity for no weighting): $B^2_{\mathrm{RMS}} = Q2ThI^2_{\mathrm{RMS}}$. For a triangular apodization, this factor is 0.31. This makes the signal-to-noise ratio about three times better, but the resolution 1.47 times lower.

Analytical treatment

As mentioned before, the previous study has been carried by adding digitally generated white noise to a known interferogram (a cosine modulation damped by a Gaussian envelop). As the relation between this interferogram and its corresponding power spectrum

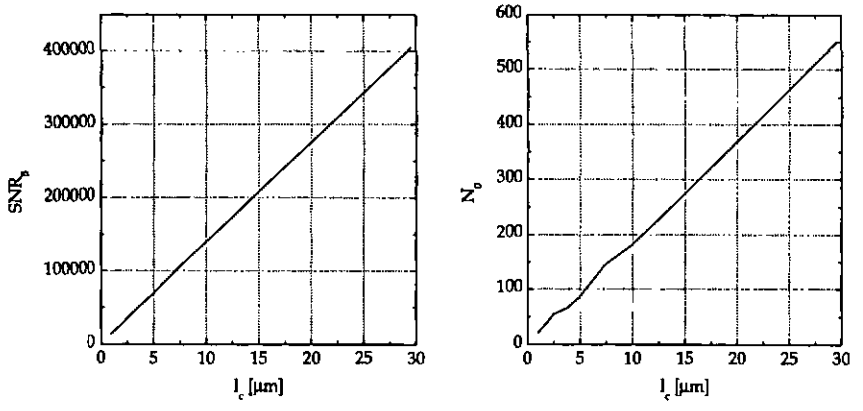

Figure 3.10: Left: Signal-to-noise ratio in the spectrum as a function of the coherence length. Right: Position N_0, at which the maximum SNR_B occurs.

is well-known, it is possible to find an analytical expression for the signal-to-noise ratio in the spectrum. The shape of the interferogram and of the spectrum are characterized by one essential parameter, the coherence length l_c.

From Eqs. (3.12) and (3.13), the Fourier transformed interferogram becomes

$$B_m \propto \exp[-\pi(\mathrm{m} - m_0)^2 l_c^2/N^2]. \tag{3.18}$$

Taking the noise power as given in Eq. (3.15), we obtain

$$\mathrm{SNR}_B = \mathrm{const}\frac{\exp[-\pi(m - m_0)^2 l_c^2/N^2]}{2Nb^2 I_{\mathrm{RMS}}^2}, \tag{3.19}$$

for a given RMS value of the interferogram, where the constant factor depends on the coherence length and the cutoff wavelength. Three curves of the SNR_B of a Gaussian spectral line shape are shown in Fig. 3.11 for three different coherence lengths.

3.3.2 Improving straylight suppression

The previous section has shown that apodization reduces the signal-to-noise ratio in the spectrum by a factor Q. In section 3.2.1, we have seen that a broad band spectrum is better resolved at shorter wavelengths. Indeed, the theoretical resolution increases with the square of the wavelength, i.e $\delta\lambda(\lambda) = 0.5\lambda^2/\delta_{\mathrm{max}}$, where δ_{max} is fixed.

The Fourier spectroscopist usually gives the power spectral density as a function of the wavenumber. Nevertheless, by analogy with dispersive methods, it is convenient to show spectra as a function of the wavelength. This means that, once δ_{max} and N have been set to achieve a certain resolution at λ_{max}, all shorter wavelengths are better resolved. For instance, taking again the numerical example given in section 2.2.4, having fixed the

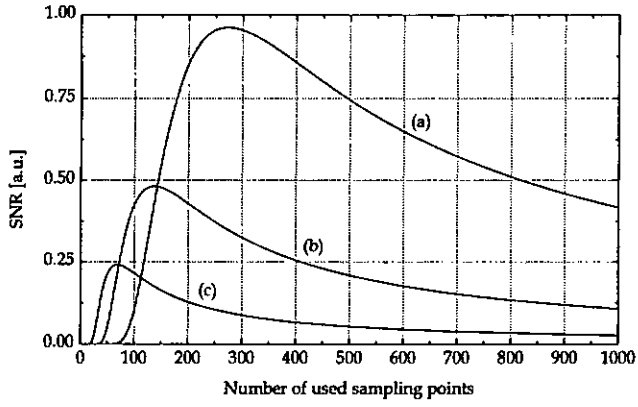

Figure 3.11: SNR_B of a Fourier transformed interferogram consisting of a cosine modulation with a Gaussian envelope. Curves (a), (b) and (c) correspond to three different coherence lengths: $l_c^{(a)} > l_c^{(b)} > l_c^{(c)}$. In this example, $m - m_0$ is 0.25.

parameters for a theoretical resolution of 10 nm at $\lambda = 730$ nm, one gets a theoretical resolution of 2.7 nm at $\lambda = 380$ nm.

For applications in the visible which require a good reduction of the noise in the blue region, it is possible to apply stronger weighting functions at shorter wavelengths and, consequently, improve the straylight suppression in this region.

Fourier transforming a truncated interferogram at selected positions depending on the wavelength allows to get a constant resolution $\delta\lambda$. Essentially, if one records the same amount of modulations $K_\lambda = \delta_{max}/\lambda$ for each wavelength separately, one obtains the same resolution for every wavelength in terms of resolving power. This is equivalent to Fourier transforming the interferogram with different apodization at each frequency. If the desired resolution $\delta\lambda$ is fixed, the necessary path length to record a given frequency is

$$D(\lambda) = w_A \lambda^2 / \delta\lambda, \tag{3.20}$$

where w_A is the apodization factor, such as FWHM $= w_A/\delta_{max}$ (see Table 2.1, e.g. $w_A = 0.603$ for a rectangle and $w_A = 0.886$ for a triangular apodization).

To achieve a constant resolution in the wavelength domain, the Fourier transform is calculated with a varying strength D_λ of the apodization:

$$B(\lambda) = \frac{1}{\lambda^2} \int_{-\infty}^{\infty} A(D_\lambda, \delta) F(\delta) \exp[i2\pi\delta/\lambda] \mathrm{d}\delta, \tag{3.21}$$

where $A(D_\lambda, \delta)$ is zero outside the interval D_λ. The normalization of the integral has been discussed in section 2.2.1.

With this procedure, we get a stronger apodization for shorter wavelengths. Apodization will be practically studied in chapter 4, mainly to reduce the effect of fixed pattern noise in spatially modulated interferometers.

3.4 Effect of the source extension

In section 2.3.3, the effect of a circular source in a scanning Michelson interferometer has been discussed. It was seen that the size of the source and the visibility are closely related.

In commonly used Fourier transform spectrometers, high resolution is a requirement. This is the reason why the studies are concerned with the effect of very long driving distances of the mirror, for instance, distortions due to off-focus [56], or misalignment of the movable mirror [57].

We consider now the aperture in micro-sized Fourier spectrometers. The problem is treated for a stationary Michelson interferometer.

The motivation for such investigations is the ability for a system to collect spectral power. Figure B.1 illustrates the notion of *étendue* (or *throughput*), which quantifies this capability. In order to facilitate the understanding, the scheme in Fig. B.1 shows a collimator (entrance of the system) and a condensor (exit of the system). In addition the source and the collector are circular. In reality, the source and the collector can have any shape and the relevant element remains the solid angle generated between the source and the detector, or vice-versa (see Fig. 3.12).

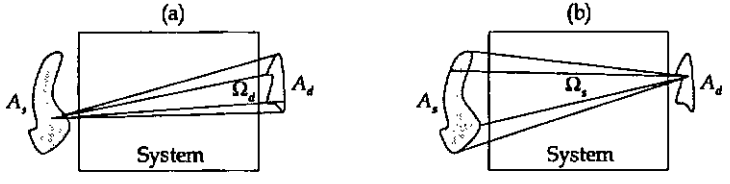

Figure 3.12: The angular acceptance of a system is either defined by the solid angle $Omega_d$ subtended by the detector (a), or vice-versa, $Omega_s$ by the source (b).

In other words, the crucial point is the angle of the bundle of rays passing through the system. Such a study consists then in summing the effect of all angles. Of course, as shown in Fig. B.1, additional optical elements (collimator and/or condensor) can be added in order to optimize the gathering of the light without altering the performance of the system.

The maximum acceptance solid angle Ω can be either calculated or measured. For some systems it can be determined analytically (section 2.3.3). In the case of an amplitude splitting interferometer, Ω can be measured by focusing a monochromatic radiation onto the interference plane and observing the interference pattern. The maximum acceptance angle is the angle subtended by the focus spot and the first minimum in the interference pattern. For a spatially invariant system (e.g. time scanning interferometer), this measurement can be carried out at one location (see Figs. 5.5 and 5.6). When the acceptance angle varies as a function of the position in the system (e.g. stationary configuration), the measurement has to be carried out over the entire system [58].

3.4.1 Spatial coherence

Dealing with an extended emitting surface instead of a point source brings us into the field of *spatial coherence*. Indeed, the fact that interference occurs even when the source is composed by laterally separated point sources, apparently not phase correlated, is a sign of coherence. Usually, one is not interested in what happens at the source itself, but rather how the source is perceived at a certain distance through a system capable to measure the coherence (i.e. an interference generator). In other words, if the optical elements through which the light passes are unable to resolve the individual radiating elements in the source, the source must be considered as incoherent.

The quality of the fringes produced by an interferometric system can be described quantitatively by the contrast C (or the visibility).

Young's experiment

Young's experiment is the easiest way to measure the degree of spatial coherence between two separate point sources. Remember that the Michelson interferometer has been used in the previous chapter to quantify the temporal coherence. In Young's experiment two pinholes separated by a distance a are placed at a distance l from a source of size h (see Fig. 3.13). The two apertures serve as sources of secondary wavelets.

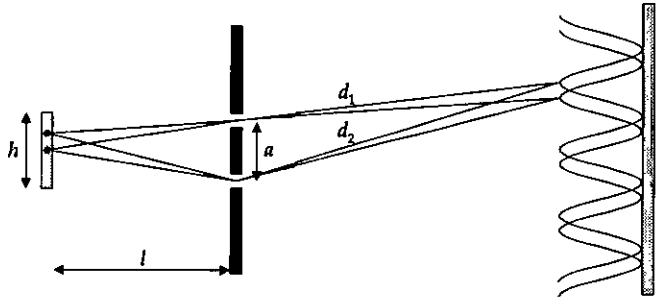

Figure 3.13: Young's experiment with an extended source. Two laterally separated point sources give rise to two fringe patterns. The modulation arises from the path difference $\delta = d_2 - d_1$. The different patterns issued from these point sources add up incoherently.

If the source is a point source, both pinholes will emit wavefronts, which are perfectly phase correlated. More precisely, using the same formalism as in section 2.1.1, the modulation of the intensity behind the pinholes (in the far-field) is described by the interference term $2\mathrm{Re}\{u_1 u_2^*\}$, where $u(t)$ is the optical disturbance at the single point source. By analogy with temporal coherence, the intensity modulation at the observation plane is governed by the interference term $2\mathrm{Re}\{u(d_1)u(d_1+\delta)^*\}$, where $\delta = d_2 - d_1$ is the path difference in Fig. 3.13. Considering the paraxial approximation, the intensity modulation is a cosine function.

The contrast is maximum when the two sources, u_1 and u_2, are correlated. The contrast is zero when the two sources are uncorrelated, for instance, if they are illuminated by two separate point sources having no phase relation. Nevertheless, these two cases do not fully describe the question of spatial coherence. Indeed, fringes can still be visible when the two points are illuminated by an extended source. In reality, one is concerned with the perception of the source by the pinholes, independently of how the source is described. For instance, if they are close together, they will give rise to fringes even if the source is large. On the other hand, if the pinholes are widely separated and the source is far away from the screen, it is perceived as a sufficiently small source to give rise to fringes again.

Note that in this experiment, the pinholes are considered sufficiently small if the following condition $\varnothing_{\text{pinhole}} \ll \lambda l/h$ [12, p. 174] for the diameter is fulfilled.

In Young's experiment, as described in Fig. 3.13, the contrast C is [59, p. 522]

$$C = \left|\text{sinc}\left(\frac{a\pi h}{l\lambda}\right)\right|. \tag{3.22}$$

Since the spatial frequency of the fringes is higher for distant pinholes, the contrast decreases when a increases. A similar remark can be made for the wavelength: the smaller the wavelength, the higher the frequency of the fringes. If the source is placed at a large distance l, or has a small extension h, then the contrast is higher. An additional interesting effect arises when the sinc function in Eq. (3.22) is negative. In this case, the fringes are shifted by half a period.

The Van Cittert-Zernike theorem

The discussion can be carried on in a more formal fashion, but this is not the purpose of this section. Nevertheless, one can hardly avoid to mention the Van Cittert-Zernike theorem, which is one of the most important theorems of modern optics. The interested reader is referred to the books of Hecht [59] (section 12.3) and Goodman [12] (section 5.2 to 5.6).

A mathematical description of Young's experiment, considering both temporal and spatial coherence, leads to the definition of the mutual coherence function, which gives the degree of coherence (temporal and spatial) between two laterally separated radiators. The propagation of the mutual intensity (using paraxial approximation) is described by the Van Cittert-Zernike theorem.

For instance, the Airy disk issued from the diffraction of a plane wave through a circular aperture is a sign of temporal coherence (the wave has one single wavelength), as well as spatial coherence (the wave is plane).

3.4.2 Michelson interferometer: stationary configuration

One application of the results obtained from Young's experiment is the determination of the maximum allowed acceptance angle θ in a stationary Fourier spectrometer, as it will be described in chapter 4. The configuration is shown in Fig. 3.14.

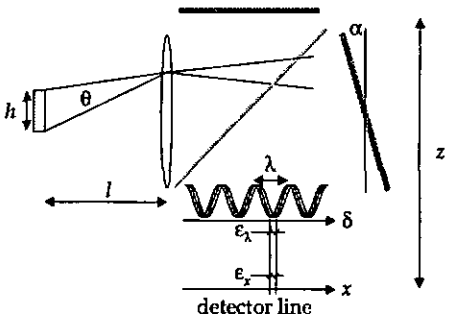

Figure 3.14: Configuration for a spatially modulated Fourier transform spectrometer, based on a Michelson interferometer with a tilt mirror, without imaging lens. The important parameters are the lateral extension of the source h, the distance from the source to the collimation lens l, the divergence angle (or acceptance angle) θ, the tilt of the mirror α, the wavelength λ (in order to determine the maximum acceptance angle, one takes $\lambda_{\min}$), and finally the distance z from the interference plane to the detector.

The setup parameters that influence the visibility of the interference pattern are listed in Fig. 3.14. The crucial parameter is the divergence angle θ, which causes a shift of the interference pattern. This shift is a function of the setup parameters. In order to know how large can be the shift ε_λ in term of wavelength for a contrast of 50%, the following integral has to be solved:

$$I(\delta, \varepsilon_\lambda) = \int_{-\varepsilon_\lambda/2}^{\varepsilon_\lambda/2} 1/2 + 1/2\cos[2\pi/\lambda(\delta+\varepsilon)]\mathrm{d}\varepsilon. \tag{3.23}$$

Then, the calculation of the corresponding contrast $C = (I_{\max} - I_{\min})/(I_{\max} + I_{\min})$, gives:

$$C(\varepsilon_\lambda) = \mathrm{sinc}(\pi\varepsilon_\lambda/\lambda). \tag{3.24}$$

The first zero of this function is at a shift corresponding to λ and the contrast is 50% when the shift is $\lambda/1.67$ (see Fig. 3.15).

The path difference δ depends on the tilt of the mirror α as $\delta = \tan[2\alpha]x \cong 2\alpha x$, where x is the position on the line detector. The shift ε_λ of the interference pattern can be expressed in terms of the shift ε_x over the detector line:

$$\varepsilon_\lambda = \varepsilon_x 2\alpha. \tag{3.25}$$

The behaviour of the contrast can be rewritten: $C(\varepsilon_x) = \mathrm{sinc}(\pi\varepsilon_x 2\alpha/\lambda)$. The shift $\varepsilon_x \cong z\theta$ is determined by the divergence angle $\theta \cong h/l$. Then, the contrast C as a function of the setup parameters becomes

$$C \cong \mathrm{sinc}(\pi\frac{z\theta 2\alpha}{\lambda}) = \mathrm{sinc}(\pi\frac{zh2\alpha}{\lambda l}). \tag{3.26}$$

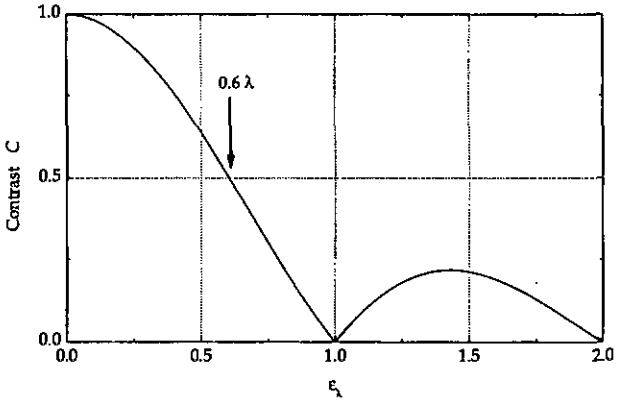

Figure 3.15: Contrast C in function of the shift ϵ_λ given in wavelength. The contrast is 50% when the shift corresponds to about $\lambda/1.67$.

Note that in order to have a parallel beam, l is equal to the focal length of the collimating lens.

In order to keep a contrast always higher than 50%, it follows that the setup parameters are related to each other by the relation

$$z \leq \frac{l\lambda/1.67}{h2\alpha}, \tag{3.27}$$

as shown in Fig. 3.16. At a distance z of 3 mm, the maximum acceptance angle is 0.011 rad. For practical reasons, if a collimation lens with a numerical aperture $N4$ equal to 0.2 is desired, then, in order to illuminate the whole detector line, a focal lens of 33 mm has to be used (we assume a 512-pixel detector with a length of 13 mm). It follows from Eq. (3.27), that the the lateral dimension h of the source must be smaller than 360 μm.

Cylindrical lens.

In a spatially modulated Fourier spectrometer a cylindrical lens can be used to increase the throughput. This is shown in Fig. 3.17.

The issue of the maximum acceptance angle can be solved by treating the problem separately in the x-direction (parallel to the modulation) and in the y-direction (perpendicular to the modulation). The acceptance angle θ_x is given by Eq. (3.27) (where $h/l = \theta_x$) and the consequences have been discussed in this section. On the other hand, the acceptance angle θ_y can be set by following the discussion in section 2.3.3. The major contrast loss due to θ_y is obtained at the border of the interferogram, where the optical path difference is maximum.

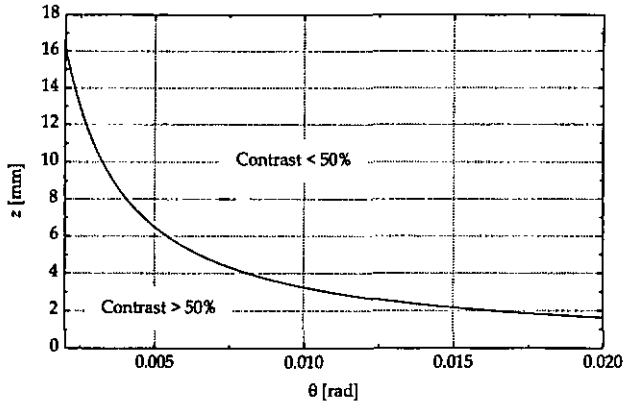

Figure 3.16: Distance z from the interference plane to the detector as a function of the divergence angle $\theta = h/l$. Wavelength $\lambda = 380$ nm and tilt of the mirror $\alpha = 3.5$ mrad, corresponding to a cutoff wavelength of $\lambda_{\min} = 350$ nm for a pixel pitch of 25 μm.

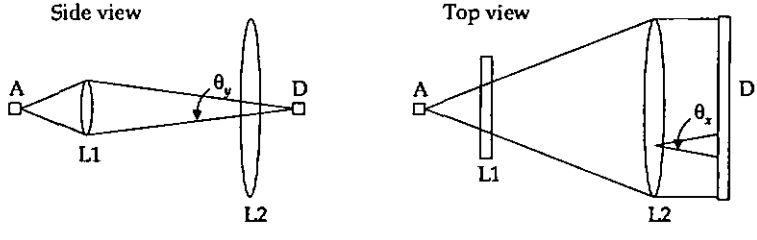

Figure 3.17: Using a cylindrical lens to gather the light diverging in the y-direction. A: aperture; D: detector line; L1: cylindrical lens; L2: collimating lens; θ_x: divergence in the x-direction; θ_y: divergence in the y-direction.

Chapter 4

Stationary Fourier transform spectrometer

In this chapter, we present a miniature stationary Fourier transform spectrometer, which operates in the visible wavelength range. No moving parts, no imaging system and compactness are the characteristics of this spectrometer. It is functional for applications requiring moderate spectral resolution (10 nm) but a good stray light suppression in the blue region (better than 20 dB). Target applications are various. They include color measurements, industrial process control, enviroomental monitoring or medical diagnostics.

Commonly used FT spectrometers with moving parts require a high mechanical precision and provide medium to high resolution. For historical and practical reasons, their main applications spread from the near to the far infrared, particularly in astronomy. Nowadays applications in the ultraviolet are found [60, 61, 62, 63, 64] bringing even higher requirement concerning mechanical accuracy, optical quality of the compooents and the type of materials.

The principal advantage of stationary FT spectrometers is the absence of a mobile mirror, since the interferogram is spread in space rather than in time. For the detection, a photodiode array (PDA) is necessary to record the interferogram instantaneously. The resolution is limited by the relatively small amount of sampling points (or pixels of the PDA), contrary to a scanning configuration where the major limiting factor is the maximum achievable path difference. Therefore, the ambition of spatially modulated and static-type Fourier spectrometers is to be stable, compact and robust enough to operate as portable sensors; their aspect is mostly monolithic and their tolerance against vibrations has to be strong. Due to the fact that a PDA is used, their wavelength range is oormally restricted from the ultraviolet to the near-infrared, since detector arrays for different wavelengths are non-standard.

A wide variety of instrument configurations are used. At first, when no detector arrays were available, Stroke and Funkhouser [65] proposed the technique of holographic spectroscopy to overcome the disadvantage of conveotional Fourier transform method (high accuracy scanning and substantial computational need). They recorded the interference pattern from a compensated Michelson-Twyman-Green interferometer on a photographic plate and demonstrated that re-illumination with coherent light would then display the spectrum of the source. In other words, the reconstruction of the spectrum from the

interferogram was performed optically. This work has later been extended using triangle [66], Lloyds mirror [67] and Mach-Zender-type interferometers. A simple and extremely cheap method using photographic recording was proposed by Billings [68]. This method was consisting in a z-cut plate of a uniaxial crystal placed between circular polarizers.

The advent of PDA and the advances in computers made possible the rapid recording of spatially distributed interferograms. Between several possible configurations listed hereafter, the Michelson interferometer (mostly used in time-scanning instruments too) is the classical one. It has been proposed in various configurations arranged with imaging optics [45], without imaging optics and a gathering cylindrical lens [69]. Additional amplitude splitting devices use the so-called Sagnac (or triangle-path, or common-path) interferometer [70, 71, 72]. A variation is suggested in reference [73] and consists in square-and-triangle topology. The considerable advantage of common-path configurations is the total independence of the contrast of the interference from the extension of the source. These spectrometers do not normally make use of an aperture, but they need a collimating lens to Fourier transform the source onto the detector. The concept of wave-front-dividing is presented either with stepped mirrors [74] or a double-mirror arrangement. Finally, interferometers exploiting polarizing effects of birefringent materials have been developed, for instance with a Savert plate [75] or a Wollaston prism [76]. In addition, a recent study [58] has shown that polarizer spectrometers can be built using liquid crystal technology, allowing extremely compact and low-cost devices. They avoid any collimating or imaging optics and are able to detect the interference pattern at the place of its creation.

Usually, despite the amount of studies, the investigated instruments never go beyond the stage of prototypes and, nowadays, only dispersive (e.g. grating) devices are widely commercially available. The principal reason is the relatively high cost (compared to a dispersive method) brought on by the optical components, as well as by the alignment and assembly steps. Then, these limitations do not counter-balance the higher throughput offered by stationary Fourier spectrometers for the common applications listed above. Note that the work of Boer et al. [58] pretends to get rid of those restrictions.

In the following sections, we experimentally investigate the potential and limitations of static-type Fourier spectrometers. Initially, we present experiments carried out with a modular Michelson interferometer having a tilted mirror. The results are used either to describe the performance, or to study specific aspects of a given configuration. Emphasis is put on the straylight suppression ability and the relevance of the background distribution (typical for any stationary configuration), which represents the larger amount of disturbance in the spectrum. Both aspects are associated to the performance of these particular spectrometers, taking into account the applications. Therefore, the influence of the background over the straylight suppression is studied. In addition, we present some methods to improve the straylight suppression, either by removing the background distribution, or by processing the interferogram in order to reduce the background effect. In the last two sections of the chapter we present a prototype based on a miniaturized Michelson interferometer and built with a non-conventional shape of the beamsplitter.

4.1 Preliminary experiments

In the following, we present a series of experiments carried out with a Michelson interferometer having a tilt mirror. The major goal of this study was to run measurements with a modular apparatus permitting to vary the essential set-up parameters in order to quantify their influence on the performance. In other words, we analyze the behaviour, the potential, the limitations and the possible improvements of a device with given configuration. Most of these evaluations are not possible with the device presented later, since the geometry and the components are fixed. Note that the presented aspects are typical for stationary Fourier spectrometers and most of them do not apply to scanning configurations.

The set-up is shown in Fig. 4.1. The interference pattern generated by the tilt of the

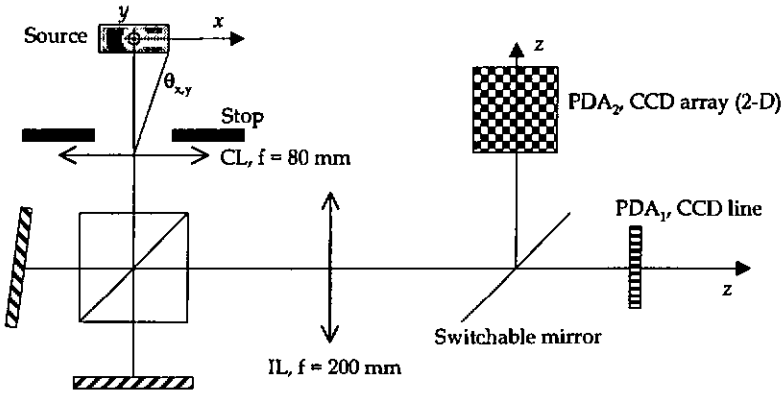

Figure 4.1: Michelson interferometer used as stationary Fourier spectrometer. CL: collimation lens; IL: imaging lens; PDA_1: CCD line (Hamamatsu, 512 or 1024 pixel, 16 bit); PDA_2: 2-D CCD array (1024 × 1280 pixel, 12 bit).

mirror is recorded by a CCD line (PDA_1), whose position can vary along the z-axis. The collimation lens makes an image 1:1 of the two mirrors (i.e. the interference plane) onto the detector. The angle of the tilt mirror can be set as desired in order to choose a given maximum optical path difference δ_{max} or a minimum accessible wavelength λ_{min}. The quality of the fringes (verticality and eventual distortion arising from misalignments) can be checked on-line by means of a 2-D CCD array (PDA_2). The choice of the PDA is made by a switchable mirror placed between them and the imaging lens. The beamsplitter is a 5 cm cube (splitting 50:50). Sufficient space is left between the beamsplitter and the mirrors in order to insert optical elements like polarizers or glass plates. The source is generated by a diffusing surface illuminated in transmission and covered by a 2-dimensional stop, which can be opened to 25 mm × 25 mm. If a laser source is used, the light is first scattered by an additional rotating diffuser as shown in Fig. 4.2. In this manner a spatially incoherent monochromatic light source with a nearly Lambertian distribution

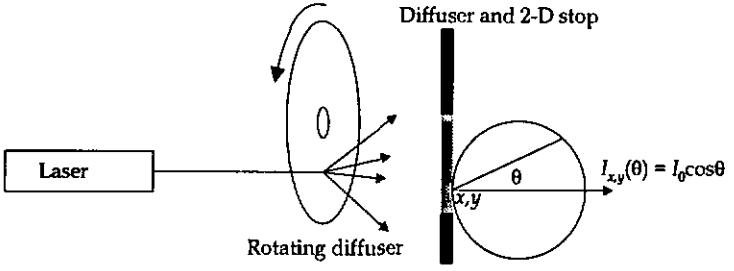

Figure 4.2: Layout of the light source considered in the setup.

can be created. By varying the width and height of the stop, we can set a field of view. In other words we vary the angle between the source and the collimation lens: θ_x stays for the divergence angle in the x-direction (slit width) and θ_y stays for the divergence angle in the y-direction (slit height), as shown in Fig. 4.1. The samples and filters to be analyzed are put in front of the diffusing surface.

Apodization functions

As will be shown, apodizing function are not only applied to minimize sidelobes engendered by truncation (see section 2.3.2). In reality, this undesired effect does not have harmful consequences since we measure mainly broadband spectra. In our case (especially when the spectrum is highly broadband), apodization is one of the methods proposed to reduce the influence of inhomogeneous background distribution on the straylight suppression ability of the spectrometer.

Three different apodizing function were used and studied (see section 2.3.2)

1. Triangle: $1 - |x_n - N/2|/(N/2)$ (goes to zero at the edges),
2. Hamming (or Happ-Genzel) [30]: $0.54 + 0.46\cos[\pi(x_n - N/2)/(N/2)]$ (8% at the edges),
3. Gauss: $\exp[-\pi(x_n - N/2)^2/(0.41N)^2]$ (1% at the edges),

where N is the total number of sampling points and x_n their respective position. A trade-off between loss of resolution and straylight suppression ability has to be chosen, and the performance of the spectrometer will then be determined by the best resolution/straylight-suppression ratio.

Transmission spectrum

The transmission spectrum $T(\lambda)$ of a sample is the ratio between the measured sample spectrum and the white light spectrum used for the measurement (see also section 3.1 and Eq. (3.1)). For comparison interest, when we shall talk about straylight suppression

in the blue region (typically with a GG495 filter), a distinction will be made between *transmission spectrum* and *simple spectrum*. In fact, the value of the suppression depends strongly on the type of white light that is used. We introduce the notion of straylight suppression with transmission spectra, since the evaluation of a given spectrometer (when compared with other spectrometers) is realized with a given type of illumination.

4.1.1 Straylight suppression

The suppression spectrum $S(\lambda)$, as well as the reference value SU used to quantify the straylight suppression ability is defined in section 3.1. Additionally, the suppression capability is determined with monochromatic radiation (at 633 nm) and, in this case, is defined as the mean value of $S(\lambda)$ between 400 nm and 550 nm. In case of *simple spectra*, the suppression is calculated by normalizing to spectrum to 1.

Type of white light spectrum

Figure 4.4 shows typical suppression spectra of a GG495 filter, measured with a halogen, a xenon low-pressure and a xenon high-pressure lamp, whose spectra are shown in Fig. 4.3. It is important to note the difference between the lamps used to measure a transmission spectrum. The higher the amount of spectral power in the blue, the higher the suppression in this region. On the contrary, almost no difference is noticeable when the suppression of simple spectra is considered, which is the reason why this approach is used to compare the performance. Note that the slightly lower suppression for both xenon lamps (curves (b) and (c)) is due to the own transmittance of the GG495 filter (the halogen lamp has practically no spectral power in the blue).

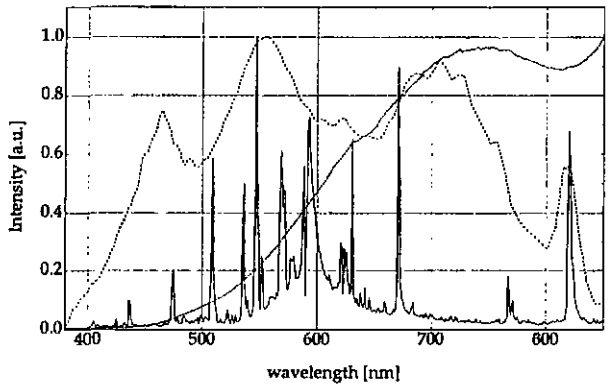

Figure 4.3: Spectra of white light lamps used in our experiments: xenon low-pressure (solid); xenon high-pressure (dashed); halogen (dot-dashed).

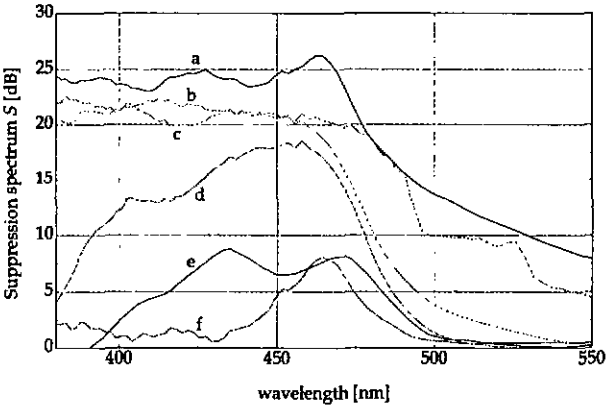

Figure 4.4: Suppression spectra of a GG495 filter (long-pass 495 nm): (a) simple spectrum with a halogen lamp, (b) simple spectrum with a xenon low-pressure lamp, (c) simple spectrum with a xenon high-pressure lamp, (d) transmission obtained with a xenon high-pressure lamp, (e) transmission obtained with a xenon low-pressure lamp, (f) transmission obtained with a halogen lamp. Note that the curves are smoothed (10 points) in order to facilitate the readability of the graph.

Straylight near a monochromatic line

As mentioned, the straylight suppression ability can be evaluated with monochromatic radiation (see Fig. 4.5). An additional feature is considered here: the width of the line at a suppression of 20 dB. This value decreases when the interferogram is apodized, contrary to the full width at half maximum (FWHM). In Fig. 4.5, the curve has not been smoothed, unlike to Fig. 4.4.

Straylight, number of sampling points and length of coherence

In Fig. 4.6, we have plotted the SU values for a GG495 filter, a monochromatic filter (633 nm) and a red HeNe laser. For each measurement, we have varied the number of sampling points and applied different apodization function. The interferogram is truncated and then apodized. The optical path difference between two neighbour pixels is constant. Of course, the background distribution is not removed in order to examine the efficiency of the respective apodizing filters, as well as to observe the influence of inhomogeneities.

As mentioned by Barnes [71], noise introduced by spurious spatial variations of the intensity should not be ignored. This so-called fixed pattern noise gives rise to systematic noise. In reality, it is the ratio between the visibility (or contrast) and the noise pattern that matters. This is the reason why, if possible, the removal of the background should be carried out (this aspect is treated in the next section). Evaluating these effects is complex

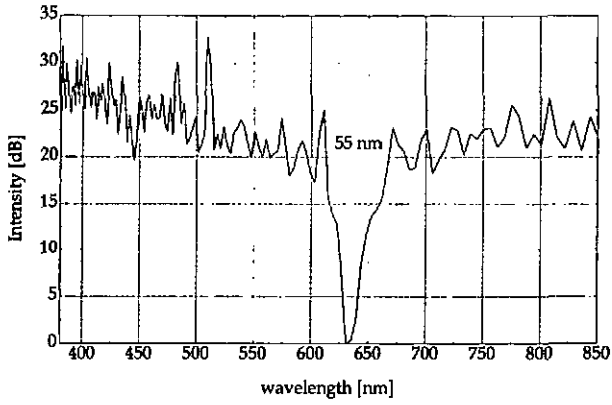

Figure 4.5: Normalized spectrum for a HeNe laser.

since each background is particular; nevertheless tendencies can be pointed out.

The first observation is the dependence of the straylight suppression ability SU on the number of pixels when the spectrum is broad: if the interferogram is not apodized, SU drops with N . The same behaviour is seen in scanning Fourier spectrometers and is commented by Chamberlain [7, p. 283]: the SNR in the spectrum increases up to the point where the oscillations are damped out, and beyond the noise will continue to increase with the path difference (see Fig. 3.9). In our case, it is possible to limit the influence of lack of contrast, and therefore to gain SU, by apodizing the interferogram. Nevertheless when the apodization filter is weaker, SU deteriorates again (see Fig. 4.6, left).

The relation between SU and the point where the contrast is lower than a certain value is shown by the three diagrams of Fig. 4.6. For both the GG495 filter and for the monochromatic filter, SU starts to decrease when the visibility is 1%; for the first filter it occurs when the the interferogram is truncated with a width of about 320 pixel and for the second one at 380 pixel (independently of the shapes of the envelopes). Finally, if the length of coherence of the radiation is long enough, a larger number of used pixels gives a higher SU. Note that for the HeNe laser the general values of SU are lower because the effect of truncation is larger.

Best apodization

It appears clearly from Fig. 4.6 that the best apodization depends on the length of coherence. For broad band spectra, the Gauss filter is the more efficient. It may be understood by the fact that this filter damps the lateral part of the interferogram, which has a low contrast. Nevertheless the loss of resolution is high (almost the double in terms of FWHM, see Table 2.1). For narrow band spectra and line spectra, the triangle apodization seems to be most suitable.

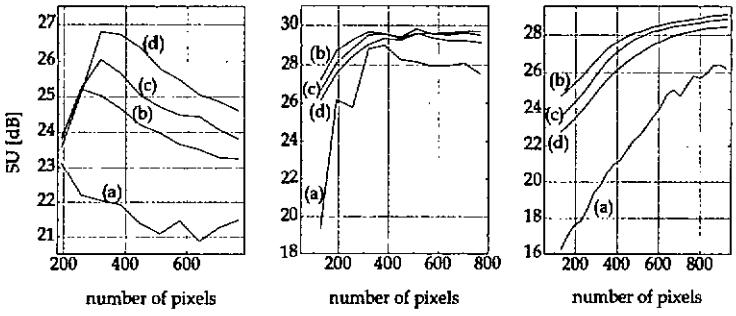

Figure 4.6: *SU* values of simple spectra of a GG495 long-pass filter (left), a monochromatic filter at 633 nm (center) and a red HeNe laser (right). They are represented as a function of the number of pixels N, and shown (a) without apodization, (b) with a triangle, (c) a Hamming, and (d) a Gauss apodization filter.

Straylight and sampling rate

So far, the tilt of the mirror has been kept constant (7.52 mrad). In the measurements presented previously, the minimum accessible wavelength λ_{min} was 376 nm. In other words the path difference between neighbour pixel was constant. In this series, we process the total number of sampling points N and we vary the tilt of the mirror in order to observe the influence of oversampling the interferogram. Fig. 4.7 shows 4 interferograms of the same spectrum with several sampling rate, each one corresponding to a different λ_{min}. The calculations of the straylight suppression are shown in Fig. 4.8 for a GG495 filter and a red HeNe laser, not apodized and apodized with a triangle, respectively.

These results indicate that there is a gain with a cut-off frequency which is close to the minimum wavelength to be observed. Even if with oversampling interferograms the visible fringes are spread over the whole detector (and eventual inhomogeneities are 'covered'), the resolution lost in reducing the angle of the tilt mirror does not allow to inspect sufficiently accurately the spectral frequencies corresponding to suppressed regions. In fact, diminishing the tilt makes the separation between neighbouring Fourier frequencies larger at a given frequency range.

It arises that the best δ_{max} is given by the tilt of the mirror corresponding to a λ_{min} close (and slightly inferior) to the minimum wavelength to be measured.

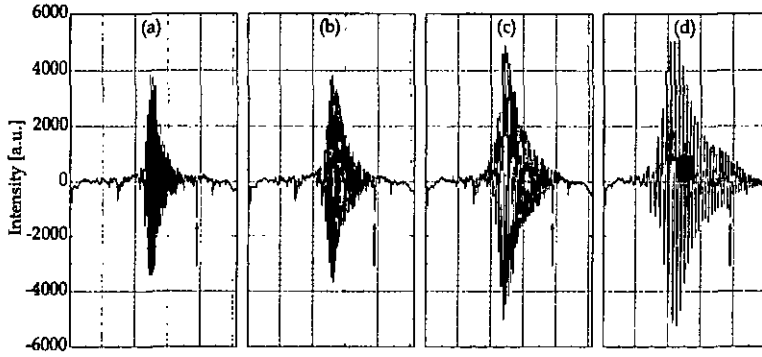

Figure 4.7: 4 interferograms of the simple spectrum of a GG495 filter used for the calculation of SU shown in Fig. 4.8. (a) $\lambda_{min} = 376$ nm, (b) $\lambda_{min} = 287$ nm, (c) $\lambda_{min} = 218$ nm, (d) $\lambda_{min} = 135$ nm. In these measurements, the interferometer is slightly dispersive. Note the position of one inhomogeneity of the background intensity distribution (arrow).

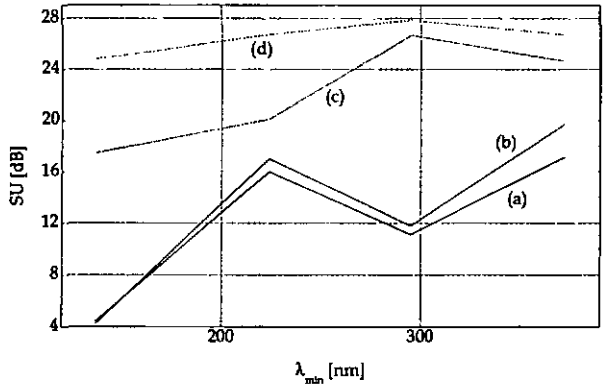

Figure 4.8: Behaviour of SU as a function of the minimum accessible wavelength λ_{min}. Simple spectra of a GG495 filter measured by means of a halogen lamp (a and b) and of a red laser HeNe (c and d), not apodized (a and c) and apodized with a triangle (b and d). The total number of sampling points is $N = 512$.

Final remarks

As far as the interferogram has oscillations corresponding to more than 1% of the useful dynamic range of the detector, it is worthwhile to consider an increased number of sampling points. As a matter of fact, a spectrum that needs to be resolved (e.g. emission or absorption lines, cut-off filters) will in any case give a modulation signal at high optical path differences. This means, following the previous considerations, that the only limitation will be the amount and the amplitude of the fixed pattern noise compared with the signal and the capacity of the device to discriminate the oscillation, in term of dynamic range. From the experimental point of view, we may restrict the wavelength range of interest by cutting the spectrum above 730 nm.

4.1.2 Background intensity distribution

In this section we present the importance of removing the fixed pattern noise or background intensity distribution. We shall introduce some experimental methods to record the background and to remove it from the interferogram. Finally, the gain in terms of straylight suppression ability will be shown.

Unfortunately, this systematic noise varies from setup to setup. Therefore, it would be best to determine the background for each measurement.

Methods

After apodization, which simply reduces (but does not eliminate) the effect of fixed pattern noise, the following methods can be considered to remove the background:

1. Record the intensity of one arm while blocking the other one, and vice-versa. This procedure is accurate but needs a three-step recording and shutters.

2. Tilt the mirror in order to get diagonal fringes. This method needs one mirror on a movable support. It may be laborious to recover the previous position.

3. Open the aperture to reduce the spatial coherence of the source. Consequently, the interference disappears. Note that the inhomogeneities are smoothed, since they are illuminated by an incoherent source.

4. Make the polarization of two branches of the interferometer orthogonal by means of linear polarizers. Here, a rotating element is needed and half the light is always lost. We have avoided this problem by placing two switchable liquid crystal (LC) cells in each branch. The LC cells polarize the light linearly when switched off. Nevertheless additional 50% of the light intensity is lost due to the poor transmission of the cell. In addition, the LC cells do not have a high enough polarizing effect to completely remove the interference.

5. Chirping the interference.

6. Record a monochromatic line and process it to find the position of the inhomogeneities. This method can mainly detect sharp features. However, when the intensity of the interference is low, the inhomogeneity is not visible. In this case, a measurement with an additional monochromatic line having a different frequency is necessary.

When the background is determined, we subtract it from the recorded interferogram, as shown in Fig. 4.9. In the ideal case, the background is measured immediately before or

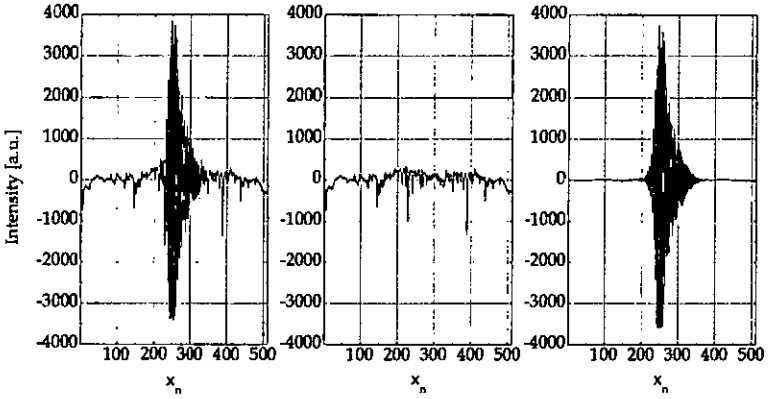

Figure 4.9: Interferogram (left) without and (right) with background removal. The subtracted background is shown in the center.

after the interferogram. If this is not possible, the background is recorded once and then multiplied by a factor proportional to the mean intensity of the interferogram, before being subtracted.

After having investigated these methods, we have chosen, in our measurements, to apply a sequential recording of each arm of the interferometer (method ♯1). For the prototype, we recorded the background by tilting the mirror before gluing it and used this result as a calibration (method ♯2).

Finally, note that for configurations where the interference is created by birefringent elements, the background can be obtained from the in-phase and the antiphase interferogram [75, 77].

Straylight and number of pixel

Contrary to 'dirty' interferograms (see section 4.1.1), reducing the number of sampling points does not affect the straylight suppression ability, whatever the apodization is. Table 4.1 demonstrates the obvious gain in *SU* for a GG495 filter when the background is removed .

Table 4.1: *SU* values in [dB] for a GG495 filter with ('clean') and without ('dirty') background removal.

	dirty	clean
No apodization	17.4	25.4
Triangle	20.0	25.7
Hamming	20.0	25.6
Gauss	21.2	25.7

4.1.3 Statistical noise

We consider now statistical noise, in opposition to fixed pattern noise. This topic has been abundantly treated in the history of Fourier spectroscopy (see sections 2.4 and 3.3).

In this section, we characterize the noise given by the PDA, and estimate the SNR in the spectrum in relation with the SNR in the interferogram. Additionally, tendencies for the standard deviation are given as a function of the number of sampling points and the intensity. Finally, we shall introduce the notion of jitter noise.

Detector noise

The linear image sensor used was a 512 pixel Hamamatsu S5462-512Q, consisting of 512 separate silicon photodiodes in line. The size of each diode cell is 25 μm $\times$ 500 μm. The readout is processed with dedicated electronics supplied by the University of Karlsruhe. It delivers a 16-bit digital signal.

We start by describing the noise when no interference is detected. Fig 4.10 shows the dark current for each photodiode cell with their respective standard deviation. From Fig 4.10, we note that the dark current is different for different pixels in the detector. The results are plotted in grey level units. Knowing that the dynamic range is 16 bit (65536 levels), we find that the dark current has an offset corresponding to 0.2% of the total dynamic range, and that its standard deviation is equivalent to 2 bit. When intensity is detected, a pattern appears which corresponds to the different sensitivities of each pixel (Fig 4.10 lower left). These dissimilarities are in the order of 0.1%, but for isolated cases can rise to 0.5%. Note that at full dynamic the standard deviation corresponds to 8 bit. When the background cannot be measured, the pattern shown in Fig 4.10 lower left has to be removed.

Figure 4.11 shows that the behaviour of the noise level in term of standard deviation in a function of the averaged intensity is linear. The SNR is constant and equal to 40000, which means that we have a multiplex disadvantage (see section 2.4.1, also described in Reference [78]).

Noise in the spectrum

As mentioned previously, the background intensity distribution gives rise to a fixed noise contribution in the spectrum. Fig. 4.12 shows that no statistical noise contribution is

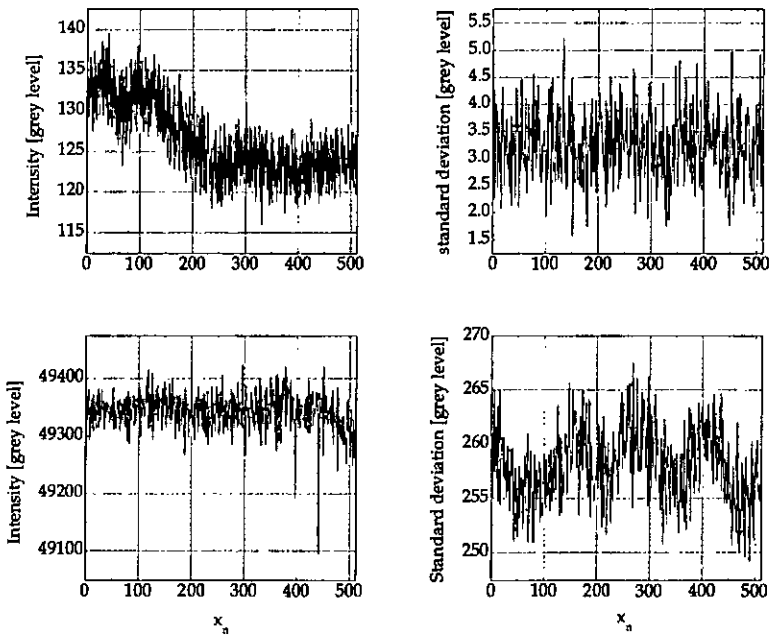

Figure 4.10: Upper left: dark current of each pixel of the Hamamatsu PDA for an integration time of 40 ms. Upper right: standard deviation of each pixel. Lower left: difference in pixel sensitivity to the collected intensity. Lower right: respective standard deviations.

added when the background is not removed. In reality, even if the spectrum issued from the dirty interferogram appears a lot more agitated (dashed line in Fig. 4.12), it has the same amount of statistical noise as the spectrum calculated from the cleaned interferogram.

Note that for the previous measurement (broad band) the SNR is about 8000. Performing a measurement with different band widths leads to notice that for a medium band (width of 100 nm) the SNR is 20000 and for a narrow band (monochromatic line), the SNR is about 27000. This leads us to presume that, like before, the amount of pixels effectively recording a modulation is an important parameter.

Jitter noise

The study of statistical noise in the spectrum is a complex task. The study should first take into account the type of spectrum, and then it will depend on a variety of parameters like the maximum optical path difference, the number N of sampling points N and the average intensity of the interferogram. The previous analysis of the influence

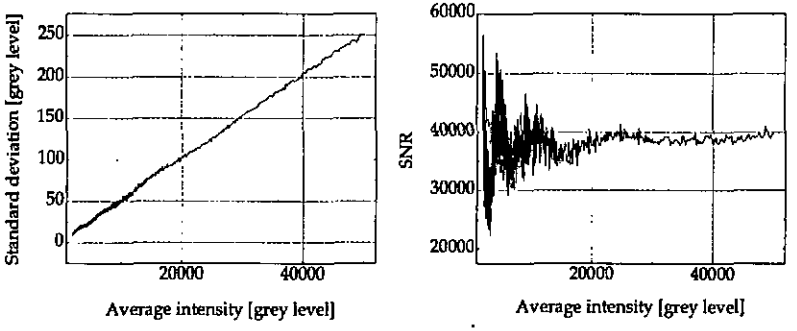

Figure 4.11: Left: standard deviation as a function of the detected intensity measured with a filter having variable transmission. Right: SNR as a function of the intensity.

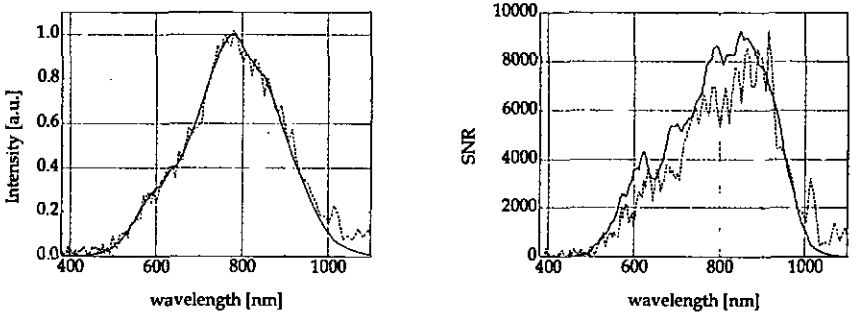

Figure 4.12: Left: Halogen lamp spectrum with (solid line) and without (dashed line) background removal. Right: SNR of the respective measurements.

these parameters in terms of straylight suppression can give an estimate. Some trends can be pointed out by regarding the standard deviation and the signal-to-noise ratio for given spectra when several measurements under identical conditions are performed.

As a function of the tilt of the mirror, it is seen in Fig. 4.13 that the SNR tends to lower with the increasing of the considered pixel number, except when the spectrum is small narrow band. Concerning the average intensity of the interferogram, no sufficient explanation can be given. Except a general decreasing tendency of the SNR in function of N, no simple description of the role played by the effective used dynamic range of the detector can be given. Keeping an equal contrast, low intensity interferogram should contain less noise (see Fig. 4.11). On the other hand, they do not benefit from a large dynamic range.

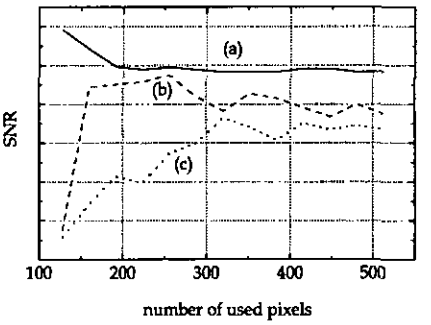

Figure 4.13: SNR for (a) broadband spectrum, (b) medium band (550 nm to 650 nm) and (c) a narrow line.

Finally, an additional contribution arises from the sampling jitter, which gives a higher noise contribution at positions where the slope of the recorded modulation is high (see Fig. 4.14). A study by Kolar [79], has shown that noise produced by jitter is relevant in the UV-VIS region.

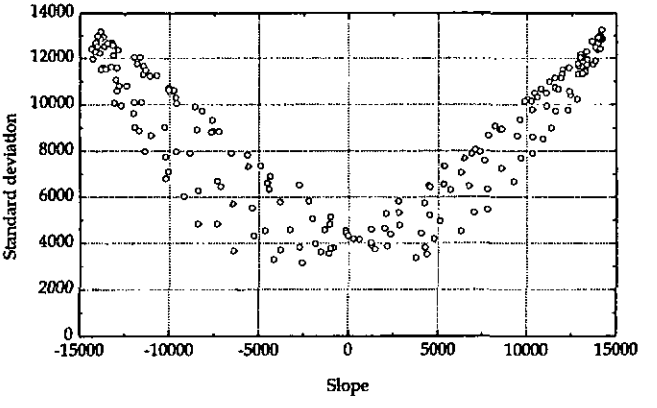

Figure 4.14: Dependence of the slope of the modulation of a narrow line with the standard deviation at the respective sampling positions.

4.2 Description of the prototype

We describe now a Fourier transform spectrometer based on a stationary Michelson interferometer, which uses a non-conventional construction of the beamsplitter. The motivation for this particular design was to realize a compact system. The principle is shown in Fig. 4.15. The beamsplitter is of elongated construction as shown in Fig. 4.15 and has

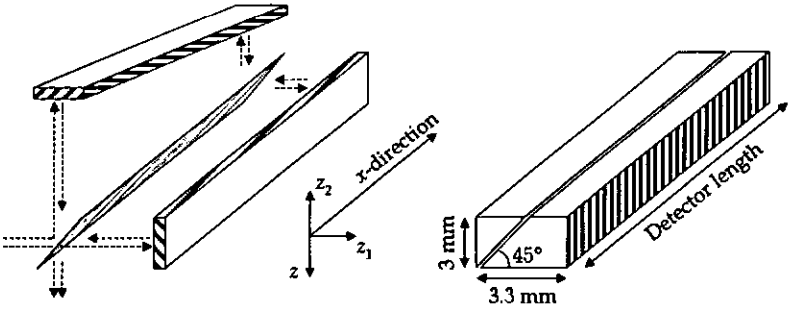

Figure 4.15: Left: Principle of the stationary FT spectrometer using a non-conventional configuration. Right: Drawing of the beamsplitter used in the setup. One surface of the beamsplitter is coated with aluminum.

a cross-section of 3 mm × 3.3 mm; its length is adapted to the detector size.

In 1970, Girard [80] described a device for stellar spectroscopy, which was using a similar beamsplitter. The interferogram was recorded by mean of a single detector moving along the x-direction. Girard named this particular configuration 'air wedge fringes' interferometer.

This uncommon geometry of the beam splitter permits to drastically shorten the distance between the mirrors and the detector. This quality permits to avoid the use of a lens to image the interference plane onto the detector plane. In addition, contrary to cubic beamsplitters, this distance does not scale with the length of the PDA. In other words, as the resolving power is set by the number of pixels of the PDA, this arrangement is independent of the desired resolution. The reason for this choice is the desire to minimize the number of optical elements, as well as additional assembly and positioning steps.

As shown in Fig. 4.15, the beamsplitter has one face coated with aluminum, which avoids the use and handling of a second mirror. Note that, in theory, the limiting dimension of this configuration would be the height of the PDA pixels (500 μm in our case). Nevertheless, as will be shown here below, assembly is a delicate task and should not be neglected. Figure 4.16 shows an interferometer with optical components having an inadequate size. The dimension of the beamsplitter is 1 mm × 1 mm × 8 mm.

4.2.1 Mounting and assembly

A prototype has been constructed following the design presented previously.

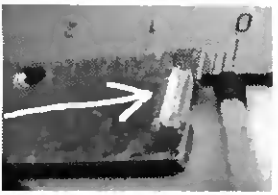

Figure 4.16: Left: Michelson interferometer realized with optical components, which are too small for an acceptable handling. Right: Interference pattern of a HeNe laser, which is unusable for satisfactory measurements.

In a first step, the beamsplitter is glued onto the silicon surface of the detector by means of UV-curing adhesive. The operation is carried out under a microscope.

Once the detector and the beamsplitter were mounted, we proceeded with a dedicated mechanical positioning holder shown in Fig. 4.17. It has been used in order to facilitate

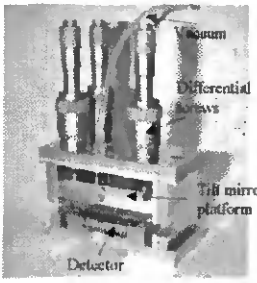

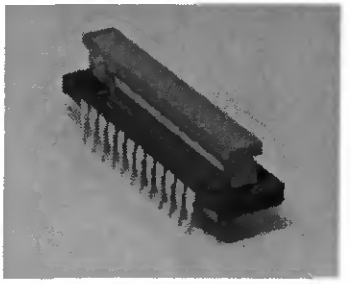

Figure 4.17: Right: Apparatus used to align and glue the tilt mirror with the beamsplitter and the detector. Left: Assembled interferometer with the line detector.

the installation of the tilt mirror. The mirror is attached by vacuum to the tilting plate. When the alignment process is done (i.e. the correct angle has been found) the mirror is glued at the edges by filling the free space with spacers. Then, the special support is removed.

The resulting device is shown in Fig. 4.17. It consists of a tilted mirror Michelson interferometer together with a CCD line. Finally, the unit is placed on a ground plate, on which the source and the collimation lens are adjusted. A photograph of the setup is shown in Fig. 4.18. The dimensions of the prototype are essentially determined by the focal length of the collimation lens together with detector width. In our case, we used a focal length of 100 mm.

Note that we used a multimode fiber (core diameter is 100 μm at the input), which enables us to probe comfortably the light source to be analyzed.

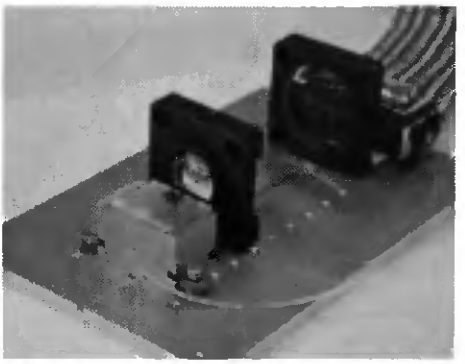

Figure 4.18: General view of the miniature FT spectrometer, comprising the input fiber, the cylindrical lens and the collimation lens.

4.2.2 General characteristics

The prototype uses a Hamamatsu 1024 pixel linear image sensor. The achieved optical path maximum is 187 μm, corresponding to an angle of the tilt mirror equal to 3.7 mrad and a cutoff wavelength λ_{min} of 366 nm. According to Eq. (2.58) (and keeping in mind that in the cited equation, δ_{max} is considered for a one-sided interferogram), we get a theoretical resolution $\delta\lambda = \lambda^2/\delta_{max}$ of 2.1 nm at 633 nm.

The effective wavelength range of the spectrometer is 366 nm to 1100 nm with a resolution better than 10 nm. The spectral response of the CCD line vanishes for longer wavelengths.

The background intensity distribution had been recorded before the gluing step by tilting the mirror and pushing the zero path difference off the detector. The background intensity is shown in Fig. 4.19. This result is used in the measurements, following the procedure presented in section 4.1.2.

The specific configuration of the interferometer leads to a strong dispersion effect, due to the light traveling through BK7 in one arm and through air in the second arm. The recorded interferograms are therefore highly asymmetric. Of course, the recovery of the spectrum is not compromised. Nevertheless, apodization cannot be applied and, therefore, the background intensity distribution has to be removed.

4.2.3 Distortion of the mirror

The issue of distortion is treated now. The phase correction in relation with the physical deformation of the mirror has to be applied for any interferogram.

The interferogram of a HeNe laser was measured before and after the gluing step. It appears that the spectrum after gluing is distorted. The tilted mirror has a thickness of 1 mm over a length of 38 mm and it has been bent during the gluing step. Figure 4.20 shows the deformation of the mirror. We observe a maximum peak-to-valley distortion

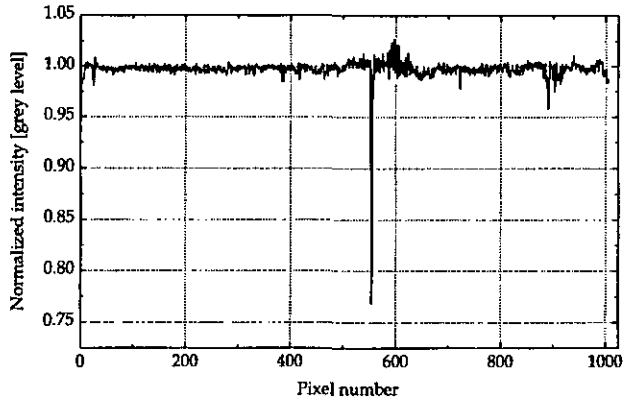

Figure 4.19: Background intensity distribution of the prototype. The peak coincides with a dust particle on pixels number 554 and 555. The intensity is normalized to 1.

of about 0.5 μm over the length of the detector (25 mm), which is enough to cause an important discrepancy in the spectrum shown in Fig. 4.21.

Phase correction procedure

To get rid of the distortion effect, we need to identify the exact phase at each sampling point, which is obviously not linear anymore. The procedure consists in measuring the position of the points where the modulation of a monochromatic radiation crosses the x-axis (see Fig. 4.15). We use either a linear or a sinusoidal interpolation. The second one is more realistic. Then, the result is transposed via a polynomial interpolation to the real position of the pixel. The result is shown in Fig. 4.20, which gives the phase delay in terms of pixels for each pixel position.

The distortion Δn is applicable to every frequency and is taken into account in the Fourier transform as

$$B_m = \sum_{n=1}^{N} F_n \exp[i2\pi m(n - \Delta n)/N], \tag{4.1}$$

where m are the Fourier frequencies and F_n the interferogram values sampled at the position n.

4.3 Characterization and results

In this section we show the performance of the prototype, in particular the straylight suppression and resolution. Additionally, we present measurements with typical spectra, as well as colour calculations.

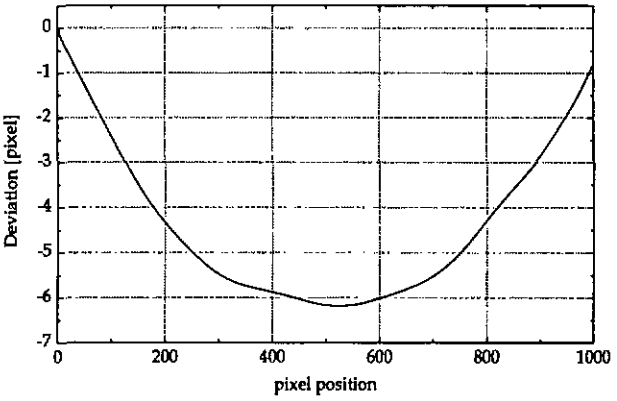

Figure 4.20: Distortion of the mirror given in pixels. The optical path difference between neighbour pixels is given by the cutoff wavelength. In this particular situation (λ_{min} = 366 nm), the measured maximum distortion at the center of the mirror is 0.5 μm.

4.3.1 Straylight suppression and resolution

Figure 4.22 shows the suppression of the transmission spectrum of a GG495 filter measured with a xenon high pressure lamp, whose spectrum is shown in Fig 4.3. The measurement underlines the necessity of removing the background. Since no apodization is applicable, the straylight suppression ability of the spectrometer would not achieve the specifications. For this specific measurement, reducing the number of used sampling points does not enhance the suppression as one would expect after the considerations presented in section 4.1.1. In fact, the spreading of the interferogram due to dispersion, gives rise to modulations with a relatively high contrast at any place of the detector. In reality, the recovering of the spectrum needs a larger detector area than with a symmetric interferogram and cutting down the number of used pixels is harmful for the spectrum.

The significance of expanding the interferogram over the detector area and its repercussion on the suppression is seen in Fig. 4.23. This graphic shows the close relation between the contrast of the central fringe and the suppression. As soon as the contrast reaches roughly 50 %, the suppression is close to 20 dB. In fact, in case of a RG695 filter, the interferogram expresses a higher degree of symmetry, firstly, because the length of coherence is longer (the spectrum extension is about 150 nm instead of 450 nm for the white light), secondly, because the dispersion effect is lower in this wavelength range. Therefore, it seems from the previous considerations that dispersion deteriorates the suppression. Note that for a symmetric configuration, the suppression is not affected by the bandwidth, contrary to grating spectrometers, which show a clear dependence between straylight and bandwidth.

The resolution together with the suppression have been measured (Fig. 4.24). We notice the effect of apodization on the suppression, primarily because of the reduction

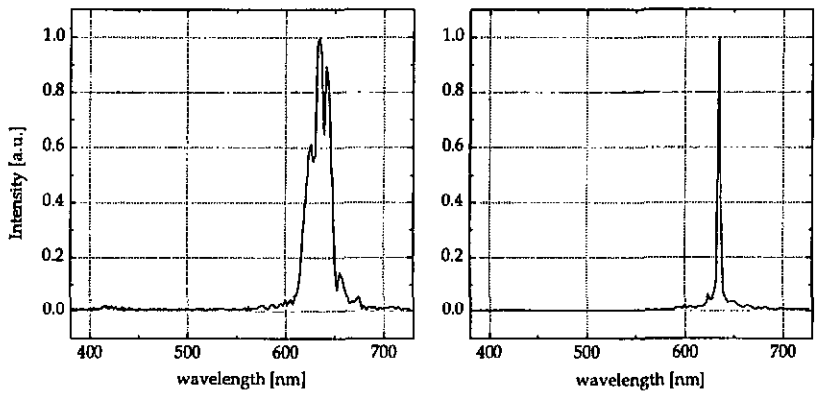

Figure 4.21: Left: spectrum of a HeNe laser recorded without phase correction. Right: spectrum after the phase correction for the distortion of the tilt mirror.

of the sidelobes. Additionally, apodization drastically reduces the width of the line at a suppression of 20 dB. The resolution in terms of FWHM are 4 nm and 5 nm for the unapodized and the apodized spectrum, respectively.

The position accuracy of the center of a line has been determined using the output of a monochromator as the source and by fitting the measurement with a Gaussian function (see Fig. 4.25). The phase correction due to the mirror distortion, measured previously with a HeNe laser, has been applied. The results are reported in Table 4.2.

Table 4.2: Accuracy of the center of several line spectra measured with the prototype.

Input wavelength	Center	FWHM
400 nm	401 nm	4 nm
460 nm	458 nm	5 nm
520 nm	519 nm	5.5 nm
580 nm	578 nm	6 nm
640 nm	640 nm	7 nm
700 nm	700 nm	7 nm

4.3.2 Measurements with weak sources

To qualify the performance of a given spectrometer, one can test its ability to measure weak sources. Fig. 4.26 shows suppression spectra of three neutral density filters. We note that the deviation from the original curved is only about 1.5 dB, even when the suppression is equivalent to 15 dB.

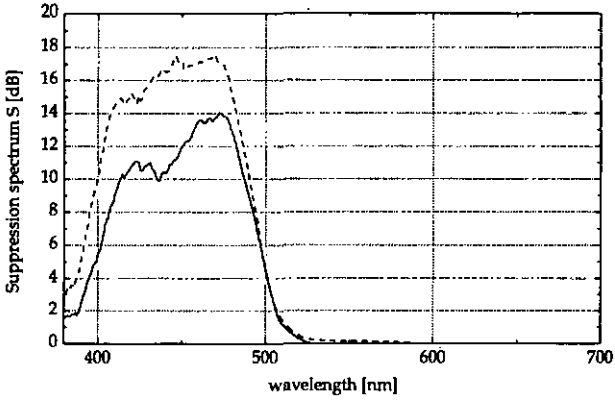

Figure 4.22: GG495 filter without (solid line) and with (dashed line) background removal. Suppression of a transmission spectrum measured with a xenon high pressure lamp. Simple spectra show a *SU* of 16 dB without removal and of 20 dB with removal.

4.3.3 Other spectra

Typical spectra have been measured and are shown in Figs. 4.27, 4.28 and 4.29

The spectrum of a xenon low-pressure lamp is composed of a series of sharp peaks and is a good test for the wavelength accuracy of the spectrometer. It can be used for calibration purposes, since the lamp is intense and, therefore, one does not deal with weak signals.

The spectrum of a BG36 filter is used to examine the suppression ability as well as the wavelength accuracy.

Finally, the Ar-Hg lamp intensity is weak and is adequate to examine the ability of matching sharp peaks even when the average recorded intensity is low.

4.3.4 Colour measurements

In Fig. 4.30, we show colour measurements of some typical fluids. The calculation of the colour and the CIE1931 diagram are presented in section 3.1.1.

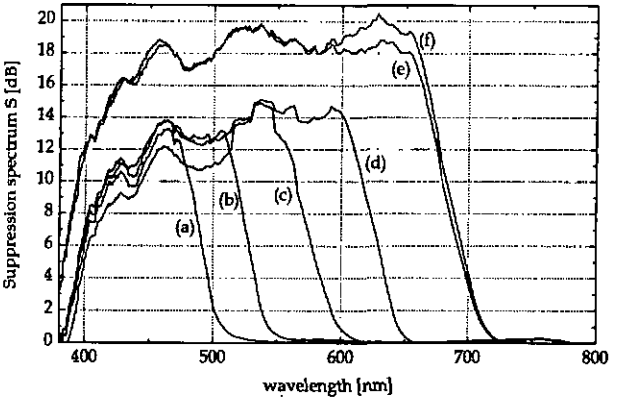

Figure 4.23: Suppression of transmission spectra of different short-pass filters measured with a xenon high pressure lamp. The contrast of the interferogram for each filter is: (a) GG495: 35%. (b) OG530: 39%. (c) OG590: 42%. (d) RG630: 58%. (e) RG695: 64%. (f) RG695 with an average intensity 5 times higher: 64%. The contrast of the white light was 29%. The background has not been removed

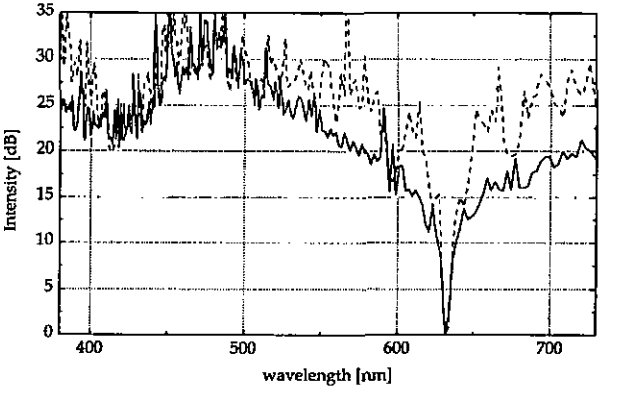

Figure 4.24: Normalized spectrum for a HeNe laser without apodization (solid line) and with a triangular apodization (dashed line). The interferogram was phase corrected as shown in section 4.2.3.

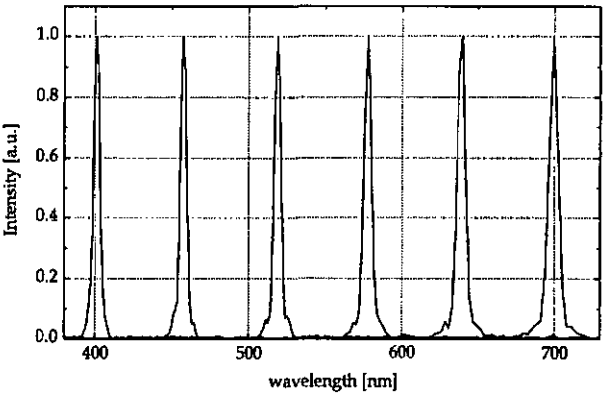

Figure 4.25: Line spectra. The source is the output of a monochromator. This measurement is used to determine the position accuracy of the center of a line.

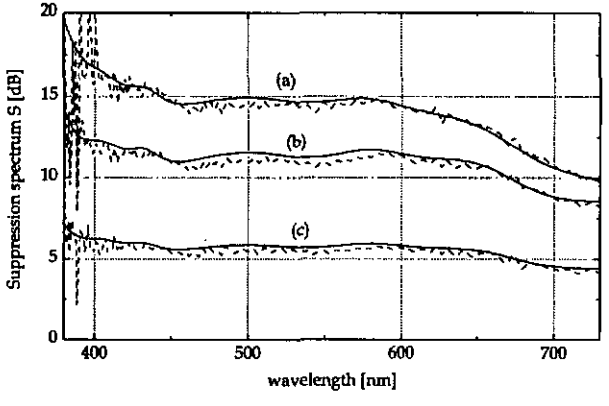

Figure 4.26: Suppression spectra (dashed curves) for several neutral density filters. (a) NG4 1 mm, (b) NG4 2 mm, (c) NG9 1 mm. The solid lines are the original suppression spectra of the filters obtained by a 1 nm resolution monochromator.

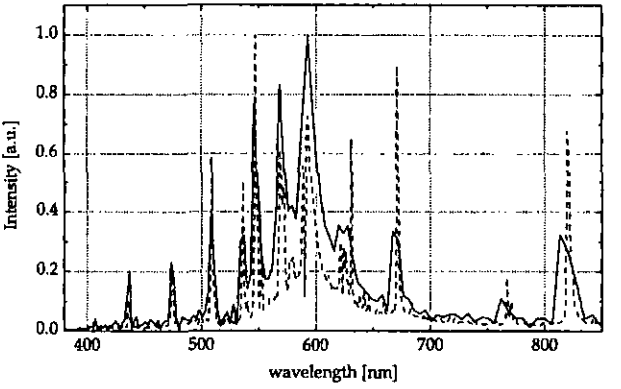

Figure 4.27: Spectrum of a xenon low-pressure lamp. The dashed line is the spectrum measured with a 1 nm resolution monochromator.

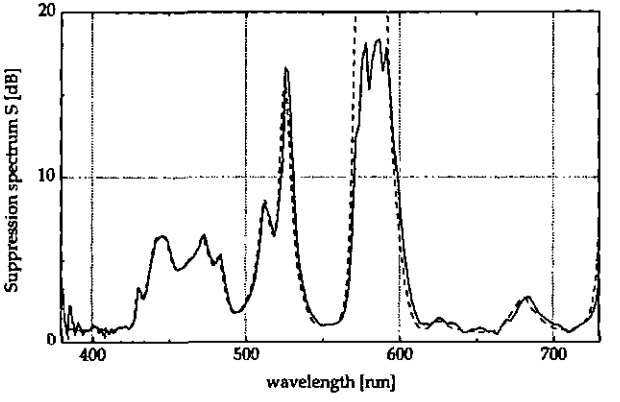

Figure 4.28: Suppression spectrum of a filter BG36. The dashed line is the spectrum measured with a 1 nm resolution monochromator.

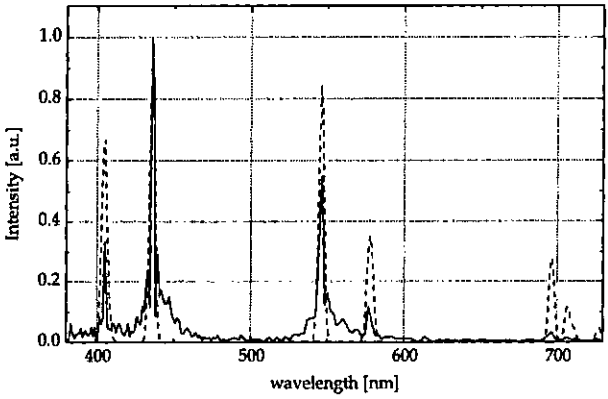

Figure 4.29: Spectrum of a Ar-Hg lamp from Ocean-Optics. The dashed line is the spectrum measured with a 3 nm resolution monochromator.

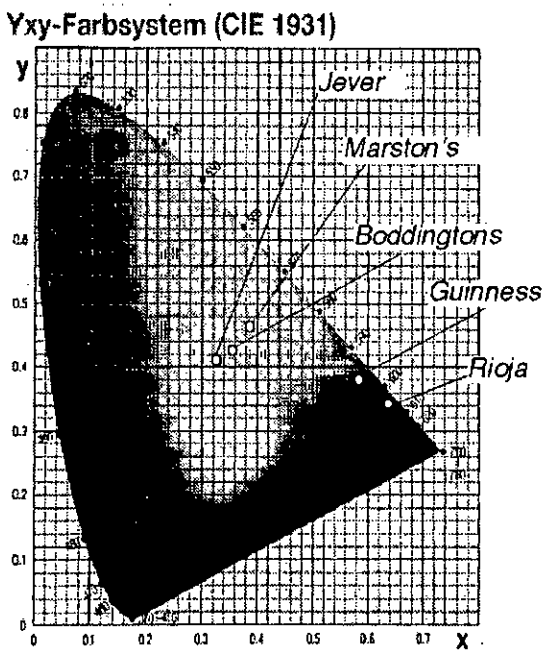

Figure 4.30: Colour measurements of different fluids.

4.4 Summary and conclusions

Investigating the potential of a particular stationary Fourier transform spectrometer is a vast exercise that relies on a variety of aspects and parameters. To restrict the area of study, a selection of applications has to be chosen and, therefore, specifications have to be set.

The key parameter chosen here is the straylight suppression ability of the spectrometer, especially in the blue region. The reason for that has been introduced in section 3.2.1.

It has been seen that fixed pattern noise is the greatest source of trouble and the background intensity distribution should always be removed in order to reach the best performance. If this is not possible, apodization, as well as cutting down the number of used pixels, can help, but only for symmetrical configurations. Of course, the results vary with the amount and type of inhomogeneities in the background.

For a simple spectrum of a GG495 filter, we have noticed that with a symmetrical configuration *SU* has been enhanced from 23 dB to 27 dB by apodizing and reducing the amount of unnecessary pixels and from 17 dB to 26 dB by removing the background. Note that the maximum values reported here above result from two different setups, having distinct backgrounds and are measured with a xenon and a halogen lamp, respectively.

In the case of a dispersive interferometer, the only possibility of enhancing *SU* is the background removal. We have observed an increase from 14 dB to 18 dB for a transmission spectrum (measured with a xenon high pressure lamp) and from 17 dB to 21 dB for a simple spectrum. Note the difference of 3 dB between simple and transmission spectra. The difference can be even higher with a different lamp type.

Following several measurements, one can observe a difference in performance between a symmetrical and a dispersive configuration. We may find the reason of that by considering the general contrast of an interferogram, together with the fact that the digital output of our PDA line has a noise which is proportional to the intensity. The spreading of the interferogram along the detector diminishes the local contrast and therefore the ratio between the modulation height and the noise. It might be that reducing the average intensity could enhance this ratio, but, on the other band, the dynamic range diminishes as well. We have noticed that a minimum contrast of the central fringe of 50% is necessary. Finally, we have observed a general loss of 1 dB in terms of suppression ability between the 512 and the 1024 pixel detector, which explains partly the difference between the symmetrical and the dispersive devices.

In both types of arrangements, the cutoff wavelength should be as close as possible to the minimum wavelength to be inspected.

As a consequence, we may be able now to give a saturation value for *SU* when the best case is taken into account. With a symmetrical configuration, the best performance (in terms of high straylight suppression and low loss of resolution) is achieved when a 512 pixel detector is used, the background is removed, a variable apodization is applied (150 pixel at 400 nm and 480 at 730 nm), and a high pressure xenon lamp is used in case of transmission spectra. In this case *SU* saturates at about 28 dB (equal to 0.17% of the intensity if the spectrum is normalized to 1). This corresponds to the measured statistical noise shown in Fig. 4.11. The average intensity is 20000 grey levels and the standard deviation corresponds to 0.15% of the dynamic range. With the prototype that

has been constructed, the saturation occurs at 21 dB after background removal.

We have mentioned that the SNR is constant as a function of the intensity. The consequence is a multiplex disadvantage compared to a grating spectrometer. The ratio of SNR between a grating and the interferometer scales with the square root of the number of spectral elements M (see also the introduction of chapter 2), which means that the disadvantage grows with the spectral bandwidth. Nevertheless, this type of interferometer keeps the advantage of large throughput compared with a grating. In fact, at equal performance a slit width of 2.4 mm can be accepted for the interferometer, compared with a slit of 100 μm for the grating.

In conclusion, we have presented a dispersive spatially modulated FTS based on a Michelson interferometer. A non-standard beam splitting configuration has lead to compactness and reduced demands concerning spatial coherence. Combined with a cylindrical lens, these features enhance the throughput. Measurements have shown that this type of spectrometer is well suited for applications in the visible wavelength range, which do not require a high resolution (better than 10 nm) but need a good stray light suppression (better than 1%).

Chapter 5

Fourier transform spectrometer based on silicon technology

In the previous chapter, we have examined the relevance of the Fourier transform technique for a number of applications that demand the utilization of portable and compact devices, but do not necessarily require a high resolution. The potential of miniature Fourier transform spectrometers have been discussed by considering a static-type Fourier spectrometer.

We report now on a Michelson interferometer with a scanning mirror. Despite the clear advantages of a stationary configuration, the time-scanning solution offers some benefits as well. The use of a single photodiode, instead of an array (PDA), eliminates the nuisance coming from the background intensity distribution. Then, the issue of resolution is not a limitation arising from the number of pixels of the PDA, but only from the maximum achievable scan distance of the mirror. In addition, the harmful influence of the size of the source is strongly reduced, since the mirrors are not tilted with respect to each other.

In the device presented in this chapter, the size, which is in the order of the millimeter, and the specific fabrication technology are fundamental assets. Together with the advantages offered by a scanning configuration, they provide a net profit for this particular solution.

In a scanning Michelson interferometer, the motion of the mirror is usually carried out by a piezo-electric system. A recent study [81] showed that silicon microfabrication can be used as an alternative method. In our situation, the mobile mirror is driven by an electrostatic comb actuator.

In this chapter, we shall give details about the technology that permits the fabrication of the Michelson interferometer, as well as the mobile mirror. Then, the experimental characterization of the motion of the mirror is presented and we shall demonstrate that the device is suitable for Fourier spectroscopy in the visible and near-infrared region with a resolution better than 10 nm. Finally, an overview of further potential designs taking advantage of the same technology will be given.

5.1 Optical micro-electro-mechanical systems

Micro-electro-mechanical systems (MEMS) include a vast variety of devices dealing with micromachining technology. After MEMS components have been built and used as sensors for chemical and physical signals, pumps, motors, and much more, the integration of optics, or the use of MEMS in combination with optical signals is considerably growing.

Optical MEMS (or MOEMS) technology plays an increasingly important role in domains such as telecommunications, optical networking, information storage, wireless technologies, environmental monitoring, remote sensing or display technology. Components and systems as various as optical bench on a chip, integrated optical laser scanners, microshutters or optical switches have been developed at industrial level. Therefore, the combination of microoptics, micromechanics and electronics exploited in order to create a wider class of integrated microoptical systems is a challenging new field.

Both constituent technologies in MOEMS, that is microoptics and micromechanics, have one important common feature: both technologies are compatible with integrated circuit technology and therefore allow batch processing. They can be produced in large quantity at low cost. This makes MOEMS highly attractive for commercial applications.

5.1.1 Silicon micromachining

The fabrication of microsystems is basically reduced to etching and bonding of silicon, as well as deposition steps. The driving idea in micromachining is to use photolithography, instead of conventional machine turning or milling.

Among the vast amount of different techniques and process steps, the technology silicon-on-insulator (SOI) is one possible choice. SOI-based MOEMS can give rise to several types of applications, like optical cross connects [82], variable optical attenuators [83] and accelerometers [84].

We describe now the different steps used in the process of fabrication of SOI-based MOEMS. A review of SOI technology is presented in reference [85]. The great advantage of this technology is its simplicity and small number of process steps. The central idea is the etching of a silicon layer, the device layer, which is on top of a silicondioxide layer (also called *sacrificial layer*). The silicon is structured in such a way that the removal of the sacrificial layer will disengage some designed frames, letting others fixed.

Figure 5.1 shows the various steps involved in the fabrication of SOI-based MOEMS. The process starts by performing photolithography on the SOI wafer in order to operate dry etching of the device layer. The patterning of the silicon is carried out by deep reactive ion etching (DRIE), which allows to fabricate vertical structures with a high aspect ratio and a good surface roughness of the side walls. This is a crucial step that demands a lot of optimization. The SiO_2 layer serves as an etch stop for DRIE. This is necessary to ensure the structures to have the same height over the whole wafer. The release of the structures designed to be mobile is obtained by dissolving the sacrificial layer in fluoric acid (HF wet etching). A final metallisation step is carried out in order to increase the conductivity of the device surface and to enhance the reflectivity of the mirrors. Note that besides the use of the silicondioxide layer as an etch stop for DRIE and as a sacrificial layer, it also serves as insulator between the different electrodes of the final device.

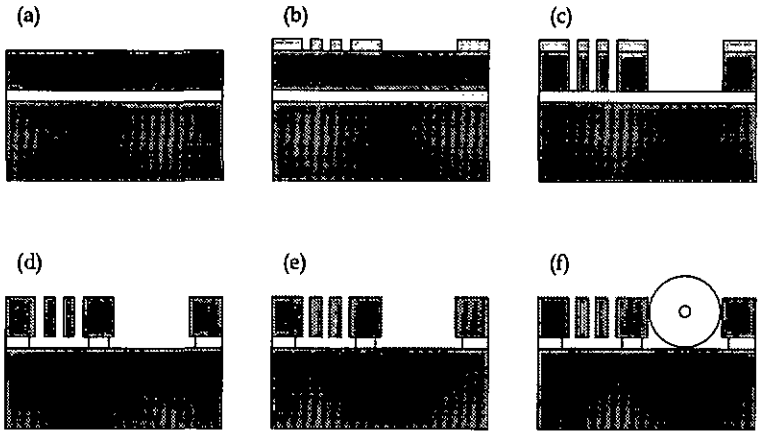

Figure 5.1: SOI technology: (a) SOI wafer composed of a silicon substrate wafer (the height is not relevant), a buried silicondioxide (SiO_2) layer (2 μm height) and a silicon device layer (75 μm height, in our case). (b) Deposition of a photoresist layer and photolithography. (c) Patterning of the wafer by deep reactive ion etching (DRIE). (d) Wet etching of the sacrificial layer with HF. (e) Metallisation. (f) Assembly.

An obvious asset of SOI technology resides in the patterning of dedicated structures aimed to facilitate the precise assembly of optical elements like fibers, micro-ball lenses or micro-plates (e.g. beamsplitter).

5.2 Actuation

As mentioned above, the motion of the mobile mirror used in the Michelson interferometer is realized by mean of an electrostatic comb drive actuator. These types of actuators are widely used in MEMS because of their simple construction and reliable operation. They allow to get a considerable displacement up to 100 μm, but they cannot drive large loads [86]. Therefore applications are mainly found in the area of optics where no output force is needed [86].

A photograph of the actuator together with the mobile mirror designed for the Michelson interferometer is shown in Fig. 5.2. The actuator is composed of a series of comb electrodes and springs. The actuation is driven by applying a voltage between the combs, as shown in Fig. 5.3. Two opposite comb structures are electrically insulated. One of them is fixed, whereas the other is mechanically connected to the suspension spring and the mirror structure. The suspension beams visible in both Figs. 5.2 and 5.3 act as springs, which counterbalance the electrostatic force applied between the combs.

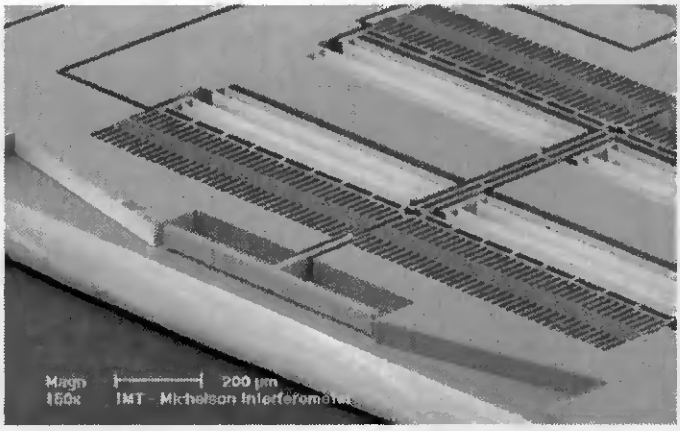

Figure 5.2: Scanning electron microscopy photograph of the electrostatic actuator, showing the 75 μm x 500 μm movable mirror, the electrostatic comb actuator and the suspension beams.

5.2.1 Design considerations

In some optical applications, like with a Michelson interferometer, one would like to have a displacement which is linear with the applied voltage. Since a conventional comb drive actuator has a voltage-displacement response that is quadratic, one has to conceive an appropriate design.

The displacement x as a function of the applied voltage V_0 for a conventional comb actuator is given by

$$x = \frac{1}{k}\varepsilon_0 n \frac{h}{g} V_0^2, \tag{5.1}$$

where k is the spring constant of the suspension beams, h is the height of the comb fingers, g is the gap between the comb fingers, n is the number of comb fingers on the mobile comb and ε_0 is the electric permittivity. In order to realize a linear motion, a push-pull configuration has been chosen: two identical comb actuators (A and B in Fig. 5.3) are placed opposite to each other. In this case, (Eq. 5.1) becomes

$$x = \frac{1}{k}\varepsilon_0 n \frac{h}{g}\left[(V_A - V_0)^2 - (V_B - V_0)^2\right]. \tag{5.2}$$

When the bias voltage V_A on comb A is kept constant and is exactly the opposite of V_B ($V_A = -V_B$), all quadratic terms are cancelled: and the displacement becomes

$$x = \frac{1}{k}\varepsilon_0 n \frac{h}{g} 2 V_A V_0. \tag{5.3}$$

The resulting displacement is now a linear function of the voltage applied on the mobile combs. The maximum displacement of the electrostatic comb drive actuators is limited

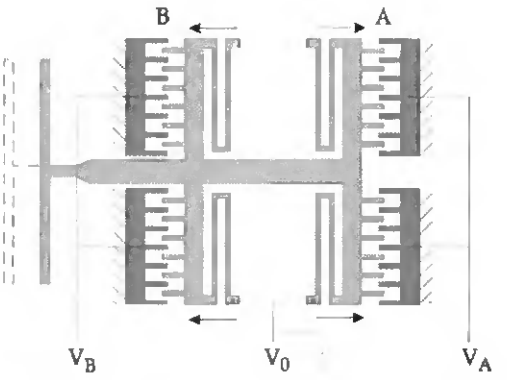

Figure 5.3: Schematic drawing of the actuator. This push-pull arrangement of the comb electrodes provides a linear displacement-voltage response.

by the lateral stability of the combs [87]. With a proper design, a maximum displacement x_{max} of 80 μm can be achieved, which gives a maximum optical path difference δ_{max} of 160 μm. For such a displacement the spectroscopic resolution at 633 nm is estimated to be $\Delta\lambda = \lambda^2/\delta_{max} \approx 2.5$ nm.

Optical elements

The complete silicon chip, comprising the actuator and the two mirrors, has a hole through the wafer to accommodate a beamsplitter or a beam splitting plate (120 μm thickness, coated with silver), as can be seen in Fig. 5.4. We can use either a beam splitting plate, or

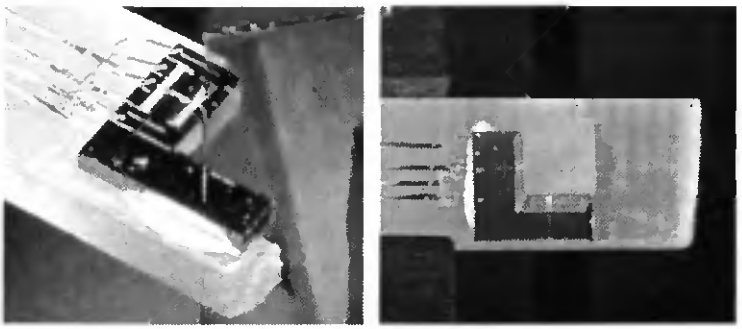

Figure 5.4: General view of the set-up. With a beam splitting plate (left), or with a cubic beamsplitter of 3 mm side (right).

a cubic beamsplitter. The beam splitting plate is adjustable and mounted on an external translation table. This configuration allows to set the zero path difference position. In the case of a cubic beamsplitter, this one is glued together with the chip onto a printed circuit board (PCB) support.

Both mirrors have a height of 75 μm and a length of 500 μm. They are coated with aluminum during the metallisation step. The surface roughness of the mirrors has been measured to be 36 nm rms, which corresponds to a light scattering of 6 %, and the verticality of the side walls is 89.3°. Further details can be found in the thesis dissertation by Marxer [88, p. 87, p. 102, p. 103].

5.3 Motion of the mirror

The characterization of the mobile mirror has been carried out by focusing a HeNe laser onto the mirrors. This solution has been chosen for practical reasons. The interference pattern resulting of such a configuration is a succession of concentric rings, as shown in Fig. 5.5. The detector has been placed in the central spot of the pattern and the

Figure 5.5: Photograph of the set up with the interference pattern.

modulation is recorded as a function of the displacement of the mirror. The divergence of the beam is mainly given by the numerical aperture of the focusing system, that is 0.2 rad.

Such a setup (see Fig. 5.6) can be used to find the zero path difference (ZPD) and to determine the maximum acceptance angle. Indeed, when the ZPD is zero the interference pattern of a monochromatic source is a simple spot instead of concentric rings. In addition,

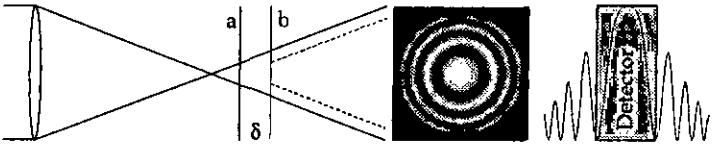

Figure 5.6: Configuration used to measure the motion of the mirror. The beam is about focused onto the two mirrors (a and b). The resulting interference pattern is illustrated in the center. On the right is sketched the position of the detector with respect to the interference pattern.

at the optical path maximum δ_{max}, one can define the maximum acceptance angle as the angle corresponding to the first zero of the interference pattern. A calculation with a diverging Gaussian wave front shows that the maximum acceptance angle is 0.14 rad at a distance of 40 μm between the mirrors. Note that in this calculation, the splitting occurs at about 25 times the Rayleigh range z_R from the focus point, which corresponds to a radius w of the wave front of 60 μm (about the height of the mirror), and permits to consider the wavefront as about spherical. At this distance, the appearance of the interference pattern depends only on the path difference between the mirrors and on the divergence angle. The optical path in each branch of the interferometer is about 1.5 mm.

5.3.1 Preliminary measurements

Measurements have been carried out at moderate, medium and full performance of the actuator, corresponding to a voltage V_0 of ± 1 V, ± 5 V, and ± 10 V, respectively. The fixed voltage $V_A = -V_B$ in Fig. 5.3 was equal to 15 V.

Voltage range: -1 V < V_0 < 1 V

We were able to measure the mirror displacement by counting the number of fringes. Figure 5.7 shows an interferogram with about 11.9 fringes, corresponding to a δ_{max} of 7.53 μm (i.e. 3.76 μm mirror displacement), for a triangular signal of the applied voltage V_0. The arrows indicate where the mirror changed the scanning direction. The contrast is about 90%.

Voltage range: -5 V < V_0 < 5 V

The linearity and the reproducibility of the motion of the mirror has been measured by applying a voltage V_0 corresponding to about half of the potential displacement. Both scanning directions have been taken into account. The result is shown in Fig. 5.8. The maximum optical path difference δ_{max} is equal to 40 μm.

The accuracy of the peak given by the Fourier transform of the interferogram, calculated for several scans of the mirror in the same direction, is better than 1 nm. The measured resolution for a HeNe laser is 16 nm in the backward direction and 23 nm in the forward direction. In this particular case, the wavelength has been calibrated for the

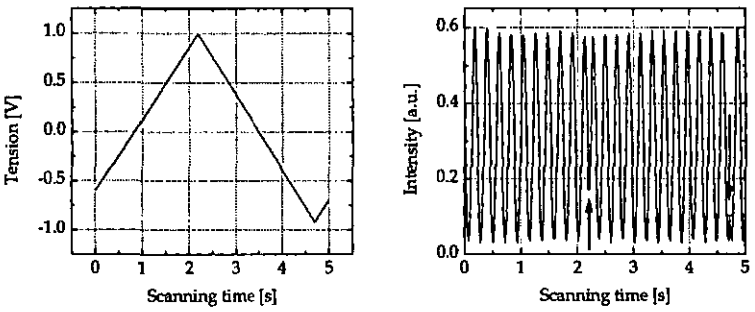

Figure 5.7: Detected signal versus the scanning time for HeNe laser light ($\lambda = 633$ nm). Triangular voltage V_0 applied to the comb.

backward direction. We have observed a discrepancy in the center of the peak calculating from the opposite direction (see Fig. 5.8). This means that the scanning speed is not exactly the same for both directions.

5.3.2 Drive non-linearity and hysteresis

The relatively large width of the peaks measured for both scanning directions, together with discrepancy in position of the center of the peaks observed in the previous results are probably caused by an hysteresis effect and a drive nonlinearity. This aspect will be treated in the following.

Voltage range: -10 V < V_0 < 10 V

At full performance we observed a drive nonlinearity, which gives a distortion of the path difference $\Delta(\delta)$ as great as ± 0.5 μm in both scanning directions. In addition, a difference between the two scan directions (hysteresis effect) is present. The maximum optical path difference δ_{max} achieved in this measurement was equal to 77 μm.

Figure 5.9 shows the drive nonlinearities $\Delta(\delta)$ with respect to the path difference δ. For both scanning directions, the reproducibility of the motion in the same direction is better than ± 25 nm. The observed nonlinearity can be understood by geometrical considerations. The reason is the change of the capacitance between the combs when the finger tips get close to the comb base [88, p. 92-93] (distance d Fig. 5.10).

To get rid of the effect of the drive nonlinearity we have applied a phase correction similar to the one given by Eq. (4.1) in section 4.2.3 namely

$$B_m = \sum_{n=1}^{N} F_n \exp[i2\pi m(\delta_n - \Delta(\delta_n))/N], \tag{5.4}$$

where $\Delta(\delta_n)$ are the measured nonlinearities, as shown in Fig. 5.9.

Figure 5.11 shows the spectrum of a HeNe laser before and after the phase correction.

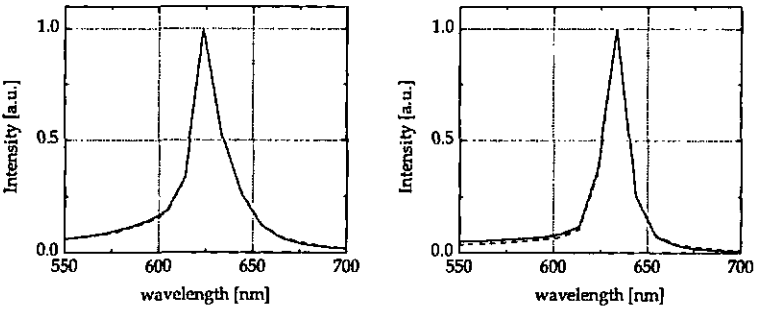

Figure 5.8: Two different spectra of a HeNe laser (plain and dashed lines) measured for both scanning directions of the mobile mirror. Left: Forward direction. The peaks are centered at 626 nm and have a FWHM equal to 23 nm. Right: Backward direction. The peaks are centered at 633 nm and have a FWHM equal to 16 nm.

After the correction, the resolution is 6 nm (at 633 nm), which is close to the theoretical limit of 5 nm for $\delta_{max} = 77$ μm. The same correction has been applied to other scans in the same direction, resulting in a resolution that was always better than 10 nm.

5.3.3 Broad band interferogram

With the specific configuration described above (see Fig. 5.4), we have managed to set the ZPD at about the middle of a scan. The resulting measurement of a luminescence diode at 800 nm is shown in Fig. 5.12. The poor contrast, about 5%, does not allow to process conveniently the corresponding spectrum. Indeed, the modulation is close to the dynamic range given by the acquisition card, which is 10 bit.

It is possible to distinguish the slight dispersion effect coming from the beam splitting plate of 120 μm thickness used in the experiment.

5.3.4 Scanning speed

With the setup used here, it is feasible to undertake about 250 measurements per second.

The limiting factor is neither the response time bandwidth of the detector (typically 1 MHz), nor the resonance frequency of such a device (estimated at about 1 kHz [88, p. 106]), but rather the digitalization capability of the acquisition card whose integration time is 10 μs, whatever the sampling frequencies.

Since the sampling rate has to be set in order to record the minimum accessible wavelength λ_{min} with respect of the Nyquist theorem, the maximum permitted scanning speed v_{max} is equal to

$$v_{max} = 0.5\frac{\lambda_{min}/2}{\tau_d}, \tag{5.5}$$

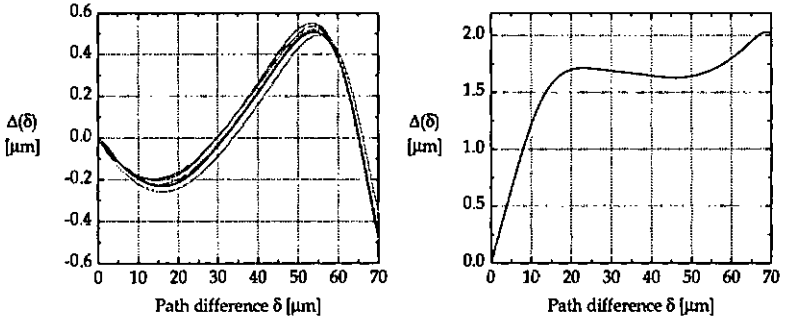

Figure 5.9: Nonlinearity of the mobile mirror. Results of the interferometric measurements for both scanning directions. Left: four different scans (grey lines) in the same direction. The deviation from their mean value (black line) is better ±25 nm.

Figure 5.10: Part of the comb-drive actuator.

where τ_d is the integration time of the acquisition card. With $\lambda_{min} = 380$ nm and $\tau_d = 10$ μs, v_{max} is equal to 9.5 mm/s. For a maximum optical path difference $\delta_{max} = 70$ μm, 3.7 ms are needed and, therefore, about 250 scans per second can be carried out. This is about 10 times more rapid than the CCD line used with the stationary Fourier transform spectrometer described in the previous chapter.

5.3.5 Conclusion

The feasibility of the device has been demonstrated by preliminary measurements with a HeNe laser. From the recorded interferograms it appears that the movable mirror has a drive nonlinearity of about 1.4 %. This inhomogeneity is not present at voltages $|V_0|$ smaller than 5 V. For larger voltages (as great as 10 V) a phase correction can be applied. This correction has been applied to other scans, yielding a resolution better than 10 nm at 633 nm for $\delta_{max} = 77$ μm. The repeatability of the motion of the mirror is better than ±25 nm.

In conclusion, it is conceivable to use this device for Fourier spectroscopy with similar specifications as those described in the previous chapters. The number of possible applications is considerable and the distinct advantages are the fabrication technology and the extreme compact dimensions.

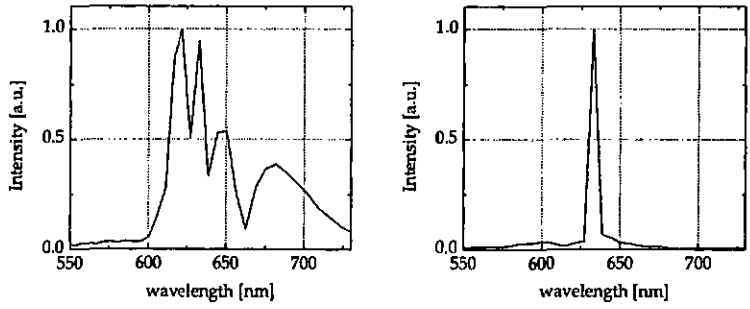

Figure 5.11: Spectrum of a HeNe laser without phase correction (left) and after phase correction (right), using $\Delta(\delta)$ of Fig. 5.9(left).

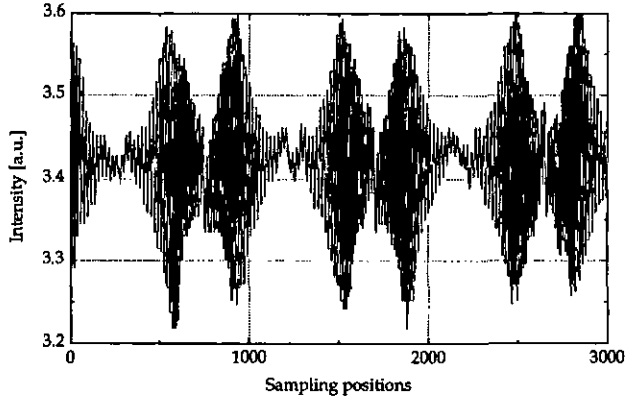

Figure 5.12: Interferogram of a luminescence diode measured over several scans.

5.4 Outlook

It turns out that the enormous potential of the technology presented in this chapter offers almost infinite possibilities. It is the aim of this section to give an overview of these vast resources.

We first introduce the successive steps and improvements, in terms of new designs, in connection with the Michelson interferometer which we have already realized, in particular the use of fibers to bring in and collimate the light to the chip. We propose a possible method to obtain microoptical elements that are suitable for integration on the interferometer chip. Finally, the versatility of this technology is illustrated with three other designs of spectrometers using radically different spectroscopic concepts.

5.4.1 Michelson interferometer: next designs

The primary purpose in this study was to realize a movable mirror that could serve in a Michelson interferometer. We demonstrated that a chip composed of a mirror driven by an SOI-based actuator was conceivable practically and that the motion of the mirror was suitable for Fourier spectroscopy with a resolution of 10 nm in the visible. Now, the logical follow-up is to find the way to integrate the elements that will transform the interferometer into a spectrometer.

To improve the device, in terms of fabrication, ease of handling and optical performance, efforts have been focused on the alignment of the optical elements, the length of the optical path and the online calibration of the movable mirror. We propose two types of designs. In the first one, emphasis is put on the collimation quality of the light source, while in the second design we privilege assembly ease and reduction of the optical distance from the input to the output of the interferometer. A scanning electron microscope (SEM) photograph of both types of system are shown in Fig. 5.13. A fiber permits to bring the light source very close to the interferometer. The distances from the source to the mirrors and from the mirrors to the output are short. The beam splitting plate is self adjusted. The actuator drives two identical mirrors opposite to each other. The collimation of the source is ensured by crossed cylindrical optical elements: two GRIN lenses placed after the input fiber and before the output fiber, and the curvature of the two mirrors.

The improved features are:

- As 'light source' serves a multimode fiber placed close to the interferometer and adjusted by mean of a U-grooves. Note that the fiber can be used either as a light source, or as a light collector. In one configuration, both the output and the input of the interferometer make use of fibers.

- The beam splitting plate is accommodated into a U-groove. Special attention has been paid to set the position of the zero path difference.

- The collimation of the light source is ensured by crossed cylindrical elements: a gradient-index cylindrical microlens (fiber) and cylindrical mirrors. The collimating fiber is placed at a distance of 31 μm from the input fiber and collimates the light diverging vertically to the surface of the chip. The two mirrors have both a curvature that collimates the light diverging horizontally.

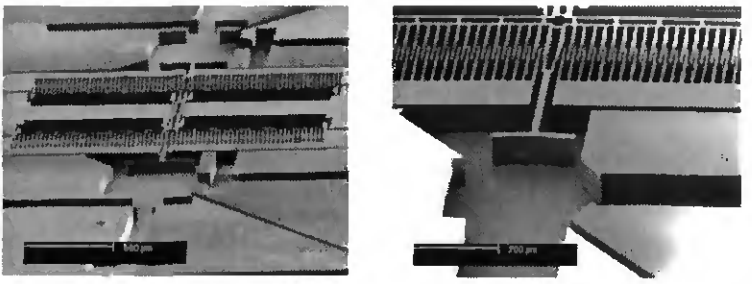

Figure 5.13: Improved Michelson interferometer.

- A second interferometer is integrated with the aim of online calibration. This is realized by placing two identical mirrors opposite to each other, which are driven by the same actuator. One interferometer records the interferogram generated by the light source of interest, while the other one measures a single line source.

Thanks to the dedicated U-grooves, the precision of the positioning of the optical elements is extremely accurate.

5.4.2 Optical elements

The combination of microoptics and micromechanics is not an easy task. Nowadays, microsystem fabrication has adapted and developed a diversity of technology, that are nevertheless not always compatible with each other. To find a method that is part of the existing fabrication process is difficult. Indeed, the more process steps are added, the more delicate the fabrication becomes. Therefore, hybrid systems, using more than one technology, might be the solution in some situations.

We propose a method to fabricate microoptical components like cylindrical lenses and beamsplitters, with the aim of designing an optical bench that will be bonded over the silicon chip with the actuated mirror. These individual optical elements have been realized by replication into UV-curing adhesive by means of an elastomer material [89]. The components have been first designed and etched in a silicon wafer by DRIE. Then, the elastomer is used to realize a negative mold. Finally, UV-curing is used to make the replicated copy. A beamsplitter and a cylindrical lens fabricated with this method are shown in Fig. 5.14. However, the process is not yet optimized. A drawback of this method is the relatively high amount of inhomogeneities, like bubbles, in the UV-curing. In addition, the maximum achievable aspect ratio of the structures is about equal to 1.

A different method, and probably more promising, can rise from the technology of thick resist, that permits the fabrication of transparent elements with a high aspect ratio (about 10) and vertical side walls.

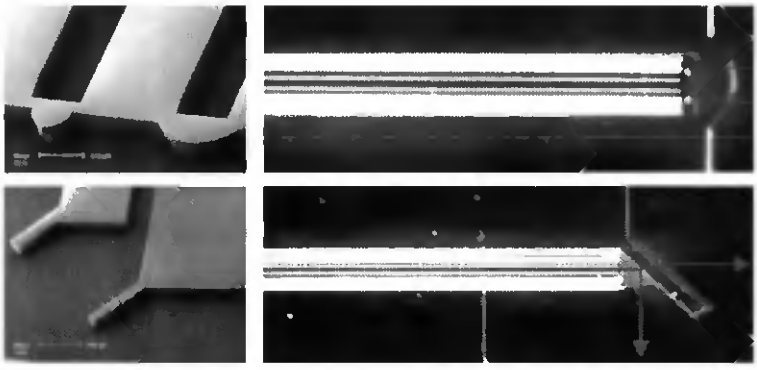

Figure 5.14: Left: Silicon structures (here, cylindrical lenses with U-grooves for input fiber, as well as beam splitting plate) used for replication in UV glue. Right: Same structures replicated into UV-curing adhesive.

5.4.3 Other Optical MEMS

As an outlook, we show three different designs of devices illustrating the flexibility and adaptability of SOI-based technology. Note that none of these devices have been characterized so far.

Lamellar grating interferometer

A lamellar grating interferometer is a grating that operates in the zeroth order. This particular type of apparatus was invented by Strong [90]. A scheme of the principles is illustrated in Fig. 5.15. For a detailed description of this method, we refer to chapter 15

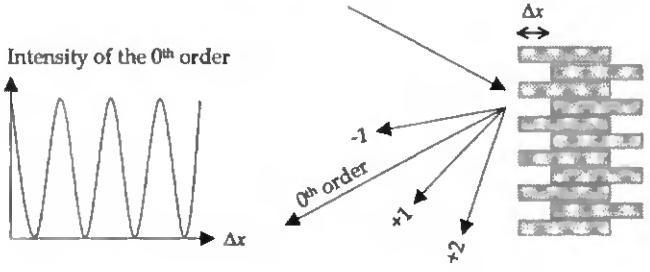

Figure 5.15: Principles of a lamellar grating interferometer. The modulation of the zeroth order is recorded in function of the depth Δx introduced in the grating.

of reference [4].

This type of spectrometer is mainly used for wavelengths larger than 100 μm; below, the tolerances are too tight for most machine shops. Silicon micromachining is the ideal technology to overcome these limitations for shorter wavelengths.

The advantages of this technique are the lack of a beamsplitter and the high efficiency. In principle, the total amount of incoming light is usable. The Michelson interferometer splits wave amplitudes at the beam splitter. On the contrary, the lamellar grating spectrometer divides the wavefront by a set of movable facets. The variation of the grating depth creates the optical path difference. The basic equation for Fourier transform spectroscopy applies to the lamellar grating interferometer, as well as the Michelson interferometer.

Figure 5.16 shows an SEM photograph of the lamellar grating that has been realized.

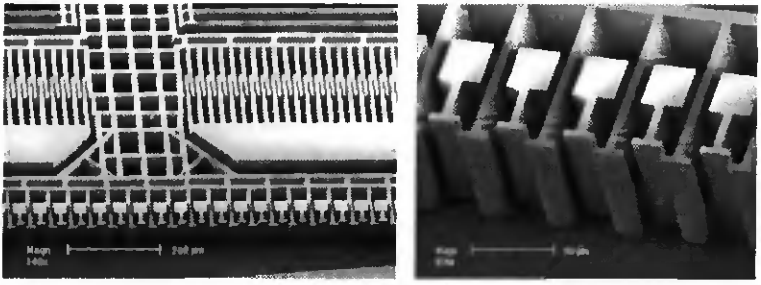

Figure 5.16: SEM photograph of the lamellar grating device.

The grating period is 40 μm.

Hadamard transformer

Hadamard transform spectrometers have been developed in order to enhance the signal-to-noise ratio of dispersion-based spectrometer [91]. The basic Hadamard transform instrument consists of an encoding mask and a dispersing system (a prism or a grating) which separates different frequency components of an incident beam. The principle in this technique is the use of masks (or array of slits) which either block or transmit light. These masks are constructed from matrices named after the French mathematician Hadamard. The detected signal needs to be processed via a dedicated mathematical transformation. An array of commutable slits is shown in Fig. 5.17.

Curved diffraction grating spectrometer

The last approach consists of a grating fabricated on a curved surface attached to the end of a movable mechanical beam as shown in Fig. 5.18. An input fiber, acting as a light source, brings the light onto the curved grating which disperses the light into a second fiber. We use the first order of a blazed grating. The fact that the minimum and maximum accessible wavelength ($\lambda = 400$ nm and $\lambda = 800$ nm) have to be dispersed along a distance

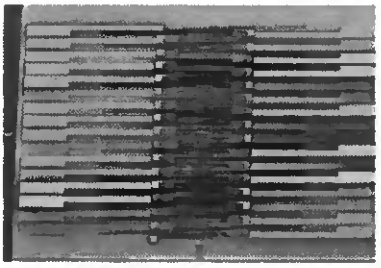

Figure 5.17: SEM photograph of a line of commutable slits.

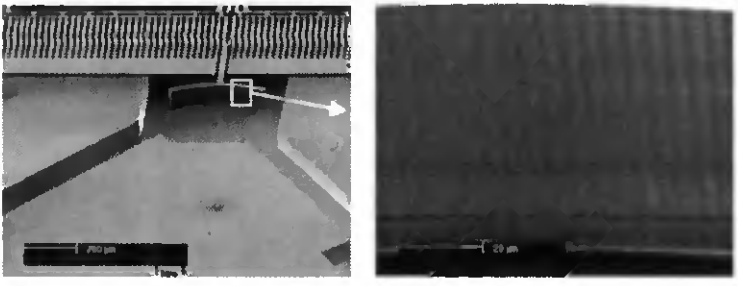

Figure 5.18: SEM photograph of a grating placed on a curved mirror driven by an actuator.

corresponding to the maximum displacement of the mirror (about 50 μm), together with the fact that the mean diffracted angle has to be 45°, leads to an incident angle of 36° and a grating period of 5 μm. Both the source and collecting fibers have been designed on the Rowland circle, which has a radius of 220 μm. The curvature of the grating has a radius of 440 μm.

The technological limitation concerns the patterning of the diffraction grating. The definition of the mask and the photolithography have to be very accurate. In addition the transfer into silicon via DRIE is a critical step. In fact, it is difficult to maintain the ideal blazed shape of the grating along the full height of the device layer. Figure 5.18 shows that the shape of the grating has been smoothed by the fabrication process.

Chapter 6

Conclusions

In this work, the relevance of the Fourier transform technique for a number of applications that demand the utilization of portable and compact devices has been clearly identified. It has been shown that miniature Fourier spectrometers have a great potential compared with common portable devices based on dispersive methods.

However, it has also been shown that the well-known advantage of Fourier transform spectroscopy (the throughput and multiplex advantage) does not necessarily apply to miniature Fourier spectrometers. On the other hand, when compared to gratings, Fourier spectrometers are never limited by the presence of the second order diffraction. The limiting aspect comes mainly from the realization of the devices.

Stationary Fourier transform spectrometer

We have presented a dispersive spatially modulated Fourier transform spectrometer based on a Michelson interferometer. A non-standard beam splitting configuration has lead to compactness and reduced demands concerning spatial coherence. Combined with a cylindrical lens, these features enhance the throughput. Measurements have shown that this type of spectrometer is well suited for applications in the visible wavelength range, which do not need high resolution, but require a good stray light suppression.

From the point of view of the performance, this Fourier spectrometer satisfies the following requirements, typical for portable spectroscopic devices:

- Resolution: $\Delta\lambda = 10$ nm,
- Wavelength range: 380 nm $< \lambda <$ 730 nm,
- Wavelength accuracy: < 0.5 nm,
- Straylight suppression: $SU > 20$ dB,
- Colour separation: $\Delta E < 1$,
- Contrast: $C > 50\%$.

To achieve these specifications, signal processing is crucial. It has been seen that fixed pattern noise is the greatest source of trouble and the background intensity distribution

should always be removed in order to reach the best performance. If this is not possible, apodization and cutting down the number of used pixels can help, but only for symmetrical configurations. Of course, the results vary as a function of the amount and type of inhomogeneities in the background.

The realization of this spectrometer is limited by assembly tolerances, which makes it difficult to compete with grating-based solutions.

Time-scanning Michelson interferometer based on silicon micromachining

The feasibility of this novel device has been demonstrated by preliminary measurements with a HeNe laser. From the recorded interferograms it appears that the movable mirror has a drive nonlinearity of about 1.4 % for a displacement of $\delta_{max} = 70\mu m$ at 10 V drive voltage. For a displacement limited to $\delta_{max} = 35\mu m$ (voltage of 5 V), the movement is very close to linear. A phase correction algorithm can be applied. With this correction a resolution better than 10 nm at 633 nm was obtained since the repeatability of the motion of the mirror is better than ± 25 nm for an optical path difference $\delta_{max} = 70\mu m$. It results that it is conceivable to use this device for Fourier spectroscopy with similar specifications as those described for the stationary configuration. The number of possible applications is considerable and the distinct advantages are the fabrication technology and the extreme compact dimensions.

The vast resources offered by SOI-technology have been illustrated. We have introduced an improved design of the existing Michelson interferometer, with the aim of undertaking spectroscopic measurements. In addition, we have shown three different designs of devices illustrating the flexibility and adaptability of SOI-based technology: a lamellar grating interferometer, an array of commutable slits to realize a Hadamard transformer and a movable curved diffraction grating. Finally, we propose a possible method to obtain microoptical elements that are suitable for integration in the interferometer chip.

Appendix A

Elements of statistical optics

This section is a summary from reference [12, pp. 11–17, and 60–76].

A.1 Random variables

A.1.1 Density functions

Let U be a continuous random variable and u a possible real number associated to the random variable. The probability that U assumes a given value can be expressed in terms of the *probability density function* $p_U(u)$. For instance, the Gaussian density is one specific probability density function.

Now consider two random variables U and V, the *marginal probability density functions* of U and V are defined as

$$\begin{aligned} p_U(u) &= \int_{-\infty}^{\infty} p_{UV}(u,v)\mathrm{d}v \\ p_V(v) &= \int_{-\infty}^{\infty} p_{UV}(u,v)\mathrm{d}u, \end{aligned} \tag{A.1}$$

where $p_{UV}(u,v)$ is the *probability density function* for the joint random variables UV. $p_{UV}(u,v)$ must have unit volume (normalization), that is

$$\iint_{-\infty}^{\infty} p_{UV}(u,v)\mathrm{d}u\mathrm{d}v = 1. \tag{A.2}$$

A.1.2 Statistical averages

Let g be a function that for every real number u assigns a new real number $g(u)$. We define the *statistical average* (or expected value) of $g(u)$ by

$$< g(u) >_E = \bar{g}(u) = \int_{-\infty}^{\infty} g(u)p_U(u)\mathrm{d}u. \tag{A.3}$$

By setting $g(u) = u^n$, we obtain the n th-order *moments*. The first moment ($g(u) = u$) is the *mean value*, defined by

$$\bar{u} = \int_{-\infty}^{\infty} up_U(u)\mathrm{d}u \tag{A.4}$$

and the second order ($g(u) = u^2$) is the *mean-square value*, defined by

$$\bar{u^2} = \int_{-\infty}^{\infty} u^2 p_U(u) \mathrm{d}u. \tag{A.5}$$

By setting $g(u) = (u - \bar{u})^n$, we obtain the *central moments*, which represent the fluctuations of a random variable about its mean. The second central moment is the *variance*, defined by

$$\sigma^2 = \int_{-\infty}^{\infty} (u - \bar{u})^2 p_U(u) \mathrm{d}u. \tag{A.6}$$

With two random variables U and V, the *joint moments* of U and V are defined by

$$<u^n v^m> = \iint_{-\infty}^{\infty} u^n v^m p_{UV}(u, v) \mathrm{d}u\mathrm{d}v. \tag{A.7}$$

The *correlation* of U and V is

$$\Gamma_{UV} = <uv> = \iint_{-\infty}^{\infty} uv p_{UV}(u, v) \mathrm{d}u\mathrm{d}v, \tag{A.8}$$

the *covariance* of U and V is

$$C_{UV} = <(u - \bar{u})(v - \bar{v})> = \Gamma_{UV} - \bar{u}\bar{v} \tag{A.9}$$

and the *correlation coefficient* is

$$\rho = \frac{C_{UV}}{\sigma_U \sigma_V}. \tag{A.10}$$

The correlation coefficient is a direct measure of the similarity of the fluctuations of U and V. Using the Schwarz's inequality we can show that $0 \leq |\rho| \leq 1$. If $|\rho| = 1$, we say that U and V are perfectly correlated, meaning that their fluctuations are identical, and when $|\rho| = 0$, we say that U and V are uncorrelated. Two statistically independent random variables are always uncorrelated and

$$p_{UV}(u, v) = p_U(u) p_V(v) \;\Rightarrow\; <uv> = <u><v>. \tag{A.11}$$

However, zero correlation does not necessarily imply statistical independence.

A.2 Random processes

A natural generalization of the concept of a random variable is a random process, for which the random events are functions rather than numbers. We consider here only functions with a dependence on time.[1]

Let $U(t)$ be a random process and $u(t)$ the specific sample function contained in the random process U (the waveforms $u^{(1)}(t)$, $u^{(2)}(t)$, ..., $u^{(k)}(t)$, ..., are the members of the ensemble). As illustrated in Fig. A.1 $u_1 = u(t_1)$ and $u_2 = u(t_2)$ are two random values of the function $u(t)$. The *joint probability density function* of the random variables $U(t_1)$ and $U(t_2)$ is denoted $p_U(u_1, u_2; t_1, t_2)$.

[1] Generalizations to functions of space (study of spatial coherence) are straightforward.

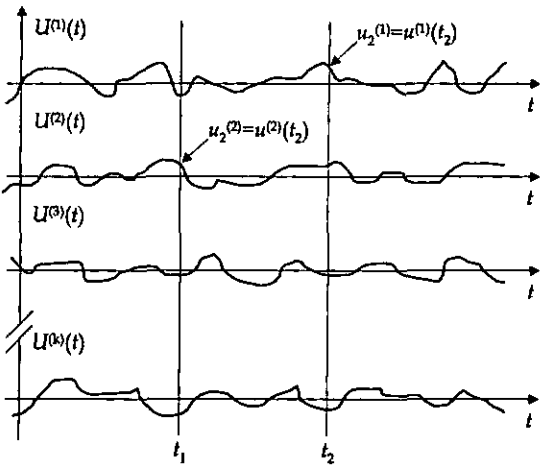

Figure A.1: An ensemble of sample functions, where t_1 and t_2 are the parameters values for which the joint probability density function $p_U(u_1, u_2; t_1, t_2)$ is specified.

A.2.1 Stationarity

A random process is called *stationary* if the n th-order joint probability density function $p_U(u_1, u_2, \ldots, u_n; t_1, t_2, \ldots, t_n)$ is independent of the choice of time origin, that is, for the first-order density function

$$p_U(u; t) = p_U(u) \tag{A.12}$$

and, for the second-order density function

$$p_U(u_1, u_2; t_1, t_2) = p_U(u_1, u_2; \tau), \tag{A.13}$$

where $\tau = t_2 - t_1$. The stationarity implies that the *ensemble average* of a function $g(u)$ (defined in Eq. (A.3) for functions of numbers)

$$< g(u) >_E = \int_{-\infty}^{\infty} g(u) p_U(u) \mathrm{d}u, \tag{A.14}$$

is independent of the time.

A stationary random process is called *ergodic* when the *time average* of a function g of a sample function $u(t)$,

$$< g(u(t)) >_t = \lim_{T \to \infty} \frac{1}{2T} \int_{-T}^{T} g(u(t)) \mathrm{d}t \tag{A.15}$$

is equal to the ensemble average: $< g >_E = < g >_t$.

A.2.2 Autocorrelation function

In the same manner than with random variables (Eq. (A.8)), we can define, for a stationary process $U(t)$, the *time autocorrelation function* of a single known time function $u(t)$ ($u(t)$ may be one sample function of a random process):

$$\Gamma_U(\tau) = <u(t+\tau)u(t)> = \iint_{-\infty}^{\infty} u_1 u_2 p_U(u_1, u_2; \tau) \mathrm{d}u_1 \mathrm{d}u_2. \tag{A.16}$$

From the physical point of view, $\Gamma_U(\tau)$ measures the structural similarity of $u(t)$ and $u(t+\tau)$, averaged over all time. For ergodic random processes, $\Gamma_U(\tau)$ of all functions are equal.

Three important properties of autocorrelation functions of stationary processes are:

1. $\Gamma_U(0) = \bar{u^2}$,
2. $\Gamma_U(-\tau) = \Gamma_U(\tau)$,
3. $|\Gamma_U(\tau)| \leq \Gamma_U(0)$.

A.3 Spectral analysis of random processes

In spectral analysis of random processes it is important to make the distinction between the two following quantities: the spectral densities of *known functions* of time and of a *random process* containing an entire ensemble of different functions. The first class of function leads to the *energy* spectral density and the latter to the *power* spectral density.

A.3.1 Spectral density of known functions

Let $u(t)$ be a known function of time.

If $u(t)$ is *Fourier transformable*, that is

$$\int_{-\infty}^{\infty} |u(t)| \mathrm{d}t < \infty, \tag{A.17}$$

then, its Fourier transform

$$\hat{u}(\nu) = \int_{-\infty}^{\infty} u(t) \exp[i2\pi\nu t] \mathrm{d}t \tag{A.18}$$

always exists and the area under $|\hat{u}(\nu)|^2$ is equal to the total energy contained in $u(t)$, according to the Parceval's theorem:

$$\int_{-\infty}^{\infty} u^2(t) \mathrm{d}t = \int_{-\infty}^{\infty} \underbrace{|\hat{u}(\nu)|^2}_{E(\nu)} \mathrm{d}\nu. \tag{A.19}$$

The quantity

$$E(\nu) = |\hat{u}(\nu)|^2 \tag{A.20}$$

is the energy spectral density of $u(t)$ and has the dimensions of energy per unit frequency.

If $u(t)$ is not Fourier transformable, but has a finite *average power*

$$\lim_{T\to\infty} \frac{1}{2T} \int_{-T}^{T} u^2(t)\mathrm{d}t < \infty, \tag{A.21}$$

then, in general, the Fourier transform of $u(t)$ does not exist. However, the truncated function

$$u_T(t) = \mathrm{rect}(T,t)u(t), \tag{A.22}$$

where $\mathrm{rect}(T,t)$ is defined to be equal to 1 for $-T \leq t \leq T$ and zero otherwise, does have a Fourier transform

$$\hat{u}_T(\nu) = \int_{-\infty}^{\infty} u_T(t) \exp[i2\pi\nu t]\mathrm{d}t \tag{A.23}$$

and the quantity $|\hat{u}_T(\nu)|^2$ represents the distribution of energy. This leads to the definition of the power spectral density

$$B(\nu) = \lim_{T\to\infty} \frac{|\hat{u}_T(\nu)|^2}{2T}, \tag{A.24}$$

which has the dimension of power per unit frequency.

A.3.2 Spectral density of random processes

Similarly, let $U(t)$ be a random process containing a set of single functions being Fourier transformable or having a finite average power. Since we wish to find an energy spectral distribution, or a power spectral distribution that characterize $U(t)$, it is logical to define such quantities in terms of averages over the entire random process (i.e. over the whole ensemble), defined by

$$E_U(\nu) = <|\hat{u}(\nu)|^2>_E \tag{A.25}$$

and

$$B_U(\nu) = \lim_{T\to\infty} \frac{<|\hat{u}_T(\nu)|^2>_E}{2T}. \tag{A.26}$$

Let the random process $V(t)$ consist of sample functions that result from passing all sample functions of the random process $U(t)$ through a known linear filter having a response $h(t)$ as illustrated in Fig.A.2 . Then, $V(t)$ is called a *linearly filtered* random process. The energy spectral density $E_V(\nu)$ and the power spectral density $B_V(\nu)$ are related to their respective input spectral densities $E_U(\nu)$ and $B_U(\nu)$ by

$$E_V(\nu) = |\hat{h}(\nu)|^2 E_U(\nu), \tag{A.27}$$

$$B_V(\nu) = |\hat{h}(\nu)|^2 B_U(\nu). \tag{A.28}$$

A.4 The Wiener-Kintchine theorem

The concept of time autocorrelation functions $\Gamma(\tau)$, introduced in section A.2.2, plays a great role in the theory of coherence. A major practical importance of autocorrelation

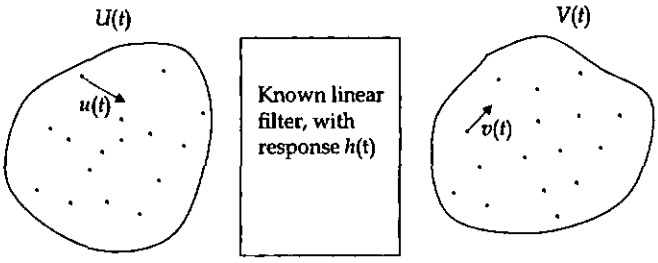

Figure A.2: Spectral densities for linearly filtered random processes.

functions lies in the very special relationship they enjoy with respect to the power spectral density. In a stationary random process, the autocorrelation function and power spectral density form a Fourier transform pair

$$\begin{aligned} B_U(\nu) &= \int_{-\infty}^{\infty} \Gamma_U(\tau) \exp[i2\pi\nu\tau] \mathrm{d}\tau, \\ \Gamma_U(\tau) &= \int_{-\infty}^{\infty} B_U(\nu) \exp[-i2\pi\nu\tau] \mathrm{d}\nu. \end{aligned} \tag{A.29}$$

This very special relationship is known as the *Wiener-Kintchine theorem.*

A.4.1 Proof

To prove this theorem, we begin with the definition of the power spectral density given by Eq. (A.26) and replace the Fourier transform $\hat{u}_T(\nu)$ given by Eq. (A.23):

$$B_U(\nu) = \lim_{T\to\infty} \left\{ \frac{1}{2T} < \left| \int_{-\infty}^{\infty} u_T(t) \exp[i2\pi\nu t] \mathrm{d}t \right|^2 >_E \right\}. \tag{A.30}$$

Using the definition of $u_T(t)$ (Eq. (A.22)) and the definition of the square modulus $|u|^2 = uu^*$, the ensemble average in Eq. (A.30) can be written

$$\begin{aligned} <\ldots>_E &= < \int_{-\infty}^{\infty} \mathrm{rect}(T,t) u(t) \exp[i2\pi\nu t] \mathrm{d}t \int_{-\infty}^{\infty} \mathrm{rect}(T,t') u^*(t') \exp[-i2\pi\nu t'] \mathrm{d}t' >_E \\ &= \iint_{-\infty}^{\infty} \mathrm{rect}(T,t)\mathrm{rect}(T,t') <u(t)u^*(t')>_E \exp[i2\pi\nu(t-t')] \mathrm{d}t\mathrm{d}t' \end{aligned}$$

and, replacing t' by $t-\tau$,

$$\begin{aligned} &= \iint_{-\infty}^{\infty} \mathrm{rect}(T,t)\mathrm{rect}(T,t-\tau) \underbrace{<u(t)u^*(t-\tau)>_E}_{\Gamma(\tau)} \exp[i2\pi\nu\tau] \mathrm{d}\tau\mathrm{d}t \\ &= \int_{-\infty}^{\infty} \Gamma(\tau) \exp[i2\pi\nu\tau] \mathrm{d}\tau \int_{-\infty}^{\infty} \mathrm{rect}(T,t)\mathrm{rect}(T,t-\tau) \mathrm{d}t. \end{aligned}$$

Now, if we apply the limit in Eq. (A.30), only the second integral here above is concerned and, for any fixed τ

$$\lim_{T\to\infty} \frac{1}{2T} \int_{-\infty}^{\infty} \mathrm{rect}(T,t)\mathrm{rect}(T,t-\tau)\mathrm{d}t = 1.$$

Finally, Eq. (A.30) becomes

$$B_U(\nu) = \int_{-\infty}^{\infty} \Gamma_U(\tau) \exp[i2\pi\nu\tau]\mathrm{d}\tau.$$

The inverse relationship follows from the properties of Fourier transforms.

Appendix B

Elements of radiometry

We define here the terms occurring when a signal is detected with an interferometer. Indeed, confusion is often made when using the notions of intensity, energy, power, etc. We shall be concerned both with the total quantity of radiation and, since we are determining spectra, with the quantity of radiation lying in a given spectral interval. The following definitions are given from reference [7, p. 92].

The International System of Units are given in [m, kg, s, A].

Radiant flux [W]=[J/s]
Total quantity of radiation in a signal, measured in power units or in terms of rate of energy flow.

Spectral flux [W/Hz], or [W/m^{-1}]
Flux of a particular frequency lying in the small interval ν to $\nu + d\nu$ or, if wavenumber is the variable, σ to $\sigma + d\sigma$.

Radiant flux density [W/m^2]
Amount of flux flowing through unit area placed perpendicular to the direction of flow.

Spectral radiant flux density [$W/(Hz \cdot m^2)$], or [$W/(m^{-1} \cdot m^2)$]=[W/m]

Intensity [W/m^2]
Time-averaged value of the radiant flux density.

Radiance [$W/(m^2 \cdot sr)$]
Amount of flux emitted by the unit area into unit solid angle.

Spectral radiance [$W/(Hz \cdot m^2 \cdot sr)$], [$W/(m \cdot sr)$]
Amount of flux emitted per unit bandwidth by unit area of the source into unit solid angle.

Étendue [m^2 sr]
Following the previous definitions, one can define the *throughput* or *étendue* of an inter-

ferometer as

$$E = \Omega_s A_s = \Omega_d A_d, \tag{B.1}$$

which is the capacity of the system to transmit energy. This notion is illustrated in Fig. B.1. In practice, as a source is diverging and as the noise increases with the sensitive

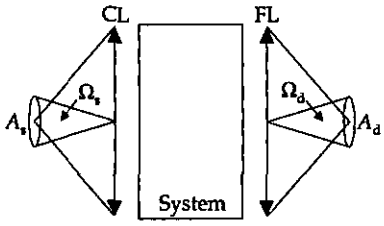

Figure B.1: Étendue of a system. The entrance aperture of area A_s and the detector of area A_d, subtend the solid angles Ω_s and Ω_d at the collimating lens (collimator), respectively the focusing lens (condensor).

area of the detector, the common configuration for a scanning Michelson interferometer consists in the use of a collimator and a condensor (see Fig. B.1). The first lens gathers the light diverging from the source, the second lens focuses the light onto the smallest possible surface.

In a measurement, one records power (not intensity or energy) and from this detected signal one determines the distribution of the radiated power over the observed frequency range, i.e. the *spectral flux*, or *power spectral density*, or *power spectrum*.

The spectral power collected by the collimator is [7, p. 95]

$$L(\nu) = l(\nu)E \quad [\mathrm{W/Hz}], \tag{B.2}$$

where $l(\nu)$ is the spectral radiance of a source element.

Appendix C

Filter GG495

Figures C.1 and C.2 show the transmission and suppression spectra of a filter GG495 measured with a spectrometer Perkin Elmer UV/VIS/NIR Lambda900.

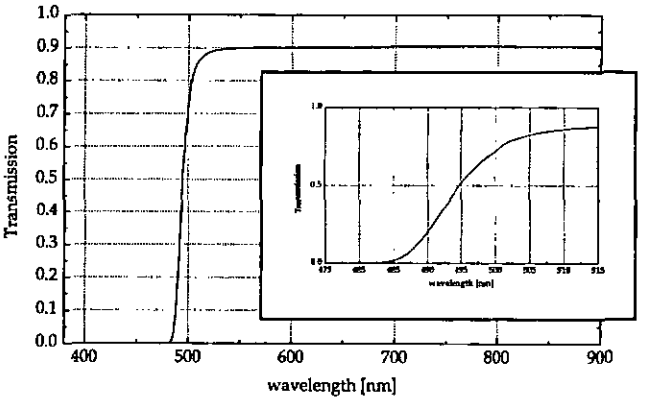

Figure C.1: Transmission spectrum of a filter GG495.

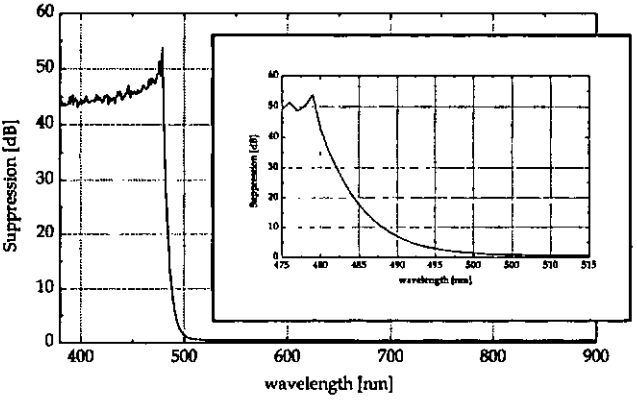

Figure C.2: Suppression spectrum of a filter GG495.

Bibliography

[1] J. Connes. Recherches sur la spectroscopie par transformation de fourier. *Revue d'Optique*, 40(2-5):45–79, 116–140, 171–190, 231–265, 1961.

[2] L. Mertz. *Transformation in optics.* John Wiley and sons, New York, 1965.

[3] G. A. Vanasse and H. Sakai. Fourier spectroscopy. In E. Wolf, editor, *Progress in Optics*, volume 6, pages 259–330. 1967.

[4] R. J. Bell. *Introductory Fourier transform spectroscopy.* Academic Press, New York and London, 1972.

[5] A. P. Thorne. *Spectrophysics.* Chapman and Hall, London, 1974.

[6] R. Geick. Infrared fourier transform spectroscopy. In *Topics in Current Chemistry*, volume 58. Springer-Verlag, Berlin, 1975.

[7] J. E. Chamberlain. *The principles of interferometric spectroscopy.* John Wiley and Sons, Chichester, 1979.

[8] A. E. Martin. *Infrared interferometric spectrometers.* Elsevier Scientific, Amsterdam, 1980.

[9] P. Hariharan. *Optical interferometry.* Academic Press, Sidney, 1985.

[10] P. Jacquinot. *Rep. Progr. Phys.*, 23:267, 1960.

[11] P. B. Fellgett. *J. Phys. Radium*, 19:187, 1958.

[12] J. W. Goodman. *Statistical optics.* John Wiley and Sons, New York, 1985.

[13] F. S. Crawford. *Ondes.* Armand Colin, Paris, 1972.

[14] E. V. Loewenstein. The history and current status of fourier transform spectroscopy. *Appl. Opt.*, 5(5):845–854, 1966.

[15] M. L. Forman, W. H. Steel, and G. A. Vanasse. Correction of asymmetric interferograms obtained in fourier spectroscopy. *J. Opt. Soc. Am.*, 56(1):59–63, 1966.

[16] J. W. Brault. High precision fourier transform spectrometry: the critical role of phase corrections. *Mikrochim. Acta*, III:215–227, 1987.

[17] T. P. Sheahen. Chirped fourier spectroscopy. 1:dynamic range improvement and phase correction. *Appl. Opt.*, 13(12):2907–2912, 1974.

[18] T. P. Sheahen and T. O. McCanney. Phase discrepancies in asymmetric interferograms and application to nonlinearities in fourier spectroscopy. *J. Opt. Soc. Am.*, 65(7):825–828, 1975.

[19] B. Carli, F. Forni, and F. Mencaraglia. Phase error correction in ft spectroscopy of spectra with positive and negative intensities. *Intern. J. Infrar. Millim. Waves*, 3(4):529–540, 1982.

[20] R. C. M. Learner, A. P. Thorne, I. Wynne-Jones, J. W. Brault, and M. C. Abrams. Phase correction of emission line fourier transform spectra. *J. Opt. Soc. Am. A*, 12(10):2165–2171, 1995.

[21] P. Raspollini, P. Ade, B. Carli, and M. Ridolfi. Correction of instrument line-shape distortions in fourier transform spectrosopy. *Appl. Opt.*, 37(17):3697–3704, 1998.

[22] A. S. Zachor. Drive nonlinearities: their effects in fourier spectroscopy. *Appl. Opt.*, 16(5):1412–1424, 1977.

[23] J. Kauppinen, T. Krkkinen, and E. Kyr. Correcting errors in the optical path difference in fourier spectroscopy: a new accurate method. *Appl. Opt.*, 17(10):1587–1594, 1978.

[24] G. Guelachvili. Distortions in fourier spectra and diagnosis. In G. A. Vanasse, editor, *Spectrometric techniques*, volume 2. Academic Press, London, 1981.

[25] C. E. Shannon. Communication in the presence of noise. In *Proc. IRE*, 1949.

[26] R. Bracewell. *The Fourier transform and its applications*. McGraw-Hill, New York, 1965.

[27] R. H. Norton and R. Beer. New apodizing functions for fourier spectroscopy. *J. Opt. Soc. Am.*, 66(3):259–264, 1976.

[28] V. A. Vagin. Optimal apodization in fourier spectrometry. *Opt. Spectrosc.*, 48(2):190–193, 1980.

[29] V. A. Vagin. Quasi-optimal apodization in fourier spectroscopy. *Opt. Spectrosc.*, 54(2):209–212, 1983.

[30] J. Gronholz and W. Herres. Datenverarbeitung in der ft-ir spektroskopy. *C.A.L.*, pages 353–356 (5/84), 418–425 (6/84), 230–240 (5/85), 1984.

[31] B. E. A. Saleh and M. C. Teich. *Fundamentals of photonics*. John Wiley and Sons, New York, 1991.

[32] G. Wyszecki and W. S. Stiles. *Color Science*. Wiley, New York, 1967.

[33] K. McLaren. The development of the cie 1976 (l*a*b*) uniform colour-space and colour-difference formula. *Journal of the Society of Dyers and Colourists*, 92:338–341, 1976.

[34] H. Sakai. Consideration of signal-to-noise-ratio in fourier spectroscopy. In *International Conference on Fourier Spectroscopy*, pages 19–41, Aspen, 1971. Air Force Cambridge Research Laboraties, Bedford, Mass.

[35] E. E. Bell and R. B. Sanderson. Spectral errors resulting from random sampling-position errors in fourier transform spectroscopy. *Appl. Opt.*, 11(3):688–689, 1972.

[36] J. W. Fleming. Noise levels in broad band fourier transform absorption spectrometry. *Infrar. Phys.*, 17:263–269, 1977.

[37] R. R. Treffers. Signal-to-noise ratio in fourier spectroscopy. *Appl. Opt.*, 16(12):3103–3106, 1977.

[38] R. Meynart. Sampling jitter in fourier-transform spectrometers: spectral broadening and noise effects. *Appl. Opt.*, 31(30):6383–6388, 1992.

[39] K. B. Hill, S. A. Basinger, R. A. Stack, and D. J. Brady. Noise and information in interferometric cross correlators. *Appl. Opt.*, 36(17):3948–3958, 1997.

[40] S. A. Basinger, E. Michielssen, and D. J. Brady. Degrees of freedom of polychromatic images. *J. Opt. Soc. Am. A*, 12(4):704–714, 1995.

[41] J. R. Birch. Dispersive fourier transform spectroscopy. *Mikrochim. Acta*, 3:105–122, 1987.

[42] T. J. Parker. Dispersive fourier transform spectroscopy. *Contemp. Phys.*, 31(5):335–353, 1990.

[43] V. Natale and G. Ventura. Fourier spectroscopy in high background noise. *Appl. Opt.*, 23(13):2052–2053, 1984.

[44] A. S. Filler. Photon-noise-limited fourier spectroscopy. *J. Opt. Soc. Am.*, 63(5):589–591, 1973.

[45] H. Aryamanya-Mugisha and R. R. Williams. A fourier transform diode array spectrometer for the uv, visible, and near-ir. *Appl. Spectrosc.*, 39(4):693–697, 1985.

[46] G. Horlick, R. H. Hall, and W. K. Yuen. *Fourier Transform Infrared Spectroscopy*. Academic Press, New York, 1982.

[47] J. J. Fitzgerald, T. L. Chester, and J. D. Winefordner. Selectively-modulated interferometric dispersive spectrometer for ultraviolet-visible atomic and molecular spectrometry. *Anal. Chem.*, 47:2330, 1975.

[48] E. Voigtman and Winefordner. The multiplex disadvantage and excess low-frequency noise. *Appl. Spectrosc.*, 41(7):1182–1184, 1987.

[49] M. J. Milano, H. L. Pardue, T. E. Cook, R. E. Santini, D. W. Margerum, and J. M. T. Raycheba. Design and evaluation of a vidicon scanning spectrometer for molecular absorption and atomic emission spectrometry. *Anal. Chem.*, 46:374, 1974.

[50] Y. Talmi and R. W. Simpson. Self-scanned photodiode array: a multichannel spectrometric detector. *Appl. Opt.*, 19(9):1401–1414, 1980.

[51] M. L. Junttila. Stationary fourier-transform spectrometer. *Appl. Opt.*, 31(21):4106–4112, 1992.

[52] R. T. Hall, D. Vrabec, and J. M. Dowling. A high resolution, far infrared double-beam lamellar grating interferometer. *Appl. Opt.*, 5:1147, 1966.

[53] J. M. Dowling. Signal and noise in two-beam interferometry. *Appl. Opt.*, 6:1580–1581, 1967.

[54] E. E. Bell. Measurement of the far infrared optical properties of solids with a michelson interferometer used in the asymmetric mode: Part 1, mathematical formulation. *Infrar. Phys.*, 6:57–74, 1966.

[55] A. Filler. *J. Opt. Soc. Am.*, 54:762, 1964.

[56] P. Saarinen and J. Kauppinen. Spectral line-shape distortions in michelson interferometers due to off-focus radiation source. *Appl. Opt.*, 31(13):2353–2359, 1992.

[57] J. Kauppinen and P. Saarinen. Line-shape distortions in misaligned cube corner interferometers. *Appl. Opt.*, 31(1):69–74, 1992.

[58] G. Boer and T. Scharf. Compact static fourier transform spectrometer with large field of view based on liquid crystal technology. *Appl. Opt.*, To be published, 2001.

[59] E. Hecht. *Optics*. Addison-Wesley Publishing company, Reading, Massachusetts, 1987.

[60] J. Rufus, J. Pickering, A. Thorne, and G. Cox. Molecular absorption cross-section measurements by fts in the uv. In *Fourier Transform Spectroscopy : New Methods and Applications*, pages 122–123, Santa Barbara, 1999. Optical Society of America.

[61] R. Gupta, J. H. Burnett, U. Griesmann, and M. Walhout. Absolute refractive indices and thermal coefficients of fused silica and calcium fluoride near 193 nm. *Appl. Opt.*, 37:5964, 1998.

[62] A. P. Thorne, C. J. Harris, I. Wynne-Jones, R. C. M. Learner, and G. Cox. *J. Phys. E: Sci. Instrum.*, 20:54, 1987.

[63] N. de Oliveira and D. Joyeux. A wavefront division intererometer for fts in the vuv-xuv range. In *Fourier Transform Spectroscopy : New Methods and Applications*, pages 178–180, Santa Barbara, 1999. Optical Society of America.

[64] P. Luc and S. Gerstenkorn. Fourier transform spectroscopy in the visible and ultraviolet range. *Appl. Opt.*, 17(9):1327-1331, 1978.

[65] G. W. Stroke and A. T. Funkhouser. Fourier-transform spectroscopy using holographic imaging without computing and with stationary interferometers. *Phys. Lett.*, 16(3):272–274, 1965.

[66] K. Yoshihara and A. Kitade. Holographic spectra using a triangle path interferometer. *Jpn. J. Appl. Phys.*, 6:116, 1967.

[67] K. Kamiya, K. Yoshihara, and K. Okada. Holographic spectra obtained with lloids mirror. *Jpn. J. Appl. Phys.*, 7:1129, 1968.

[68] B. H. Billings. Visual fourier-transform spectroscopy with a single crystal plate. *J. Opt. Soc. Am.*, 65(7):817–824, 1975.

[69] J. Genest, P. Tremblay, and A. Villemaire. Throughput of tilted interferometers. *Appl. Opt.*, 37(21):4819–4822, 1998.

[70] T. Okamoto, S. Kawata, and S. Minami. Fourier transform spectrometer with self-scanning photodiode array. *Appl. Opt.*, 23(2):269–273, 1984.

[71] T. H. Barnes. Photodiode array fourier transform spectrometer with improved dynamic range. *Appl. Opt.*, 24(22):3702-3706, 1985.

[72] J. B. Rafert, R. G. Sellar, and J. H. Blatt. Monolithic fourier-transform imaging spectrometer. *Appl. Opt.*, 34(31):7228–7230, 1995.

[73] M. P. Dierking and M. A. Karim. Solid-block stationary fourier-transform spectrometer. *Appl. Opt.*, 35(1):84–89, 1996.

[74] K. D. Möller. Wave-front-dividing array intefrerometer without moving parts for real-time spectroscopy from the ir to the uv. *Appl. Opt.*, 34(9):1493–1501, 1995.

[75] M. Hashimoto and S. Kawata. Multichannel fourier-transform infrared spectrometer. *Appl. Opt.*, 31(28):6096–6101, 1992.

[76] A. R. Harvey, M. Begbie, and M. J. Padgett. Stationary fourier transform spectrometer for use as a teaching tool. *Am. J. Phys.*, 62(11):1033–1036, 1994.

[77] N. Ebizuka, M. Wakaki, Y. Kobayashi, and S. Sato. Development of a multichannel fourier transform spectrometer. *Appl. Opt.*, 34(34):7899–7906, 1995.

[78] T. J. Hirschfeld. Fellgett's advantage in uv-vis multiplex spectroscopy. *Appl. Spectrosc.*, 30:68–69, 1976.

[79] W. Kolar and R. Williams. Comparison of interferogram noises in the ultraviolet and visible regions. *Appl. Spectrosc.*, 46(4):615–619, 1992.

[80] A. Girard. Devices for multiplex stellar spectroscopy. In G. A. Vanasse, editor, *Aspen international conference on Fourier spectroscopy*, pages 425–428, Aspen, Col., 1970. Springfield-Va. NTIS.

[81] S. D. Collins, R. L. Smith, C. Gonzles, K. P. Stewart, J. G. Hagopian, and J. M. Sirota. Fourier-transform optical systems. *Opt. Lett.*, 24(12):844–846, 1999.

[82] C. Marxer and N. F. De Rooij. Micro-optomechanical 2 × 2 switch for single-mode fibers based on plasma-etched silicon mirror and electrostatic actuation. *Journal of Lightwave Technology*, 17(1):2–6, 1999.

[83] C. Marxer, P. Griss, and N. F. De Rooij. A variable optical attenuator based on silicon micromechanics. *IEEE Photonics Technology Letters*, 11(2):233–235, 1999.

[84] B. Guldimann, P. Dubois, P.-A. Clerc, and N.F. De Rooij. Fiber optic - mems accelerometer with high mass displacement resolution. In *Transducers '01 Eurosensors XV, The 11th International Conference on Solid-State Sensors and Actuators*, Munich, 2001.

[85] W. Noell, P. A. Clerc, L. Dellmann, B. Guldimann, H. P. Herzig, O. Manzardo, C. Marxer, K. Weible, R. Dändliker, and N. De Rooij. Applications of soi-based optical mems. *J. Selec. Top. Quant. Electr.*, 8:148, 2002.

[86] J. Mohr, M. Koh, and W. Menz. Micro optical switching by electrostatic linear actuators with large displacements. In *Seventh International Conference on Solid-State Sensors and Actuators (Transducers '93)*, pages 120–123, Yokohama, Japan, 1993.

[87] T. Hirano, T. Furuhata, K. J. Gabriel, and H. Fujita. Design, fabrication and operation of submicron gap electrostatic comb drive actuators. *J. Microelectromech. Syst.*, 1:52, 1992.

[88] C. R. Marxer. *Silicon Micromechanics for applications in fiber optic communication.* PhD thesis, University of Neuchâtel, 1997.

[89] P. Nussbaum, I Philipoussis, A. Husser, and H. P. Herzig. Simple technique for replication of micro-optical elements. *Opt. Eng.*, 37(6):1804–1808, 1998.

[90] J. D. Strong and G. A. Vanasse. Lamellar grating far-infrared interferometer. *J. Opt. Soc. Am.*, 50(113), 1960.

[91] M. Harwit and N. J. A. Sloane. *Hadamard transform optics.* Academic Press, New York, 1979.